Atomistic Simulation of Electroceramics

James Alexander Dawson

Department of Materials Science and Engineering
University of Sheffield

A thesis submitted for the degree of
Doctor of Philosophy

December 2012

Abstract

This work presents a range of atomistic techniques used to study the energetic and structural properties of the perovskite, barium titanate ($BaTiO_3$). Particular attention is given to defective structures of $BaTiO_3$ and their importance at the atomic scale and for the behaviour of the material.

Using a newly developed potential model calibrated against *ab initio* calculations, simulations of rare earth (RE) and transition metal doping of both the cubic (space group Pm3m) and hexagonal polymorphs (space group $P6_3/mmc$) of $BaTiO_3$ have been completed. All major dopant charge compensation schemes have been considered as well as the contribution from binding between charged defects. The results agree with simple ion size arguments and excellent agreement with experiment is observed. Clear evidence of the stabilisation of the hexagonal polymorph as a result of trivalent and tetravalent transition metal doping is presented.

Lattice statics have also been used to study the energetics and structures of a range of $ATiO_3$ solid solutions, where A is Ba, Ca and Sr. Energy of mixing curves have been produced using both the new and old potential models. The relationship between strain and the ferroelectric Curie temperature (T_c) in $Ba_{1-x}Ca_xTiO_3$ has also been considered.

Molecular dynamics methods have been applied to investigate oxygen diffusion in cubic $BaTiO_3$ and $SrTiO_3$. Mean square displacement (MSD) calculations were completed over a range of oxygen vacancy concentrations. Diffusion coefficients and activation energies have been calculated and compared with experiment.

Finally, we have performed density functional theory (DFT) simulations on mono- and di-vacancies in hexagonal $BaTiO_3$. Defect formation energies are derived for multiple charge states and due consideration is given to the errors usually associated with such calculations. Equilibrium concentrations of vacancies in the system are also presented. Comparisons are drawn with the cubic polymorph as well as with potential-based simulations and experimental results.

Acknowledgements

The time spent at the University of Sheffield during my PhD has been both a very rewarding and challenging experience. Firstly, I would like to thank both of my supervisors, Professor John Harding and Professor Derek Sinclair, as without their constant advice and support this piece of work would not have been possible.

A special thanks also goes to Dr. Colin Freeman for his continual support and patience, especially during the early stages of my PhD. My gratitude also goes to all other members of the Professor Harding research group for being a constant source of motivation and assistance.

I would like to thank Hungru, James M and the other members of the H7 office as well as the members of the 'Cabal' for a variety of reasons, some academic and some not.

Finally, my gratitude goes to all my family and friends in Stoke for their constant support and inspiration during this time.

I declare that the work in this dissertation was carried out in accordance with the Regulations of the University of Sheffield. The work is original, except where indicated by the appropriate reference in the text. No part of this thesis has been submitted for any other academic award. Any views expressed in the thesis are those of the author.

James Alexander Dawson

December 2012

Table of Contents

Published Work

The work presented in this thesis has led to a number of publications.

'A new potential model for barium titanate and its implications for rare-earth doping', C. L. Freeman, J. A. Dawson, H. Chen, J. H. Harding, L. - B. Ben and D. C. Sinclair, Journal of Materials Chemistry **21**, 4861, (2011).

'An atomistic study into the defect chemistry of hexagonal barium titanate', J. A. Dawson, C. L. Freeman, L. - B. Ben, J. H. Harding and D. C. Sinclair, Journal of Applied Physics **109**, 084102, (2011).

'First-principles study of intrinsic point defects in hexagonal barium titanate', J. A. Dawson, J. H. Harding, H. Chen and D. C. Sinclair, Journal of Applied Physics **111**, 094108, (2012).

'The influence of A-site rare earth ion size in controlling the Curie temperature of $Ba_{1-x}RE_xTi_{1-x/4}O_3$', C. L. Freeman, J. A. Dawson, J. H. Harding, L. - B. Ben and D. C. Sinclair, Advanced Functional Materials, DOI: 10.1002/adfm.201201705 (2012).

'Phase stabilisation of hexagonal barium titanate doped with transition metals: A computational study', J. A. Dawson, C. L. Freeman, J. H. Harding and D. C. Sinclair, Journal of Solid State Chemistry (accepted) (2012).

'Energetics of donor-doping, metal vacancies and oxygen-loss in A-site Rare-Earth doped $BaTiO_3$', C. L. Freeman, J. A. Dawson, H. Chen, L. - B. Ben, J. H. Harding, A. R. West and D. C. Sinclair, Advanced Functional Materials (accepted) (2012).

1

Introduction

The significant increase in computational power and its availability has led to improved usefulness and a wide range of simulation methods in all areas of science. In chemistry and physics, computational methods have become a crucial tool in the study and understanding of the structure and properties of complex materials, especially where experiment maybe difficult or impossible. Through the combination of computational and experimental studies, a far better insight into a material can be achieved.

In this thesis we present results for a range of properties of barium titanate, $BaTiO_3$ and similar perovskite structured materials. $BaTiO_3$ has many industrial and technological uses as a result of its useful electrical properties. It is well known for its ferroelectric properties and high dielectric constant [1], as well as its application as a lead-free piezoelectric material [2]. Also, its positive temperature coefficient of resistivity (PTCR) [3] means it is important in surface heaters and temperature sensors. Other important applications include random access memories (RAM) as well as infrared sensors [4].

Ferroelectricity is defined as the spontaneous electric polarisation of a material, which when an external electric field is applied can be reversed. Ferroelectricity in a material was first reported by J. Valasek in 1920 [5]. In a series of papers, Valasek detailed the unusual electrical properties of Rochelle salt and the link between this materials dielectric properties and ferromagnetism [5-6]. $BaTiO_3$ was the first discovered ferroelectric oxide and is still the most widely used ferroelectric material. Another important ferroelectric material is lead zirconate titanate (PZT) which has important applications in ferroelectric random access memories (FRAM).

Many of the interesting properties of $BaTiO_3$ are a result of it adopting the perovskite structure. This is named after the discoverer of $CaTiO_3$, L. A. Perovsky [7] and hence compounds isostructural to $CaTiO_3$ (ABX_3) are called perovskites. $BaTiO_3$ is an excellent example of a ferroelectric perovskite based on a d^0 cation occupying the B-site and is therefore a useful 'model' system for fundamental studies related to structure-composition-property relationships. Therefore, it is to be expected that there is a wealth of research on this material. While this is correct; it is also true that many of its properties are not yet fully understood. Throughout this work, via the use of both potential-based and quantum mechanical (QM) simulation techniques and by comparison to experiment, we attempt to provide further understanding into this technologically important material.

Above the ferroelectric Curie temperature, T_c (~ 130 ^oC) the crystal structure of $BaTiO_3$ is cubic. Cubic $BaTiO_3$ (see figure 1.1) has one Ti^{4+} ion in the centre of the unit cell (0.5, 0.5, 0.5) and six O^{2-} ions in the faces of the cell (0.5, 0.5, 0.0). A Ba^{2+} ion is located in each of the corners of the unit cell (0.0, 0.0, 0.0). There are four polymorphs and three polymorphic phase transition temperatures associated with *c*-$BaTiO_3$. Below ~ 130 ^oC the cubic polymorph transforms into the ferroelectric tetragonal polymorph. Further distortions occur at lower temperatures associated with transformations into orthorhombic and rhombohedral polymorphs at ~ 0 ^oC and - 90 ^oC, respectively [8]. In addition to these polymorphs, a high temperature hexagonal polymorph exists above ~ 1425 ^oC. The structure is based on a combination of cubic (c) and hexagonal (h), close packed BaO_3 layers based on a $(cch)_2$ sequence, and is classified as a 6H-type hexagonal perovskite (figure 1.2). This results in a combination of face-sharing Ti_2O_9 dimers connected by a corner sharing TiO_6 unit.

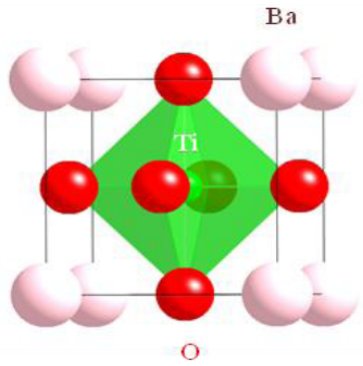

Figure 1.1: Unit cell of the cubic structure of $BaTiO_3$.

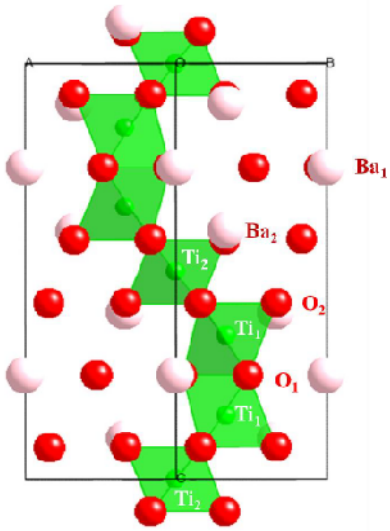

Figure 1.2: Unit cell of the hexagonal structure of $BaTiO_3$.

In chapter 2, classical methods are described in which different atomic interactions are modelled by fitted potential functions. Both lattice statics and molecular dynamics are explained as well as the theory behind defect formation and its thermodynamic consequences. Defects are modelled using the Mott-Littleton approximation and diffusion data are obtained by mean square displacement (MSD) calculations.

QM methods are featured in chapter 3. In this work, we make use of density functional theory (DFT) to solve the many electron problem associated with electronic structure calculations. Through the use of Bloch's theorem and the pseudopotential approximation, large unit cells of solid state systems can be simulated. It should be noted, however, that the size of cell that can be simulated by DFT cannot compete with

the size of cell that potential-based methods can study. However, while DFT cannot model the same size of cell as potential-based calculations, its accuracy is greater as a result of the electronic structure being considered explicitly instead of the approximations made in potential-based calculations. It is therefore important to consider which method is appropriate for the desired application.

Doping of electroceramic materials is commonplace and is crucial in improving and tailoring certain properties, especially the electrical properties. The prediction of where these dopants will sit in the lattice and hence whether they will act as donors or acceptors and the type of charge compensating defect associated with that dopant can yield useful information. In the case of low dopant concentrations and complex electronic and vacancy charge compensation mechanisms, it can be difficult for experiment to conclusively prove one mechanism of incorporation over another which leads to conflicting hypotheses. In chapter 4 we simulate the rare earth and transition metal doping of cubic-$BaTiO_3$ (*c*-$BaTiO_3$) and hexagonal-$BaTiO_3$ (*h*-$BaTiO_3$). We use a new $BaTiO_3$ potential model, lattice statics methods and the Mott-Littleton approximation to calculate solution binding energies for each dopant and each dopant incorporation mechanism. Attention is also given to stabilisation of the hexagonal polymorph through transition metal doping. Our results show that tri-valent and tetra-valent dopant ions have the most significant effect on this stabilisation process. Results are compared with previous modelling and experiment.

Local structure of $BaTiO_3$ solid solutions is analysed in chapter 5. A-site doped $BaTiO_3$ solid solutions are used primarily for electrical applications such as multilayer ceramic capacitors (MLCCs) (Ca-doped $BaTiO_3$ (BCT)) and dynamic random access memories (DRAM) (Sr-doped $BaTiO_3$ (BST)). Another feature of these dopants is the significant effect on the ferroelectric Curie temperature (T_c). While these effects are well understood for BST, this is not the case for BCT. Lattice statics modelling of the local structure of these solid solutions shows that serious distortion occurs in the Ca-O bonds in BCT and that this distortion increases with increasing Ca concentration up to the solid solution limit. It is also shown that Ca off-centering is preferred at Ca concentrations where T_c is highest. These results are used to interpret the unusual T_c

effects in BCT. Internal energies of mixing for the BCT and BST solid solutions are also presented.

In chapter 6 we present results from molecular dynamics simulations of oxygen diffusion in the bulk structures of $BaTiO_3$ and $SrTiO_3$. It is generally believed that oxygen vacancies in the undoped structures of these materials are compensated by electrons [9-10]. Both these oxygen vacancies and the compensating electrons cause a reduction in the performance and increased degradation in $BaTiO_3$ based MLCCs. Mean square displacement calculations are completed on these materials with varying levels of oxygen vacancies and three potential charge compensation defects ($Ti^{4+} \rightarrow Ti^{3+}$ reduction, Ti vacancies and Ba vacancies). Activation energies of diffusion and conduction are calculated and comparison with experimental values is given.

The thermodynamics of intrinsic point defects in *h*-$BaTiO_3$ calculated using DFT and the Zhang-Northrup formalism [11] is presented in chapter 7. Similar to the cubic polymorph of the material, *h*-$BaTiO_3$ receives attention due to its electrical and semiconducting properties and again these properties are significantly affected by intrinsic and extrinsic defects. The defect formation energy is defined as the Gibbs free energy difference between the defective and perfect cell with regard to specific chemical potentials and the contribution of electrons being added or removed. However, a drawback of zero temperature DFT calculations is the exclusion of entropic and pressure/volume contributions from the Gibbs free energy of each particle. While this is a minor factor for solids as these contributions are small, it does present a significant issue for calculations on gaseous particles where such contributions are much larger. This problem is corrected through the use of ideal gas physics and a method described by Finnis *et al*. [12]. Our results indicate that oxygen vacancies are the favoured defect in metal-rich conditions and that in oxygen-rich conditions the dominant defect is dependent upon the Fermi level. Binding energies suggest that metal-oxygen di-vacancy formation is favourable.

Chapter 8 concludes this work and considers possible research that could follow on from our results. A general introduction and literature review for the relevant material and topic is also given in each chapter.

References

[1] C. A. Miller, British Journal of Applied Physics **18**, 1689 (1967).

[2] T. Karaki, K. Yan and M. Adachi, Advances in Science and Technology **54**, 7 (2008).

[3] S. R. Syrtsov, V. N. Shut, I. F. Kashevich, A. S. Sedlovsky and B. E. Watts, Materials Science in Semiconductor Processing **5**, 223 (2002).

[4] J. Thongrueng, K. Nishio, Y. Watanabe, K. Nagata and T. Tsuchiya, Journal of the Australasian Ceramic Society **37**, 51 (2001).

[5] J. Valasek, Physical Review **15**, 537 (1920).

[6] J. Valasek, Physical Review **17**, 475 (1921).

[7] V. V. Lemanov, A. V. Sotnikov, E. P. Smirnova, M. Weihnacht R. Kunze, Solid State Communications **110**, 611 (1999).

[8] A. J. Moulson and J. M. Herbert, *Electroceramics - Materials, Properties, Applications* (John Wiley and Sons Ltd., Chichester, 2003).

[9] D. I. Woodward, I. M. Reaney, G. Y. Yang, E. C. Dickey and C. R. Randall, Applied Physics Letters **84**, 4650 (2004).

[10] W. Gong, H. Yun, Y. B. Ning, J. E. Greedan, W. R. Datars, C. V. Stager, Journal of Solid State Chemistry **90**, 320 (1991).

[11] S. B. Zhang and J. E. Northrup, Physical Review Letters **67**, 2339 (1991).

[12] M. W. Finnis, A. Y. Lozovoi and A. Alavi, Annual Review Materials Research **35**, 167 (2005).

2

Potential-based Methods

2.1 Introduction

The vast majority of all atomistic simulation techniques can be divided into either classical, potential-based methods or quantum mechanical methods. Both of these different simulation fields are featured in this thesis. Potential-based simulation methods do not explicitly take into account electrons and hence have the advantage of being able to simulate large systems that would be far too computationally expensive for quantum mechanics. Quantum mechanics does, however, have the advantage of being more accurate and can provide important information that could not be revealed using classical methods. In this chapter we discuss potential-based methods including lattice statics and molecular dynamics. We also discuss the theory behind defect formation. Quantum mechanical methods are described in chapter 3. Further details of the techniques discussed here are available in [1-3].

2.2 Born-Oppenheimer Approximation

The Born-Oppenheimer approximation [4] is an important concept that allows the nuclear and electronic motions of an atom to be separated so that the wave function can be written as,

$$\Psi_{total} = \Psi_{electronic} \text{ x } \Psi_{nuclear} \tag{2.1}$$

It is assumed that the nuclear motion is so much slower than the electron motion meaning the nuclear coordinates are effectively fixed. As a result the electronic degrees of freedom can be treated separately from the nuclear degrees of freedom. Classical methods use this approximation implicitly and also use the further approximation that interatomic forces can be modelled using a simple classical interaction model where the atoms are treated as hard formally charged spheres. This allows the forces between the ionic spheres to be separated into a long-range Coulombic force and a short-range force.

2.3 Potentials

The potential energy (Φ) of a given system takes into account all interactions between the atoms whether they are long range Coulombic interactions or dispersion forces and short range interactions which are taken into account by the interatomic potentials. The sum of all the short-range interactions can be expressed by,

$$\Phi = \sum_{i<j}^{n} V_{ij} + \sum_{i<j<k}^{n} V_{ijk} + ..., \tag{2.2}$$

where ΣV_{ij} is the summation of the interactions between all pairs of atoms and ΣV_{ijk} is the summation of the interaction over all three atom combinations and so on. Therefore, the short-range interaction energy can be broken down into n discrete summations, where n is dependent on the system being simulated. So for example for n = 3,

$$\Phi = V_{12} + V_{13} + V_{23} + V_{123} \tag{2.3}$$

In our calculations, the Coulombic terms are calculated using the assumption that the ions are in their formal charge states and therefore the short-range terms are the only the variables that must be addressed. The long-range Coulombic terms are calculated using Coulomb's law,

$$V_{ij} = \sum_{i \neq j}^{n} \frac{q_i q_j}{4\pi\varepsilon_0 r_{ij}} \tag{2.4}$$

where q_i and q_j represent the ionic charge of the atoms, r_{ij} represents the distance between the atoms and ε_0 is the vacuum permittivity (8.854×10^{-12} F/m).

The ability to model the short-range interactions and therefore the system is entirely dependent on the accuracy of the potential parameters. There are two general methods used for fitting potential parameters; fitting to experimental data or to *ab initio* calculations. For the first method parameters are usually fitted to experimental values such as the lattice parameter, lattice energy, interatomic distances and thermodynamic quantities. Potential fitting using *ab initio* simulations has also become a common method over the last decade. *Ab initio* methods are effective in gaining a larger range of data over varying theoretical conditions and hence can provide us with more information for the fitting process, whereas it would be far more time consuming or physically impossible to get the same results via experimental techniques. It is also important to consider which types of potential will be required for the system of interest. For some systems, the use of only two-body potentials in a simulation may not give the necessary level of accuracy and higher order terms may be required. Hence, it is not only the potential parameters themselves that are important in achieving an accurate representation of the system but also the types of potentials. It is essential, therefore, that the fitting and the data to which the potentials are fitted are reliable.

The types of potentials used to model the titanate materials in this work are described in the next section.

2.3.1 Two-body Potentials

For ionic solids, two-body potentials are most important. There are numerous different potential types used in modelling the forces in solid state systems. One main example is the Buckingham potential which we have used throughout this work,

$$V_{ij} = \sum_{i \neq j}^{n} A\exp(-r_{ij} / \rho) - \frac{C}{r_{ij}^6} \tag{2.5}$$

where A, ρ and C are the parameters that must be fitted. Two-body potentials are divided into two elements, a repulsive and an attractive part. In the Buckingham potential the repulsive part is accounted for by the $A\exp(-r_{ij}/p)$ term and the attractive part is accounted for by the C/r_{ij}^6 term. The repulsive element is a two-body potential that comes from the Pauli repulsion arising from the overlap of the electron clouds of each atom. The attractive element represents Van der Waals interactions. Electrons in close proximity experience correlated motions which in turn produce instantaneous dipoles. The strength of these dipoles is dependent upon the polarisability of the electron clouds. This explains why this term is most important in highly polarisable species such as anions. In the case of atoms with small polarisabilities the attractive C term is usually ignored. This produces the simpler Born-Mayer potential, where the other terms have the same meaning as for the Buckingham potential.

$$V_{ij} = \sum_{i \neq j}^{n} A\exp(-r_{ij} / \rho) \tag{2.6}$$

Another common form of two-body potentials is the Lennard-Jones potential,

$$V_{ij} = \sum_{i \neq j}^{n} 4\varepsilon_{ij} \left[\left(\frac{\sigma_{ij}}{r} \right)^n - \left(\frac{\sigma_{ij}}{r} \right)^m \right] \tag{2.7}$$

where ε and σ are the potential parameters, ε represents the depth of the energy well, i.e. the binding energy at the ideal interatomic separation, σ is the interatomic separation for $V_{ij} = 0$. Similar to the Buckingham potential there is a Van der Waals attraction term

$((\sigma_{ij}/r)^m)$ and a Pauli repulsion term $((\sigma_{ij}/r)^n)$. The n and m values can be altered depending upon the nature of the potential curve required, commonly values of n = 12 and m = 6 are chosen. However a smaller n value is often used when a less repulsive potential is required e.g. n = 7, 9.

2.3.2 Three-body Potentials

In addition to the two-body potentials, some systems may require another potential type to accurately describe the bending in a triplet of atoms. This is true for titanates, which require a O-Ti-O three-body term because of the nature of the bonding character in the Ti-O interaction. This bond angle term is used to describe the effect of altering the O-Ti-O bond from its usual ideal angle of 90˚. This form of this potential is given by,

$$V_{ij} = \frac{k_\theta}{2}(\theta - \theta_0)^2 \tag{2.8}$$

where k_θ is the harmonic force constant, θ is the angle between the bonds and θ_0 is the equilibrium optimum bond angle (90˚) as shown by figure 2.1.

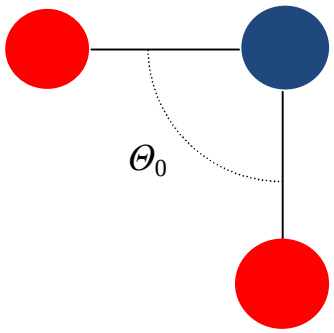

Figure 2.1: Schematic representation of a three-body term.

In the harmonic form of the three-body potential, any distortion from the equilibrium bond angle results in an energetic penalty. For ionic materials with easily polarisable anions, a three-body term is sometimes used to model the dispersion energy

contribution from these atoms. This is usually done using the Axilrod-Teller potential [5].

2.4 Shell Model

Until now, it has been assumed that the electron densities of the atoms are fixed and that the nuclei are just hard charged spheres. This approximation is termed the 'rigid ion' model. Although this model has important applications, especially in molecular dynamics, it does not take into account the polarisability of the atoms. This is a significant problem when defects are introduced into a solid state system. In this approximation the high-frequency dielectric constants are unity and will therefore not be capable of accurately modelling the massive influence a charged defect will have on its surrounding lattice.

An effective way of dealing with this problem is the shell model developed by Dick and Overhauser in 1958 [6]. This model represents an atom as a negatively charged massless shell and a positively charged core with the relevant atomic mass. Although both components are charged they interact via a harmonic spring and its spring constant *k*, as opposed to a conventional electrostatic interaction.

$$V_i = \frac{1}{2} k_i \delta_i^{\,2} \tag{2.9}$$

where *k* is the spring constant, as discussed, and δ is the distance between the core and the centre of the shell.

The cores and shells of all atoms interact Coulombically (except when the core and shell are on the same atom) and short range interactions take place only between the shells. The polarisability of an isolated atom in this model is given by,

$$\alpha = \frac{1}{4\pi\varepsilon_0}(Y^2 / k) \tag{2.10}$$

where Y is the shell charge (e) and *k* is again the spring constant (eV A^{-2}).

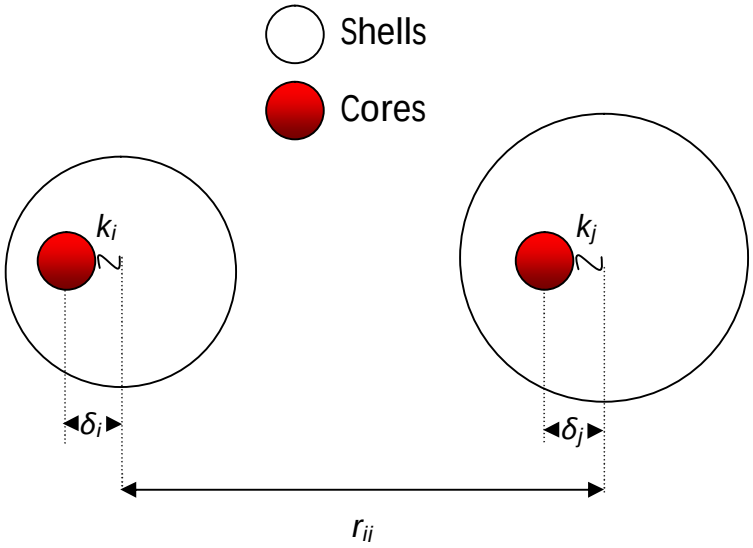

Figure 2.2: The Dick-Overhauser shell model.

Although the absolute value of Y does not have a clear meaning, the shell model provides an effective way of simulating the polarised electron clouds. In this work, all the ions have been modelled with the shell model. However, the cation species have considerably higher spring constants than the easily polarisable O anions.

2.5 Perfect Lattice Simulation

It is unfeasible to calculate the energy of a whole system directly, as the calculation would effectively involve an infinite number of unit cells. Therefore periodic boundary conditions are employed to allow the calculation to be completed on a far more reasonable scale. Periodic boundary conditions also remove the surfaces of the system, so that only the bulk of the system is considered. The energy of the perfect lattice can then be calculated from the individual calculations of the short- and long-range interactions,

$$E_L = \sum_{ij} \frac{q_i q_j}{r_{ij}} + \sum \Phi_{ij}(r_{ij}) \tag{2.11}$$

where the symbols have the same meaning as in equation (2.4) and Φ represents the short-range interactions.

The short-range interactions fall quickly to zero over several interatomic distances. This allows a simple finite cutoff distance to be applied to each potential. While this application is simple for short-range interactions, direct summation of the electrostatic energies is impossible due to their slow convergence in real space. The rapid decrease in energy over interatomic separation for short-range interactions is not true for the Coulombic long range interactions as there is still a significant energetic contribution from these interactions over a large distance. The Coulomb potential between the ions decays at the rate of r^{-1}, but the number of interacting ions also increases as a function of r^2 meaning that the energy is conditionally convergent.

2.5.1 Ewald Summation

The Ewald summation [7] is used to solve the problem of the conditionally converging summation. This method transforms the slowly convergent summation into two rapidly converging terms; one part is calculated in real space (where the short-range interactions are also calculated) and the other part in reciprocal/Fourier space. The method involves first subtracting a lattice of Gaussian charge distributions from the lattice of point charges. The total charge of each Gaussian distribution of charge is the same as that of the point charge at the same site. The effect of this is to screen the point charges and produce a short-range term in real space. This lattice of Gaussian charges must then be added on again, but the total energy of this lattice can readily be obtained by first transforming to reciprocal space and then performing the summation. Finally, the spurious interaction of the point charges with the Gaussian distribution of charge on the same site must be removed.

The total electrostatic potential energy between point charges can be written as,

$$U = \frac{1}{2}\sum_{i=1}^{N} q_i \phi(r_i) \tag{2.12}$$

where

$$\phi(r_i) = \sum_{j,n}{}' \frac{q_j}{\left| r_{ij} + nL \right|} \tag{2.13}$$

for a cubic unit cell where the prime means sum over all j except $j = i$, $n = 0$ and L is the unit cell length. As explained above, we can express the Ewald potential as three terms,

$$\phi(r_i) = \phi_{recip}(r_i) + \phi_{real}(r_i) - \phi_{self}(r_i) \tag{2.14}$$

where $\phi_{recip}(r_i)$ is the reciprocal/Fourier term potential of a periodic array of Gaussian charges with widths of $\sqrt{2/\eta}$ at r_i. $\phi_{real}(r_i)$ is the real/short-range potential of the point charge array screened by the Gaussian array. $\phi_{self}(r_i)$ is the interaction of the point charge with the Gaussian on its own site which should not be present.

The Gaussian charge distribution is given by,

$$p_{\boldsymbol{G}} = q_i \left(\frac{\eta}{\pi} \right)^{3/2} e^{-\eta r^2} \tag{2.15}$$

where η is a variable parameter chosen to maximise the efficiency of the convergence.

The potential due to the Gaussian array is given by,

$$\phi_{recip}(r_i) = \frac{4\pi}{V} \sum_{\boldsymbol{G} \neq 0} \left\{ \sum_j q_j \exp(i\boldsymbol{G}.r_{ij}) \right\} \frac{1}{\boldsymbol{G}^2} \exp\left(-\frac{\boldsymbol{G}^2}{4\eta} \right) \tag{2.16}$$

where $\boldsymbol{G}$ is the reciprocal lattice vector, V is the unit cell volume. Note that the $\boldsymbol{G} = 0$ term cannot exist for a charge-neutral cell.

The short-range potential is expressed as,

$$\phi_{real}(r_i) = \frac{q_i}{r} - \frac{q_i}{r}\,\mathrm{erf}\,(r\sqrt{\eta}) \tag{2.17}$$

$$= \frac{q_i}{r}\,\mathrm{erfc}(r\sqrt{\eta}) \tag{2.18}$$

where erf(r) is the standard error function and erfc(r) is the complementary error function.

The self-interaction term is represented by,

$$\phi_{self}(r_i) = 2q_i\sqrt{\frac{\eta}{\pi}} \tag{2.19}$$

This combination of these three terms allows the full expression for the Coulombic contribution to the energy to be derived,

$$U = \frac{4\pi}{2V}\sum_{\boldsymbol{G}\neq 0}\left(\sum_{i,j=1}^{N} q_i q_j \exp(i\boldsymbol{G}.r_{ij})\right)\frac{1}{\boldsymbol{G}^2}\exp\left(-\frac{\boldsymbol{G}^2}{4\eta}\right) + \frac{1}{2}\sum_{i\neq j}^{N}\frac{q_i q_j}{r_{ij}}\mathrm{erfc}(r_{ij}\sqrt{\eta}) - \sqrt{\frac{\eta}{\pi}}\sum_{i=1}^{N} q_i^2 \tag{2.20}$$

By separating the summation into these terms, we can produce two rapidly converging functions, one in real space and one in reciprocal space. The final summation is rapidly convergent with respect to both increasing $\boldsymbol{G}$ and r.

2.6 Energy Minimisation

Energy minimisation techniques are often employed in classical simulations as we are normally interested in the lowest energy configuration (also known as the global energy minimum) of a system. This can be a challenging process as a potential energy surface is very complex and finding a minimum can be difficult. There are numerous methods used to achieve this including molecular dynamics and Monte Carlo simulations, but most are based on the calculation of energy derivatives with respect to variables such as Cartesian coordinates. In this work we use GULP [8] to perform energy minimisation.

All the calculations completed in this thesis using GULP are based on the concept of lattice statics. The free energy of a system, G, is given by,

$$G = U + pV - TS \tag{2.21}$$

where U is the total internal energy, p is pressure, V is volume, T is temperature and S is the entropy. In lattice statics the effects of temperature are not implicitly calculated and so the vibrations and therefore the entropy (a result of atomic vibration in the crystal) is neglected. The calculations are also performed at atmospheric pressure so the pV term is negligible. The energy optimisation is carried out using the lattice vectors and coordinates alone,

$$\frac{\partial G_{static}}{\partial Z_i} = \frac{\partial \Phi}{\partial Z_i} = 0 \tag{2.22}$$

where Z_i are all the atomic coordinates and lattice vectors. It should be noted that a lattice dynamics term can be included in such calculations to incorporate the effects of temperature. This is usually done using a quasi-harmonic approach [9] where lattice vibrations are calculated using a Taylor expansion about the equilibrium atomic positions.

Often second derivative methods are used for minimisation, one such example is the Newton-Raphson (NR) method which is the method employed by the GULP code. These methods use both the first derivatives (gradient) and also the second derivatives (Hessian matrix) to locate the minimum. The potential energy surface, E, or hypersurface may be expanded as a second order Taylor expansion,

$$E(x + dx) = E(x) + E'(x)dx + \frac{1}{2}E''(x)dx^2 \tag{2.23}$$

where $E'(x)$ is the vector of the first derivatives (g) and $E''(x)$ is the matrix of the second derivatives, the Hessian (H). The NR method is used to significantly reduce the computational effort in finding a minimum in the complex energy surface. It works by using the derivatives from the previous point to calculate the vector for the next step (dx),

$$dx = -H^{-1}g \tag{2.24}$$

The main problem with the NR method is the computational expense of calculating the Hessian and inverting it for every step of the minimisation. The inversion of the Hessian is usually the most expensive step of the method, especially for large system sizes. Also, the Hessian matrix must be positive definite (i.e. all eigenvalues are positive), if not then the process can become unstable and saddle points can be found as opposed to the minimum. Quasi-Newton methods are often employed to minimise these issues. The Broyden-Fletcher-Goldfarb-Shanno (BFGS) method [10-12] is regarded as the most efficient method and is also used in the GULP code. The BFGS algorithm is a well known approach used to avoid recalculating the Hessian every step through the use of a quantity labeled J which is recalculated based upon x and the vector of the first derivative,

$$J_{i+1}^{-1} = J_i^{-1} + \frac{(x_{i+1} - x_i)(x_{i+1} - x_i)}{(x_{i+1} - x_i)(g_{i+1} - g_i)} - \frac{(J_i^{-1}(g_{i+1} - g_i))(J_i^{-1}(g_{i+1} - g_i))}{(g_{i+1} - g_i)J_i^{-1}(g_{i+1} - g_i)} + ((g_{i+1} - g_i)J_i^{-1}(g_{i+1} - g_i))u.u \tag{2.25}$$

The vector, u, is expressed as,

$$u = \frac{(x_{i+1} - x_i)}{(x_{i+1} - x_i)(g_{i+1} - g_i)} - \frac{J_i^{-1}(g_{i+1} - g_i)}{(g_{i+1} - g_i)J_i^{-1}(g_{i+1} - g_i)} \tag{2.26}$$

This algorithm reduces the computational expense in recalculating the Hessian every step. However, the Hessian is still recalculated explicitly every few steps for accuracy or if a situation arises where the approximation is deemed inaccurate as a result of an unusual step in the minimisation process e.g. the energy drops below a given threshold.

2.7 Point Defects in Solids

Intrinsic point defects are caused by the increase in thermal vibrations as the temperature is raised beyond absolute zero. Intrinsic defects include vacancies and interstitials. Extrinsic defects or dopants (see figure 2.3) can be present in the crystal naturally or purposely introduced into the structure. Vacancies are created by the

breaking of bonds and result in usually occupied lattice sites becoming unoccupied. Interstitials, however, usually form at vacant lattice sites which therefore become occupied. Frenkel pairs can also form which consist of a vacancy-interstitial pair.

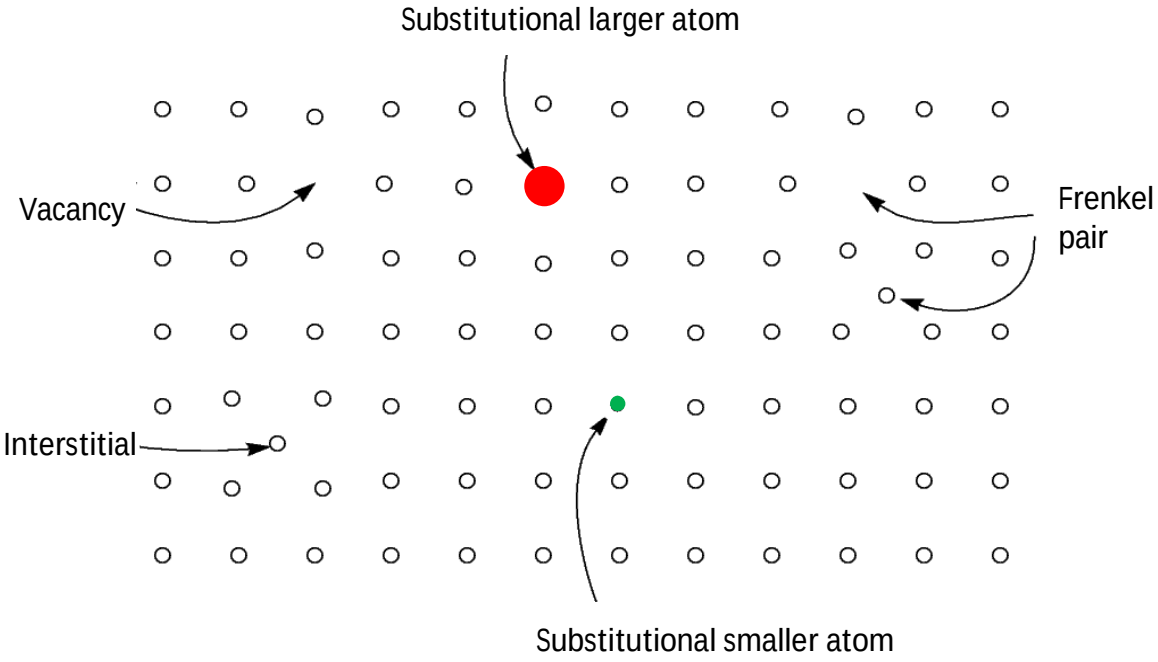

Figure 2.3: Illustration of point defects in a 2D lattice.

Substitutional atoms can be divided into isovalent and aliovalent dopants. Isovalent dopants have the same charge as the ion at the site where it is doping and aliovalent dopants have a different charge from the ion it is replacing. While these defects can exist as isolated species, defects tend to form complex clusters. Point defects are usually charged and the charge can consist of holes left over from the removal of an atom from the lattice (lattice defects) or from the addition or removal of electrons (electronic defects) caused by for example aliovalent doping. In this thesis, we use the well established notation of Kroger-Vink created in 1953 [13]. The Kroger-Vink notation uses three labels to define the defect species,

$$V_{Ti}''''' \tag{2.27}$$

The three labels consist of the defect species, the occupying site and the charge state. The defect species is indicated by the atomic symbol and the type of defect, in this case *V* for vacancy. The occupied site is shown by the subscript atomic symbol. The charge state of the defect relative to the difference in charge of the defect site is given by either a dot (˙) or prime (/) for an extra positive or negative charge, respectively. In the case of a defect with the same charge as the defect site in the perfect crystal, a superscript × is used. Equation (2.27) assumes that the Ti vacancy has a formal effective charge of -4 resulting from the Ti^{4+} ion leaving the site. This 4- charge may be fully localised at the site or may be spread over the neighbouring ions.

Atomistic simulation methods can provide information on the energetics of such processes as well as the consequences on the lattice structure (see [14] for further details). This section demonstrates some of the theory involved in defect chemistry and for the simulations.

2.7.1 The Law of Mass Action

The law of mass action is used to analyse the often complex myriad of defects and defect clusters in a solid by relating them using equilibrium constants that are only dependent on the temperature and pressure. By calculating the Gibbs free energies of all the potential defects in a system, the equilibrium constants can be determined. Formation of a Schottky defect in NaCl (one Na^+ cation vacancy and one Cl^- anion vacancy) can be written as,

$$Na_{Na} + Cl_{Cl} + V_{Na,S} + V_{Cl,S} \rightleftharpoons V'_{Na} + V^{\bullet}_{Cl} + Na_{x,S} + Cl_{x,S} \qquad (2.28)$$

where S represents surface sites i.e. two bulk ions relocating to the crystal surface to leave two vacancies. In a crystal the number of surface sites is constant with a constant total surface area. Therefore, the number of Na^+ and Cl^- ions at the surface is also constant. The equilibrium constant ($\varphi(T)$) is related to the concentration of each species as follows,

$$\varphi'(T) = \frac{[V_{Na}^{/}][V_{Cl}^{\bullet}]}{[Na_{Na}][Cl_{Cl}]} \tag{2.29}$$

where the concentrations of atoms at their own sites are constants so that,

$$\varphi(T) = [V_{Na}^{/}][V_{Cl}^{\bullet}] \tag{2.30}$$

In this expression, the equilibrium constant is dependent on temperature and pressure and the following general equation is obeyed,

$$\varphi(T) \propto \exp(-\Delta G \ / k_B T) \tag{2.31}$$

where ΔG is the free energy change for the forward reaction.

It is noteworthy that for all the defects in the materials featured in this work, only the bulk defect chemistry is considered, which is likely to differ significantly from the surface defect chemistry. Furthermore, it is always assumed that the defects are in the dilute limit (concentrations can be equated to activities, to a good approximation) and are therefore independent, except where explicitly stated otherwise i.e. vacancy pairs or binding clusters. Point defect equilibria can also be studied using statistical thermodynamics. The free energy is expressed in terms of the partition function which is then minimised to obtain the equilibrium condition [15].

2.7.2 Defects in Thermal Equilibrium

At T = 0 K and constant pressure, the ground state of a system is found by minimising the total enthalpy. At finite temperatures, however, the Gibbs free energy (G) is used to define the equilibrium state of the system,

$$G = H - TS \tag{2.32}$$

where H is the enthalpy and S is the entropy. When defects are introduced into a solid state system, strain is caused by the movement of neighbouring atoms and the expansion of the lattice. Although this process involves an enthalpic cost, it is

outweighed by the entropic benefits. For a simple vacancy with N atomic sites, the work done (Gibbs free energy) can be expressed as three terms (G_0, G_1 and G_2). In the dilute limit and at equilibrium the concentration of vacancies is given by,

$$\frac{\partial G}{\partial n} = \frac{\partial}{\partial n}\left(G_0 + G_1 + G_2\right) = 0 \tag{2.33}$$

G_0 represents the perfect crystal, G_1 is equal to ng (Gibbs free energy for creating n vacancies) and G_2 is equal to $-TS_{\text{config}}$ (configurational entropy). For a perfect crystal $n = 0$ and $\partial G_1/\partial n$ is g equation (2.33) can be reduced to,

$$G - T\frac{\partial}{\partial \mathrm{n}}\left(S_{config}\right) = 0 \tag{2.34}$$

The vacant lattice sites can be arranged in P_L ways. The configurational entropy is then given by $k_B \ln P_L$,

$$P_L = N!/[(N-n)!] \tag{2.35}$$

$$S_{config} = k_B \ln\{N!/[(N-n)!n!]\} \tag{2.36}$$

Stirling's theorem states that at high values of x, $x \ln x - x$ is a good approximation of $\ln(x!)$. If this is applied to $n!$, $N!$ and $(N - n)!$ (assuming they are all large values) then $T\partial S_{\text{config}}/\partial n$ can be found from,

$$T\frac{\partial \mathrm{S}_{\text{config}}}{\partial \mathrm{n}} = k_B T \ln\left(\frac{N-n}{n}\right) \tag{2.37}$$

When the defect concentration (f or simply n/N) is small, the right-hand side of equation (2.37) can be reduced to simply $-k_B T \ln f$. By collecting the terms together, the vacancy concentration, f, can be found,

$$g + k_B T \ln f = 0 \tag{2.38}$$

which rearranges to gives,

$$f = \exp\left(-g/k_B T\right) \tag{2.39}$$

This proves the vacancy concentration is dependent upon the Gibbs free energy and increases exponentially with temperature. It also proves that defects must exist in an ideal crystal when the temperature is above 0 K. It is noteworthy to add this is only true for a single defect type in the crystal and that in an ionic crystal more than one single defect type must be considered to ensure charge neutrality. Also it must be stressed that this is a simple example used to convey some of the concepts involved and does not take into account factors such as the energy contribution from internal degrees of freedom. The reader is directed to [16] and [17] for a more complete description.

2.7.3 Mott-Littleton Approximation

There are two general approaches taken to calculating the energetics of defects in solid-state systems, the supercell approach and the embedded cluster approach. The supercell approach is used when defect concentrations extend far beyond the dilute limit and where significant defect-defect interactions are expected. This method is ideal for simulations of solid solutions. For the calculations presented in this section of the work, defects are considered at the infinitely dilute limit where the embedded cluster approach (Mott-Littleton method) is appropriate. The Mott-Littleton approximation divides the area around a defect into two spherical regions where in region 1 the atomic interactions are treated explicitly and the interactions in region 2 are approximated. Region 2 can also be divided into two sections (2a and 2b) as shown by figure 2.4 [18-19].

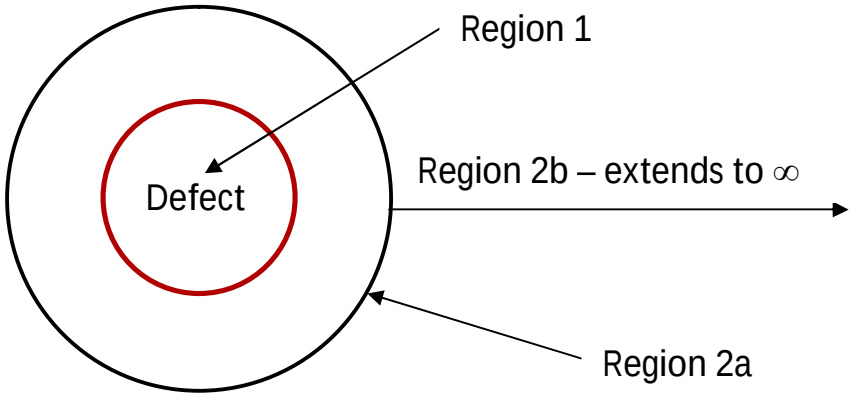

Figure 2.4: Schematic representation of the Mott-Littleton approximation.

The ions in region 1 are strongly perturbed by the defect and therefore the interactions must be calculated explicitly using Coulombic interactions and inter-atomic potentials. Further away from the defect, the perturbations become weaker so approximations based on continuum theory can be used. In region 2a, the displacements of the ions are calculated using the Mott-Littleton approximation but the interaction energies with ions in region 1 are calculated explicitly. The energies of region 2b ions are not calculated explicitly although it is assumed that they respond harmonically. The energy for region 2b in a diagonally cubic case is given by,

$$E = -\frac{Q^2}{8\pi\varepsilon_0}\sum_{i\varepsilon 2b}\frac{M_i}{|R_i|^4} \tag{2.40}$$

where ε_0 is the static dielectric constant, R_i is the distance of the ith atom from the defect centre and M_i is the Mott-Littleton parameter for the sub-lattice and can be expressed as

$$M_i = \left(\frac{\alpha_i}{\sum_j \alpha_j}\right)\left(1-\frac{1}{\varepsilon}\right) \tag{2.41}$$

where α_j is the polarisability of the jth sub-lattice.

For the anisotropic case, the following form is taken,

$$E = -\frac{Q^2}{8\pi\varepsilon_0}\sum_{i\varepsilon 2b}\sum_{\alpha\beta}\frac{M_i^{\alpha\beta}R_i^{\alpha}R_i^{\beta}}{|R_i|^6} \tag{2.42}$$

where α,β denote the Cartesian directions and $M_i^{\alpha\beta}$ is the generalised Mott-Littleton parameter [20].

The total energy of all regions is described by,

$$E = E_1(x) + E_{12}(x,\xi) + E_2(\xi) \tag{2.43}$$

where E_1 and E_2 are the energies of the inner and outer regions, respectively and E_{12} is the interaction between the two regions. Atomic coordinates and displacements are represented by x (inner region) and ξ (outer region), respectively.

The energy of the outer region (E_2) is treated harmonically and is therefore represented by a quadratic function of the displacements,

$$E_2(\xi) = \frac{1}{2}\xi^T H_2 \xi \tag{2.44}$$

where H_2 is the Hessian matrix for region 2. At equilibrium, the energy with respect to the displacements is zero and so we can obtain,

$$\left(\frac{\partial E(x,\xi)}{\partial \xi}\right)_x = \left(\frac{\partial E_{12}(x,\xi)}{\partial \xi}\right)_x + H_2\xi = 0 \tag{2.45}$$

Through combination of equations (2.43) and (2.45), the energy E_2 can be eliminated to give an equation for the total energy,

$$E = E_1(x) + E_{12}(x,\xi) - \frac{1}{2}\left(\frac{\partial E_{12}(x,\xi)}{\partial \xi}\right)_x \xi \tag{2.46}$$

This implies that the total energy can now be found by direct minimisation of E with respect to the displacements. However, as the displacements in the outer region are a function of the inner region coordinates, an analytical expression is not available. The solution to this complication is to ensure the force on each region 1 ion is zero. This solution also requires the ions in region 2 to be in equilibrium. In region 2b it is assumed that the only force acting upon the ions is Coulombic. This is certainly true when the value of the radius of region 2a is larger than that of region 1 by the interatomic potential cutoff value in the simulation.

The correct choice of region size is important in ensuring accurate defect energies. If the region size selected is too small and the energy has not converged, significant variations from the correct result can be produced. The defect calculations in this work have used a minimum region 1 size of 13 Å to ensure convergence as shown by figure 2.5.

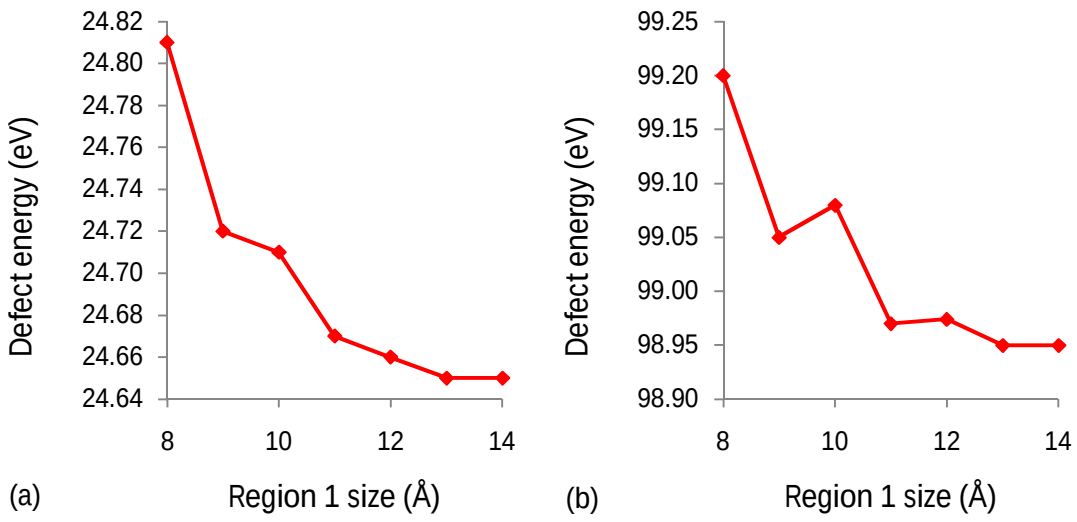

Figure 2.5: Illustration of defect energy convergence with the Mott-Littleton region1 size for (a) – an O vacancy and (b) – a Ti vacancy.

2.8 Molecular Dynamics

Molecular dynamics (MD) is a powerful simulation tool that allows the motion of the atoms in a system to be studied directly. MD is a classical technique which relies on the Born-Oppenheimer approximation. As a result it uses many of the previously discussed techniques and approaches including the use of interatomic potentials to model the short-range interactions. In this work, we have used the same potential models for the lattice statics and MD calculations. From the forces calculated by the potentials, Newton's equations of motion can be solved and then used to calculate the atomic positions and velocities. Unlike lattice statics methods, temperature is now explicitly accounted for in the simulation. MD also has the advantage of being able to study properties that are time dependent such as diffusion and structural transitions. MD has found many applications in modelling not only ionic solids, but biological systems [21] and metals [22] to name but a few. Classical MD has also become a popular technique for modellers as it can handle systems with many thousand atoms or molecules, whereas *ab initio* methods are limited to hundreds of atoms or molecules. The following sections

provide an overview of the MD methodology. For a more detailed description of the theory behind MD, the reader is directed to [23-24].

2.8.1 Classical Mechanics

Molecular dynamics simulations are based on the Newton's second law, the equation of motion,

$$F_i = m_i a_i \tag{2.47}$$

where F_i is the force exerted on particle i, m_i is the mass of particle i and a_i is its acceleration. As discussed, MD is deterministic, meaning that when the positions and velocities of the atoms have been calculated, the future state of the system can be predicted. The energy of a system is the sum of the potential, $U(\boldsymbol{r}_N)$, and the kinetic, $K(\boldsymbol{p}_N)$, energies summed over the positions $\boldsymbol{r}^N = (\boldsymbol{r}_1, \boldsymbol{r}_2 \ldots \boldsymbol{r}_N)$ and momenta $\boldsymbol{p}^N = (\boldsymbol{p}_1, \boldsymbol{p}_2 \ldots \boldsymbol{p}_N)$ of all N atoms. The energy can be given in a Hamiltonian form,

$$\hat{H}(\boldsymbol{r}, \boldsymbol{p}) = K(\boldsymbol{p}^N) + U(\boldsymbol{r}^N) \tag{2.48}$$

The potential energy is defined using the potential models that are discussed in section 2.3. The kinetic energy is given by,

$$K = \sum_{i=1}^{N} \frac{p_i^2}{2m_i} \tag{2.49}$$

Hamilton's equations can be applied to equation (2.47) to produce first order differential equations capable of describing the change in position and momenta of each atom over time,

$$\dot{\boldsymbol{p}}_i = -\frac{\partial}{\partial \boldsymbol{r}} \hat{H} = -\frac{\partial}{\partial \boldsymbol{r}} U(\boldsymbol{r}) = \boldsymbol{f}_i \tag{2.50}$$

$$\dot{\boldsymbol{r}}_i = -\frac{\partial}{\partial \boldsymbol{p}} \hat{H} = \frac{\boldsymbol{p}_i}{m_i} \tag{2.51}$$

Although these expressions are reasonable to solve, even for large systems, a problem arises when they need to be solved efficiently while still remaining accurate as this can be computationally very expensive. As is the case with energy minimisation in lattice statics methods, it is again the calculation of the derivative of the potential energy that is the most computationally expensive part of the calculation. Numerous numerical algorithms have been developed for integrating the equations of motion and will be discussed in the following section. The choice of time step in any MD simulation is a crucial decision, if the time step is too long, the simulation will not be as accurate and if the time step is too short it will be impractical to run the simulation for a long enough period to gain valid results. The choice of time step and other factors including the conservation of energy and momentum and computationally efficiency should determine the choice of integrating algorithm.

2.8.2 Integrating Algorithms

The simplest method for solving the equations of motion is the finite-difference method. The application of finite-difference methods to the equations of motion was pioneered by Verlet [25]. The information on the dynamics and positions of the atoms in the system at a given time *t* is used to propagate the properties for the following time steps. This information can be approximated by a Taylor series expansion, as shown by this example for the positions,

$$\boldsymbol{r}(t+\Delta t) = \boldsymbol{r}(t) + \boldsymbol{v}(t)\Delta t + \frac{\boldsymbol{f}(t)}{2m}\Delta t^2 + \frac{\Delta t^3 ...}{3!}\boldsymbol{r} + O(\Delta t^4)... \tag{2.52}$$

Similar expressions can be derived for the velocities and accelerations which are used to further propagate the other related properties. While this method is capable of iteratively updating the forces which in turn give updated information on the accelerations and correct the previously calculated positions, it is also computationally demanding. Although this correction step provides accurate information, the re-calculation of the forces is an expensive process and it may take numerous iterations to fully equilibrate.

The Verlet integrating algorithm is a method which avoids this problem as it only requires a single calculation of the force at every time step. This option is one of the most used in MD simulations as it is simple to use and is compact meaning that only modest storage is required. Many of the other commonly used integration algorithms including the Leapfrog and the Velocity Verlet [1] algorithms are based on the Verlet scheme. The Verlet algorithm combines the Taylor expansion for the propagation of the positions (equation (2.52)) with the Taylor expansion for the preceding step,

$$\boldsymbol{r}(t-\Delta t)=\boldsymbol{r}(t)-\boldsymbol{v}(t)\Delta t+\frac{\boldsymbol{f}(t)}{2m}\Delta t^2-\frac{\Delta t^3}{3!}\boldsymbol{r}+O(\Delta t^4)... \tag{2.53}$$

By summing these two expressions, the positions of the next step, $\boldsymbol{r}(t + \Delta t)$, can be calculated provided the previous positions, $\boldsymbol{r}(t - \Delta t)$,have been stored,

$$\boldsymbol{r}(t+\Delta t)=2\boldsymbol{r}(t)-\boldsymbol{r}(t-\Delta t)+\frac{\boldsymbol{f}(t)}{2m}\Delta t^2+O(\Delta t^4) \tag{2.54}$$

When these expressions are combined, the velocity terms cancel each other out and therefore must be calculated directly from the difference between the two equations,

$$\boldsymbol{r}(t+\Delta t)-\boldsymbol{r}(t-\Delta t)=2\boldsymbol{v}(t)\Delta t\ \ +O(\Delta t^3)+... \tag{2.55}$$

$$\boldsymbol{v}(t)=\frac{\boldsymbol{r}(t+\Delta t)-\boldsymbol{r}(t-\Delta t)}{2\Delta t}+O(\Delta t^2) \tag{2.56}$$

The main drawback to this algorithm is unless that many variables are stored, the accuracy of the velocities is modest and of the order of Δt^2. The velocities also have to be calculated at every time step so that important system properties including the total energy and temperature can be calculated. The leapfrog variant of this algorithm provides an improved method of calculating the velocities. The leapfrog algorithm has been used for all the MD simulations completed in this work.

In the leapfrog algorithm the positions are propagated by calculating the velocities at half time steps. It is based on the following equations,

$$\boldsymbol{r}(t+\Delta t) = \boldsymbol{r}(t) + \Delta t \boldsymbol{v}(t+\frac{1}{2}\Delta t) \tag{2.57}$$

$$\boldsymbol{v}(t+\frac{1}{2}\Delta t) = \boldsymbol{v}(t-\frac{1}{2}\Delta t) + \frac{\boldsymbol{f}(t)}{m}\Delta t + O(\Delta t^3) \tag{2.58}$$

The velocities, $\boldsymbol{v}(t + ½t)$, are first calculated from the velocities at time $t - ½\Delta t$ and the accelerations at time t. These values are then used to calculate the updated positions as shown by equation (2.56). Essentially, the velocities leap over the positions to calculate the position values and the positions then leap over the velocities to calculate the new velocity values and so on. Similar to the Verlet algorithm, the leapfrog algorithm is easy to compute. However, it does have important advantages over the Verlet algorithm, it explicitly calculates the velocities (although not at the same time as the positions) and does not need to calculate the differences between equations (2.52) and (2.53).

2.8.3 Statistical Mechanics

Statistical mechanics plays an essential role in molecular dynamics as it provides the link between the interactions at the atomic level and the macroscopic properties of the system.

The thermodynamic state of a given N-body system can usually be defined by a set of variables which include temperature T, pressure P, volume V and the number of atoms N. In such a system, there are an unlimited number of possible configurations which can each be individually defined in terms of the position vectors, $\boldsymbol{r}^N$, and momenta, $\boldsymbol{p}^N$, of each atom. Each of these points is deemed a phase point, $\Gamma(\boldsymbol{r}^N, \boldsymbol{p}^N)$, and together they form phase space. It is these phase points that control the microscopic state of the system.

Only a selection of these phase points, however, are used to satisfy the conditions of a given thermodynamic state, this selection of phase points is known as an *ensemble*. A

number of different ensembles exist and vary by which thermodynamic quantities are preserved. These ensembles are described in more detail in section 2.8.4.

In an ensemble, the macroscopic properties of the system are based on the average properties of the phase points in that ensemble, i.e. the ensemble average. Ensemble averages capable of accurately replicating the properties of experimental samples, even given the massive amount of conformations in such a sample. Ensemble averages are calculated from the probability of a given phase point occurring,

$$p_{\text{ens}}(\Gamma) = \frac{w_{\text{ens}}(\Gamma)}{Q_{\text{ens}}} \tag{2.59}$$

where w_{ens} is a weight function that describes the likelihood of a particular state and Q_{ens} is the partition function which acts as a normalising factor that is simply the sum of all of the weights,

$$Q_{\text{ens}} = \sum_{\Gamma} w_{\text{ens}}(\Gamma) \tag{2.60}$$

In statistical mechanics, the partition function acts as the bridge between the microscopic and macroscopic properties of the system. The ensemble average of an observable, A, can be estimated using the partition function,

$$\langle A \rangle_{\text{ens}} = \sum_{\Gamma} \frac{w_{\text{ens}}(\Gamma) A(\Gamma)}{Q_{\text{ens}}} \tag{2.61}$$

Therefore, in order to calculate an accurate representation of the macroscopic properties of the system, an accurate estimation of the partition function is essential. However, the partition function cannot be explicitly calculated as it is based on all the infinite possible states of the system. This is why MD and other simulation methods such as Monte Carlo simulations [26] rely on the preferential sampling of configurations. It is noteworthy to add that unlike in MD, the sampling in Monte Carlo simulations is stochastic rather than deterministic. In MD, the rate of sampling for a phase point is made proportional to $p_{\text{ens}}(\Gamma)$, which has a distribution based on the ensemble it is being sampled from. This allows the accuracy of the partition function to improve with the

length of time the simulation runs for. This is known as the ergodic hypothesis, where the ensemble average equals the time average.

This hypothesis proposes that if a system could be simulated on an infinite time scale, the system would eventually move through each possible state. Therefore, it is essential that such simulations must be completed over an appropriate time scale, so that the necessary amount of phase space is sampled, especially when the data is used to extract the properties of the system. Given this hypothesis, the ensemble average (equation (2.61)) can now be re-written as a product of the average discrete time-steps, τ_{obs}, in the simulation,

$$\langle A \rangle_{ens} = \frac{1}{\tau_{obs}} \sum_{\tau=1}^{\tau_{obs}} A(\Gamma(\tau)) \tag{2.62}$$

2.8.4 Statistical Ensembles

There are a several types of ensemble each with different characteristics and properties. The most simple of these is the microcanonical ensemble (*NVE*), here the number of atoms, *N*, the volume, *V*, and the energy, *E*, are all fixed. This ensemble represents an isolated system and therefore the useful properties that can be extracted from the simulation are somewhat limited. In the canonical ensemble (*NVT*) the number of atoms, the volume and the temperature are all fixed. For the isobaric-isothermal ensemble (*NPT*) the number of atoms, the pressure and the temperature are fixed, but the volume of the system can now adjust to the pressure and temperature. The final ensemble covered here is the grand canonical ensemble (μVT), where the chemical potential, μ, volume and temperature are all fixed.

When the ensemble requires the temperature to be fixed for the MD simulation, we need a method of controlling it. This is done using a thermostat, where the system is coupled to an external heat bath at the desired temperature. For ensembles at constant pressure, a barostat is used which is considered as a piston that reacts to pressure changes by altering the volume accordingly. There are numerous thermostats used in

MD simulations which include the Anderson [27], the Berendsen [28] and the Nosé-Hoover thermostats. We will focus on the Nosé-Hoover thermostat in this section.

Unlike some thermostats, the Nosé-Hoover thermostat generates states in the canonical ensemble. Usually Newton's equations only conserve energy in the *NVE* ensemble; however, this thermostat allows the equations of motion to be altered so that the canonical ensemble can also be applied. The Nosé-Hoover thermostat adds the effect of constant temperature by introducing an extra degree of freedom (*s*) and the conjugate momentum so that the Hamiltonian can be written as,

$$\hat{H} = \sum_i \frac{p_i^2}{2m_i s^2} + U(\boldsymbol{r}^N) + \frac{p_s^2}{2Q} + (3N+1)k_B T \ln s \tag{2.63}$$

where Q controls the coupling of the heat bath to the system and must be chosen to ensure that a canonical distribution is achieved. This thermostat can also be extended so that it can be used for *NPT* ensembles. For this a barostat must be added to maintain constant pressure by rescaling the system size after each time step in addition to the trajectories. The pressure can be constrained by including terms to account for volume fluctuations and by adding in another degree of freedom that corresponds to inertia for the volume fluctuations. The Nosé-Hoover thermostat-barostat has been used in all of our *NPT* MD calculations.

2.9 Conclusions

In this chapter we have attempted to give an overview of the classical potential-based techniques used in this thesis. We have described the importance and applications of potentials and their importance in simulation techniques including lattice statics and molecular dynamics. Descriptions of other important methods including energy minimisation, Ewald summation, the Shell model and the Mott-Littleton approximation have also been provided. An introduction into point defects and their thermodynamic properties is also given. Finally, the fundamentals of molecular dynamics simulation have been explained through the relationship between statistical and classical mechanics.

References

[1] A. R. Leach, *Molecular Modelling: Principles and Applications* (Pearson Prentice Hall, Dorset, 2001).

[2] J. H. Harding, Reports on Progress in Physics **53**, 1403 (1990).

[3] D. Frenkel and B. Smit, *Understanding Molecular Simulation: From Algorithms to Applications* (Academic Press, San Diego, 2002).

[4] M. Born and R. Oppenheimer, Annalen der Physik **389**, 457 (1927).

[5] P. M. Axilrod and E. Teller, Journal of Chemical Physics **11**, 299 (1943).

[6] B. G. Dick and A. W. Overhauser, Physical Review **112**, 90 (1958).

[7] P. P. Ewald, Annals of Physics **369**, 253 (1921).

[8] J. D. Gale and A. L. Rohl, Molecular Simulation **29**, 291 (2003).

[9] G. P. Srivastava, *The Physics of Phonons* (Taylor and Francis Group, New York, 1990).

[10] C. G. Broyden, Mathematics of Computation **24**, 365 (1970).

[11] R. Fletcher, Computer Journal **13**, 317 (1970).

[12] D. Goldfarb, Mathematics of Computation **24**, 23 (1970).

[13] F. Kroger and H. Vink, *Solid State Physics* (volume 3, Academic Press, New York, 1956).

[14] C. R. A. Catlow and W. C. Mackrodt, *Computer Simulation of Solids* (Springer-Verlag, Berlin, 1982).

[15] A. R. West, *Basic Solid State Chemistry* (John Wiley & Sons Ltd., Chichester, 1999).

[16] W. Hayes and A. M. Stoneham, *Defects and Defect processes in Nonmetallic Solids* (Dover publications, New York, 2004).

[17] L. A. Girifalco, *Statistical Physics of Materials* (John Wiley & Sons Ltd., New York, 1973).

[18] C. R. A. Catlow, Journal of the Chemical Society, Faraday Transactions 2 **85**, 335 (1989).

[19] A. B. Lidiard, Journal of the Chemical Society, Faraday Transactions 2 **85**, 341 (1989).

[20] C. R. A. Catlow, R. James, W. C. Mackrodt and R. F. Stewart, Physical Review B **25**, 1006 (1982).

[21] C. L. Freeman, J. H. Harding, D. Quigley and P. M. Rodger, Physical Chemistry Chemical Physics **14**, 7287 (2012).

[22] C. F. Sanz-Navarro, P.- O. Åstrand, D. Chen, M. Rønning, A. C. T. van Duin and W. A. Goddard, Journal of Physical Chemistry C **114**, 3522 (2010).

[23] M. P. Allen and D. J. Tildesley, *Computer Simulation of Liquids* (Oxford University Press, USA, 1989).

[24] D. C. Rapaport, *The Art of Molecular Dynamics Simulation* (Cambridge University Press, 2004).

[25] L. Verlet, Physical Review **159**, 201 (1967).

[26] N. Metropolis and S. Ulam, Journal of the American Statistical Association **44**, 335 (1949).

[27] H. C. Andersen, Journal of Chemical Physics **72**, 2384 (1980).

[28] H. J. C. Berendsen, J. P. M. Postma, W. F. van Gunsteren, A. DiNola and J. R. J. Haak, Journal of Chemical Physics **81**, 3684 (1984).

3

Quantum Mechanical Methods

3.1 Introduction

While classical methods are capable of simulating systems with many thousands of atoms and beyond, it can only ever approximate the interactions between these atoms. Therefore, quantum mechanical methods (QM) are necessary for simulating systems where the approximations of classical mechanics do not provide enough detail or fail completely. The popularity of QM methods increased dramatically during the latter part of the 20^{th} century and still continues to increase today with further advances in computational power. QM simulations work by using approximations to solve the many-body problem. One of the most used methods for this is density functional theory (DFT). In this chapter we outline the basic theory of these methods and how to apply them to solid state systems. Special attention is given to the method that we have used in this work, DFT. The VASP [1] simulation package has been used for all the DFT calculations in this work. At this point we direct the reader to the literature for a more detailed description of these methods [2-3].

3.2 The Hamiltonian

Schrödinger's equation cannot be solved analytically when the system has more than two particles. This issue is known as the many body problem and can be solved by numerical methods. The energy of a system can be calculated from the time independent Schrödinger equation,

$$H\Psi = E\Psi \tag{3.1}$$

QM methods also make use of the Born-Oppenheimer approximation [4]. As discussed in chapter 2, this approximation allows the nuclei to be treated as stationary which means the electronic wavefunction can be calculated independent of the nuclear wavefunction. This effectively decouples the wavefunctions of the electrons and the nuclei so that,

$$\Psi(r, R) = \varphi(r; R)\phi(R) \tag{3.2}$$

where r represents the electronic coordinates, R represents the nuclear coordinates, φ represents the electronic wavefunction and ϕ represents the nuclear wavefunction. The Hamiltonian (in atomic units) in equation (3.1) can be expressed in terms of the kinetic energy, the external potential, the electron-electron interaction term and finally the nuclei-nuclei interaction term. This produces the Born-Oppenheimer electronic Hamiltonian,

$$\hat{H} = -\frac{1}{2}\sum_{i}^{n}\nabla_i^2 - \sum_{iA}^{nN}\frac{Z_\alpha}{r_{iA}} + \sum_{i<j}^{n}\frac{1}{r_{ij}} + \sum_{A<B}^{N}\frac{Z_A Z_B}{R_{AB}} \tag{3.3}$$

where nuclei are denoted by upper case letters and electrons are denoted by lower case letters, r is the separation between atoms and Z is the nuclei charge. The nuclei interaction term in the electronic Hamiltonian expression can be treated as a constant value. This reduces equation (3.1) to a more succinct expression,

$$\hat{H} = \hat{T} + \hat{V} + \hat{U} \tag{3.4}$$

where $\hat{T}$ is the kinetic energy of the electrons, $\hat{V}$ is the external potential and $\hat{U}$ is the electronic Coulombic interaction. Although the Born-Oppenheimer approximation reduces the many body problem to a many electron problem, the complexity of the electronic Schrodinger equation still means the wavefunction cannot be calculated exactly. This fundamental problem forms the basis of all electronic simulation theory covered in the remainder of this chapter.

3.3 Density Functional Theory

The basis of DFT comes from the earlier Hartree-Fock theory [5-7]. This theory works by providing an approximation of the ground-state wave function and energy of a many body system. This approximation is dependent on treating the particles in the system independently and that the wavefunction can be given by a single Slater determinant of *N* spin-orbitals. This allows an accurate description of the system to be formed and therefore acts as a benchmark for other QM simulations.

DFT calculations make use of the ground state electron probability density, *p*(r), to calculate the ground state energy and other important molecular properties. This principle reduces the complex *N* electron wave function to a far simpler single particle electron density. The electronic energy of the system, *E*, can be expressed as a function of the electron density, *p*(*x*,*y*,*z*),

$$E = E_v[p] \tag{3.5}$$

where *p* defines the number of electrons, *n*, assuming that the wavefunction has been normalised,

$$n = \int p(r)dr \tag{3.6}$$

The theoretical proof that links the ground state electron density to the physical properties of the system was developed by Hohenberg and Kohn [8-9] in the 1960s.

3.3.1 The First Hohenberg-Kohn Theorem

The first Hohenberg-Kohn theorem states that the electron density determines the external potential of the system (see equations (3.3) and (3.4)). Therefore, since the Hamiltonian is determined by the external potential, the ground state energy and other ground state properties can be determined from the ground state electron density. By using the variational principle [10] and by minimising the energy function, the wavefunction and energy can be found,

$$E[\Psi] = \frac{\left\langle \Psi \middle| \hat{H} \middle| \Psi \right\rangle}{\left\langle \Psi \middle| \Psi \right\rangle} \tag{3.7}$$

This theory can be proven by assuming we have two different external potentials, $V_A(r)$ and $V_B(r)$, that both give rise to the same ground state electron density, $\rho(r)$. Both of these external potentials have different associated Hamiltonians, H_A and H_B, and ground state wave functions, Ψ_A and Ψ_B, which therefore produce different ground state energies, $E_{0\,(A)}$ and $E_{0\,(B)}$.

Again using the variational theorem and by considering one of the wave functions as the true wavefunction (Ψ_A) and the other as a trial wavefunction (Ψ_B) for H_A that will produce a higher energy than the ground state energy, we can write,

$$\begin{aligned} E_{0(A)} &< \left\langle \Psi_B \middle| H_A \middle| \Psi_B \right\rangle = \left\langle \Psi_B \middle| H_A + H_B - H_B \middle| \Psi_A \right\rangle \\ &= \left\langle \Psi_B \middle| H_A - H_B \middle| \Psi_B \right\rangle + \left\langle \Psi_B \middle| H_B \middle| \Psi_B \right\rangle \end{aligned} \tag{3.8}$$

Given that the Hamiltonians only differ by their respective external potential and that these external potentials are one electron operators that are treated independently, the difference in ground state energies can be written as,

$$E_{0(A)} < E_{0(B)} + \int \left[V_A(r) - V_B(r) \right] \rho(r) dr \tag{3.9}$$

and similarly for $E_{0\,(B)}$,

$$E_{0(B)} < E_{0(A)} + \int \left[V_B(r) - V_A(r) \right] \rho(r) dr \tag{3.10}$$

As the ground state electron densities are the same for both external potentials, we can combine equations (3.9) and (3.10) to cancel the integrals. This produces a contradiction that proves that two different external potentials cannot produce the same ground state energy and that for any given $\rho(r)$ there can only be one corresponding $V(r)$,

$$E_{0(A)} + E_{0(B)} < E_{0(A)} + E_{0(B)} \tag{3.11}$$

3.3.2 The Second Hohenberg-Kohn Theorem

The second Hohenberg-Kohn theorem states that the ground state energy can be obtained variationally on the basis that the electron density that minimises a functional for the energy is the exact ground state energy. Therefore an electronic energy functional of the density, $E_V[\rho(r)]$, can be defined as,

$$E_V[\rho(r)] = F_{\mathrm{HK}}[\rho(r)] + \int V(r)\rho(r) dr \tag{3.12}$$

$$F_{HK}[\rho(r)] = \left\langle \Psi \left| T + V \right| \Psi \right\rangle \tag{3.13}$$

where $F_{\mathrm{HK}}[\rho(r)]$ is the Hohenberg-Kohn functional and the other terms have the same meaning as previously defined.

For a particular value of $V(r)$, the ground state energy is the equivalent to the global minimum of $E_V[\rho(r)]$ and the density that minimises this functional is the ground state density. This produces the variational principle of the second Hohenberg-Kohn theorem,

$$E_0 \leq E_V[\rho(r)] \tag{3.14}$$

This would allow for the direct calculation of the ground state energy and density. However, this can only happen if we know the form of the Hohenberg-Kohn functional, which of course we do not. While these theorems are extremely useful for describing the nature of electron density and its relation to the physical properties of a system, they do not give a practical framework for actually computing the ground state electron density. Therefore an accurate and reliable solution for this calculation is still required, as will be discussed in the next section.

3.3.3 The Kohn-Sham Approach

Shortly after the pioneering of Hohenberg and Kohn, Kohn and Sham [11] developed a theory that enables the calculation of the ground state energy of a system. The method involves replacing the system of interest with a fictitious reference system with non-interacting electrons but with the exact same ground state electron density. This reference system is used to approximate the kinetic and electron Coulombic repulsion functional. The second Hohenberg-Kohn theorem shows that the ground state energy of a many electron system can be calculated from minimising the energy functional, F_{HK}, that contains the terms for the electron's kinetic energy and their interaction with the external potential (equations (3.12) and (3.13)). The Hamiltonian of the reference non-interacting system can be written as,

$$\hat{H}_S = -\frac{1}{2}\sum_{i=1}^{N}\nabla_i^2 + \sum_{i=1}^{N}V_{KS}(r_i) \tag{3.15}$$

where $V_{KS}(r_i)$ is an effective local potential known as the Kohn-Sham potential (discussed below).

The ground state wavefunction of the reference system with density $p(r)$ can be written using a Slater determinant,

$$\Psi_S = \frac{1}{\sqrt{N!}}\det[\phi_1\phi_2...\phi_N] \tag{3.16}$$

where the Kohn-Sham orbitals $\phi_i(r)$ are the N lowest eigenstates of the one electron Hamiltonian $\hat{h}_S$,

$$\hat{h}_S \phi_i(r) = \left[-\frac{1}{2}\nabla^2 + V_{KS}(r) \right] \phi_i(r) = \varepsilon_i \phi_i(r) \tag{3.17}$$

This allows the kinetic energy, T_S, to be directly calculated from the orbitals, similarly to Hartree-Fock theory,

$$T_S = -\frac{1}{2}\sum_{i=1}^{N} \left\langle \phi_i(r) \middle| \nabla^2 \middle| \phi_i(r) \right\rangle \tag{3.18}$$

It is noteworthy to add that T_s in this equation is not equal to the kinetic energy of the real interacting system, but simply the kinetic energy of the reference non-interacting system for the corresponding true ground state density,

$$\rho(r) = \sum_{i=1}^{N} \left| \phi_i \right|^2 \tag{3.19}$$

Using the Kohn-Sham method and by subtracting T_S from F_{HK} in equation (3.12), an expression for the ground state energy of the Kohn-Sham system can be derived,

$$E_{KS} = T_S[\rho(r)] + J[\rho(r)] + E_{xc}[\rho(r)] + \int V(r)\rho(r)dr \tag{3.20}$$

where

$$J[\rho(r)] = \frac{1}{2}\int \frac{\rho(r)\rho(r')}{\left| r - r' \right|} dr dr' \tag{3.21}$$

is the Hartree energy or the classical Coulomb interaction of the electron density interacting with itself and E_{xc} is the exchange-correlation energy which accounts for the difference in kinetic energy between the real interacting system (T) and the non-interacting system (T_S) and the non-classical contribution from the electron-electron interaction of the real interacting system.

Via the combination of the one electron Hamiltonian expression (equation (3.17)) and the expression for the ground state energy of the Kohn-Sham system (equation (3.20)), the Kohn-Sham equation can be produced,

$$\left[-\frac{1}{2}\nabla^2 + V_{\mathrm{KS}}(r) + \int \frac{\rho(r')}{|r-r'|} dr' + V_{\mathrm{xc}}(r) \right] \phi_i(r) = \varepsilon_i \phi_i(r) \tag{3.22}$$

where

$$V_{\mathrm{xc}}(r) = \frac{\delta E_{\mathrm{xc}}[\rho]}{\delta \rho} \tag{3.23}$$

is the exchange-correlation potential which is the functional derivative of the exchange-correlation energy with respect to density.

The Kohn-Sham equation in principle provides an exact model of the system where the solution can be solved accurately though an iterative procedure as long as E_{xc} is known. Using this equation all the properties can be determined from the correct value of $\rho(r)$. An initial estimate of $\rho(r)$ is used to construct $V_{\mathrm{KS}}(r)$ which in turn is used to calculate a new value of $\rho(r)$. This new value of $\rho(r)$ can also then be used to calculate the Hamiltonian. This cycle is repeated self-consistently until the results for $\rho(r)$ are converged to the necessary degree of accuracy when compared to the value from the previous cycle. Once the correct value for the ground state density has been calculated, it can be used to determine the ground state energy and other important properties of the system.

In summary, the Kohn-Sham method reduces the complicated many-body problem to a set of single particle equations that can be calculated with relative ease and are computationally efficient. This is achieved by considering the real interacting system in tandem with a non-interacting reference system with the same ground state electron density. This method reduces the complex mathematical and physical problems associated with a many-body system to one variable, the exchange-correlation potential. It is noteworthy to add that in this description we have not considered the spin

component of the electrons. Spin-polarisation can be readily incorporated into the Kohn-Sham equation and we direct the reader to [12] for further information.

3.3.4 Exchange-correlation Functionals

The accuracy of a DFT simulation is entirely dependent upon the quality of the approximation made by the exchange-correlation term, $E_{xc}[\rho(r)]$. There are a variety of different functionals used to approximate this term and they are often chosen on the basis of the nature of the system being simulated. One of the most common functionals is the Local Spin Density Approximation (LSDA) [13-15] or the Local Density Approximation (LDA) when the system of interest has no net spin. As the name suggests, this functional relies on the assumption that the local energy depends on the local electron density.

In LDA the electrons are treated as locally homogenous, so that the exchange-correlation energy at a given point is only dependent on the electron density at that same point,

$$E_{xc}^{LDA}[\rho(r)] = \int \rho(r) e_{xc}^{hom}(\rho) dr \tag{3.24}$$

where e_{xc}^{hom} is the exchange-correlation energy density.

The LDA assumes that the exchange-correlation energy density at a given point is the same as in a homogenous electron gas with that density. The exchange energy for the homogenous electron gas can be calculated analytically and the correlation energy can be calculated using Monte Carlo methods [16]. While this functional is good at describing systems with uniform charge density, it is far less capable of dealing with individual atoms and molecules because of the large changes in charge density.

Unfortunately, LDA also has several other inherent failings. One of these is the self-interaction error which results from the fact that the interaction of an electron with itself is not zero for such functionals. This error does not completely cancel in DFT unlike in

the Hartree-Fock method. This creates an additional inaccuracy when simulating inhomogeneous systems such as atoms where the self-interactions terms can be large. Another issue when using the LDA method is the significant underestimation of the band gap of insulating and semiconducting materials. This arises from the inability of the exchange-correlation functionals to describe excited state properties as well as to predict the energy gaps between occupied and unoccupied states [17-18]. The underestimation of band gaps by LDA is shown clearly by figure 3.1.

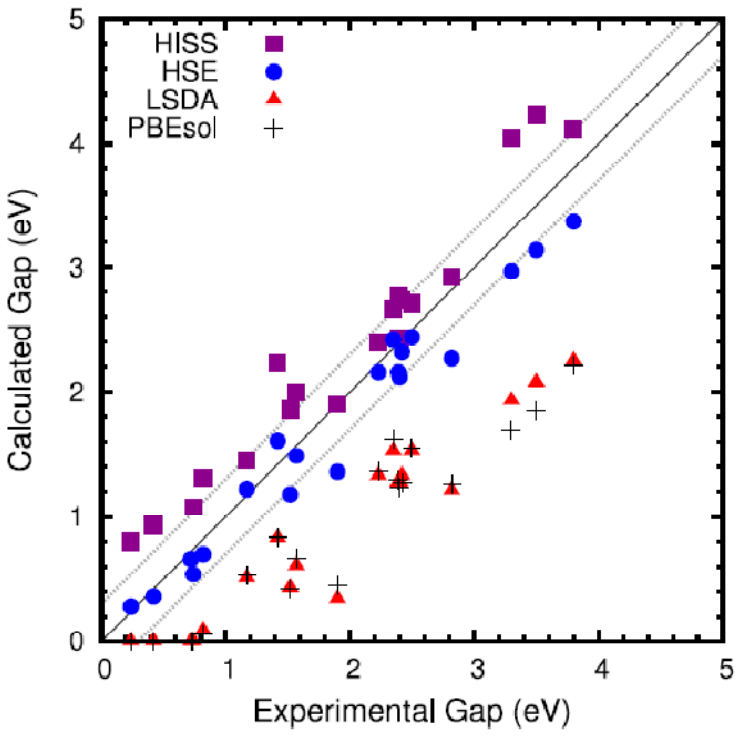

Figure 3.1: A comparison between low-temperature experimental band gaps and band gaps calculated using DFT with a series of different exchange-correlation functionals. All band gaps are for semiconductor materials and are within the visible range [19] (explicit permission to reuse this image has been granted).

Regardless of these disadvantages, LDA is successful in calculating many properties including lattice parameters, vibrational frequencies and the phase stability of many solid systems.

To build upon the success of the LDA approach, the gradient of the density must be included so that semi-local effects can also be analysed and so that the functional is no longer entirely dependent on the local exchange-correlation terms. This is known as the Generalised Gradient Approximations (GGA) and has proven to be a powerful method in simulating a wide range of systems including atoms and molecules. This method also shows some significant improvements on the performance of LDA including the correction of 'overbinding' caused by the large exchange energies for atoms and molecules when using LDA and improved cohesive energies for solids. The GGA functional can be written as,

$$E_{\mathrm{xc}}^{\mathrm{GGA}}[n_{\uparrow}, n_{\downarrow}] = \int \rho(r) e_{\mathrm{xc}}^{\mathrm{GGA}}[n_{\uparrow}, n_{\downarrow}, \nabla n_{\uparrow}, \nabla n_{\downarrow}, ...] dr \tag{3.25}$$

where $e_{\mathrm{xc}}^{\mathrm{GGA}}$ is the exchange-correlation energy density, $n_{\uparrow}$,$n_{\downarrow}$ denotes the spin densities and $\nabla n_{\uparrow}, \nabla n_{\downarrow}$ is the gradient of the density. The energy density can also be written as,

$$e_{\mathrm{xc}}^{\mathrm{GGA}} = e_{\mathrm{x}}^{\mathrm{hom}}(n) F_{\mathrm{xc}} \tag{3.26}$$

where F_{xc} is dimensionless and is known as the exchange enhancement factor and $e_{\mathrm{x}}^{\mathrm{hom}}(n)$ is the exchange energy of the unpolarised gas.

F_{xc} can take numerous forms including the Perdew and Wang (PW91) [20] and Perdew, Burke and Enzerhof (PBE) [21] functionals. PBE is generally considered the most commonly used functional for solid-state systems, although many new and supposedly improved functionals have been developed in the last few years [22]. A full description of these functionals and others is available in the literature [12, 16, 22].

Another option is hybrid functionals which contain elements of DFT exchange-correlation functions and Hartree-Fock theory exact exchange. These have become popular because of their ability to overcome some of the problems associated with standard DFT calculations. The most common example of a hybrid functional is the B3LYP functional [23-24] which comprises a number of functionals and parameters that are chosen to give a good fit to experimental data. B3LYP takes the form,

$$E_{\mathrm{xc}}^{\mathrm{B3LYP}} = E_{\mathrm{xc}}^{\mathrm{LDA}} + a_0 (E_{\mathrm{x}}^{\mathrm{EXX}} - E_{\mathrm{x}}^{\mathrm{LDA}}) + a_x E_{\mathrm{x}}^{\mathrm{Becke}} + a_c E_{\mathrm{c}}^{\mathrm{LYP}} \tag{3.27}$$

where E_{xc}^{LDA} is the exchange-correlation functional taken from LSDA/LDA, E_x^{EXX} is the exact exchange from Hartree-Fock, E_x^{LDA} is the exchange functional taken from LSDA/LDA, E_x^{Becke} is the Becke exchange functional [25], E_c^{LYP} is the correlation from from Lee, Yang and Parr [26] and a_0, a_x and a_c are the fitted parameters.

Results from calculations using hybrid functionals show improved agreement with experiment in areas including binding energies and geometries when compared to LDA or GGA. However, the calculation of the Hartree-Fock exact exchange is computationally expensive which somewhat limits the size of system that can be simulated using these functionals.

3.4 DFT Calculations on Solid State Systems

In addition to the fundamentals of QM/DFT calculations and the important points to consider that we have discussed, there are other crucial methods that must also be applied when simulating periodic solid systems. The main problem in simulating a solid state system arises from the fact that it is clearly impossible to assign a wavefunction for every electron in the system and also that the wavefunction of each electron extends over the entire system which is also, therefore, computationally intractable.

3.4.1 Bloch's Theorem

Bloch's theorem allows us to reduce the effectively infinite number of one electron wavefunctions in the system to simply the number in the unit cell of the system. This is done by splitting the wavefunction into a lattice periodic part and a wavelike part. The theorem states that an electronic wavefunction within a perfectly periodic potential can be expressed as,

$$\Psi_k(r) = e^{ik\cdot r}u_k(r) \tag{3.28}$$

where $u_k(r)$ is a function with the same periodicity of the potential, $u_k(r + l) = u_k(r)$, where l is the unit cell length. The other terms in equation (3.28) are i which is the band index and k which is the Bloch vector which is confined to the first Brillouin zone. The $u_k(r)$ function can be expressed with a plane wave basis set (see section 3.4.2) using the reciprocal lattice vectors, G, of the crystal,

$$u_k(r) = \sum_{\mathrm{G}} c_{j,\mathrm{G}} e^{i\mathrm{G}\cdot r} \tag{3.29}$$

where $c_{j,G}$ are the plane wave expansion coefficients. This allows the wavefunctions to be expanded using plane waves, where the wave vectors are the reciprocal lattice vectors,

$$\Psi_k(r) = \sum_{\mathrm{G}} c_{j,k+\mathrm{G}} e^{i(k+\mathrm{G})\cdot r} \tag{3.30}$$

This reduces the infinite number of one-electron wavefunctions to a tractable number of just the electrons in the unit cell. However, another problem arises from the fact that there are an infinite number of k-points in the reciprocal cell. Fortunately, all of the k-points are not needed for an accurate calculation as wavefunctions are almost identical at k-points in close proximity. Therefore, any given k-point can be used to represent a small region of the reciprocal cell. This means the calculation can be completed using a finite number of k-points. This does, however, mean that the accuracy of the calculation is very much dependent on the density of k-points used as illustrated by figure 3.2.

There are multiple methods used to sample and determine k-points. Perhaps the most commonly used is the Monkhorst-Pack scheme [27] where k-points are evenly distributed over the irreducible part of the Brillouin zone. However, the Monkhorst-Pack scheme is generally not used for hexagonal lattices as it has slow convergence and in some cases the hexagonal symmetry can be lost. This is a consequence of the Monkhorst-Pack grid shifting the k-points by half their spacing. Although this is simple for a cubic cell as each grid point and the centre point has a fold four-axis passing through it, this is not the case for a hexagonal cell. Therefore when the grid is shifted in the hexagonal cell, additional unwanted k-points are generated which are not in the

original mesh. We have used a Gamma-point centered grid for all the DFT calculations in this work.

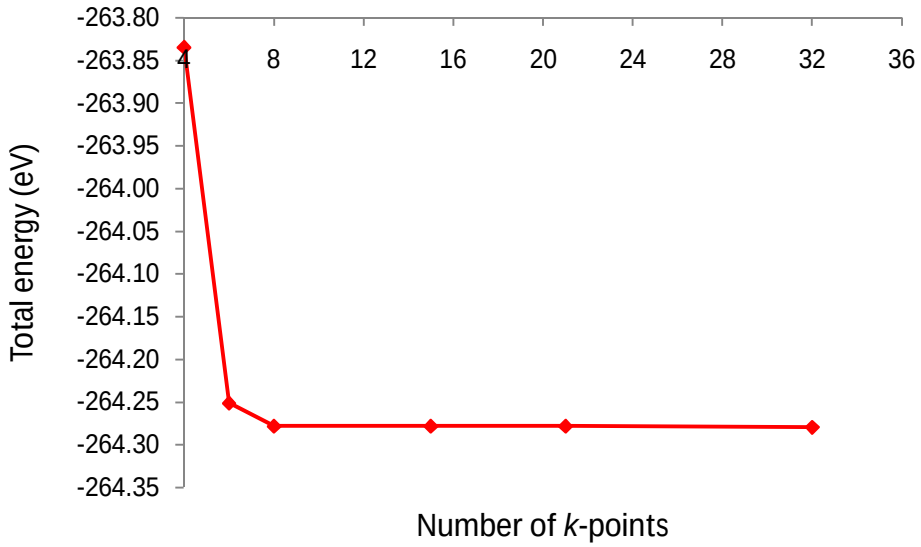

Figure 3.2: Illustration of *k*-point convergence for a total energy calculation on a hexagonal $BaTiO_3$ unit cell.

3.4.2 Basis Sets

As we have seen from Bloch's theorem, the wavefunctions can be expressed as a basis set of plane waves (PW) (equation (3.30)). Plane waves take the following form,

$$\chi(r,\theta,\phi) = N\exp[i(k_x r\sin\theta\cos\phi + k_y r\sin\theta\sin\phi + k_z r\cos\theta)] \qquad (3.31)$$

where N is a normalisation constant and k_x, k_y and k_z are quantum numbers that determine the momenta of the orbital along each of the Cartesian axes, *x*, *y* and *z*. In order to completely describe a wavefunction an infinite number of plane waves is required. However, it can still be accurately described using a finite number of plane waves as only the plane waves with a small kinetic energy will determine the wavefunction. This can be ensured by applying a cut-off energy E_{cut},

$$E_{\text{cut}} \leq \frac{\hbar^2 \left|k+G\right|^2}{2m_e} \tag{3.32}$$

It is important to select a reasonable value for E_{cut} as it determines the accuracy of the calculation and a value too small may produce results that have not fully converged. Therefore, as E_{cut} approaches infinity, the basis set approaches completeness which allows us to assess the level of the convergence for any results and identify an appropriate cut-off value. This is one of a number of advantages that PW basis sets have over types of basis sets such as localised basis sets such as Gaussian-type orbitals. Other advantages of PW basis sets include the flexibility to describe any solution and the fact that no assumption is made on the shape of the orbital. These basis sets are also computationally efficient as they can be solved easily and Fast Fourier Transform algorithms can be used for an iterative solution for eigenvalues.

Gaussian-type orbitals also provide another method for approximating the atomic orbitals. This approach is usually taken when simulating atoms and molecules as the use of a localised basis set is more appropriate here than when compared to a solid state system. A Cartesian 'primitive' Gaussian takes the general form,

$$g_i(r) = N \exp(-\alpha_j r^2) x^l y^m z^n \tag{3.33}$$

where α_j is the extraction exponent and l, m and n are integral exponents of the Cartesian coordinates and define the type of Gaussian. However, the Gaussian primitives do not exactly replicate the shape of the atomic orbitals. Therefore, we use a linear combination approach to produce the 'contracted' Gaussian-type basis functions to model the orbitals,

$$\chi_y = \sum_{j=1}^{L} d_j g_j(r) \tag{3.34}$$

where $g_j(r)$ represents the primitive Gaussians, L is the length of the contraction and d_j represents the contraction coefficients. The contracted Gaussian-type basis functions are capable of producing a far more accurate representation of the atomic orbitals.

The major advantage of this type of basis function is that a far fewer number of basis function per atom is required to accurately produce the atomic orbitals when compared to the amount needed for PW basis sets. However, they do have the disadvantage of being poor when calculating the density near and far away from the nucleus. This is illustrated by figure 3.3 which compares the form of Gaussian-type orbitals with Slater-type orbitals which are also usually used for simulating molecules.

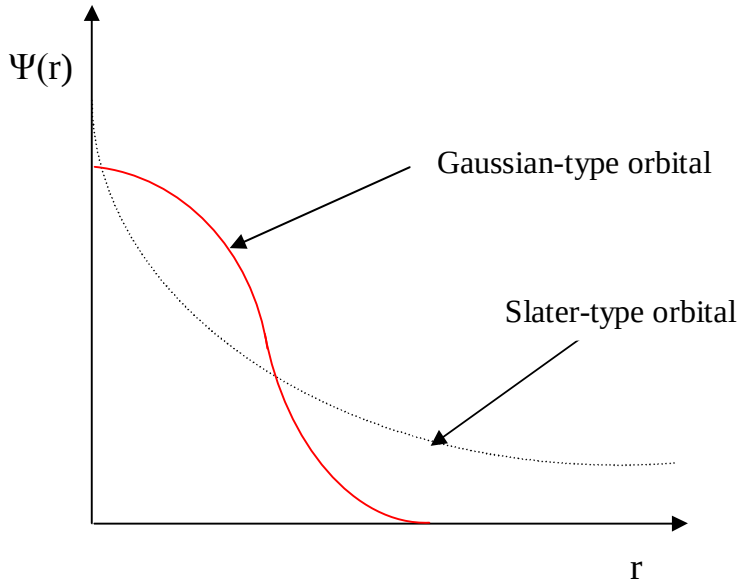

Figure 3.3: A representation of the performances of two types of basis sets with increasing distance from the nuclei.

3.4.3 Pseudopotentials

The previous sections of this discussion have shown how we have reduced the calculation of an infinitely sized system with an infinite number of wavelengths to a manageable unit cell with a finite number of *k*-points each with a finite number of plane waves. While this is now a solvable problem, it is still very computationally expensive when considering systems with hundreds of atoms. Furthermore, the wavefunctions of valence electrons oscillate rapidly near the nucleus to maintain orthogonality between the core and valence electrons. This requires a high number of plane waves to model

which also increases the computational expense. Fortunately, chemical properties and interactions are generally controlled by the valence electrons as the core electrons are tightly bound by the nuclear charge and are therefore less perturbed than the valence electrons. This allows us to separate the valence and core electrons and treat the core electrons with the pseudopotential approximation effectively.

The pseudopotential approximation replaces the nucleus and core electrons with a pseudopotential. The valence electrons are represented by pseudo-wavefunctions which interact with the pseudopotential, but without the same complex oscillations that arise from orthogonalisation of the valence electron wavefunctions to the core when the core electrons are treated explicitly (see figure 3.4). By replacing the core electron wavefunctions with node-less wavefunctions while still maintaining the same scattering, far fewer plane waves are required and the efficiency of the calculation is greatly improved. A cutoff, r_c, is used to separate the core and valence region and is dependent on the size of the core radius of the atom. The advantage of the pseudopotential method is that although the properties of the core electrons are now approximated, the pseudo-wavefunctions of the valence electrons are identical and therefore the interactions can be reliably reproduced.

There are two general types of pseudopotential, norm-conserving (NCPP) and ultrasoft (USPP). NCPPs are normalised and are based on a potential chosen capable of producing the valence properties from an all-electron calculation. It is essential that the real and pseudo-wavefunctions produce the same charge densities so that the exchange-correlation energy can be accurately obtained. NCPPs do this by ensuring that the real and pseudo-wavefunctions are equal within the core region and therefore equal outside the core region. USPPs relax the norm-conservation to produce smoother pseudo-wavefunctions which require fewer plane-waves but still maintain the accuracy of NCPPs. More information on the types of pseudopotentials can be found in [12, 16].

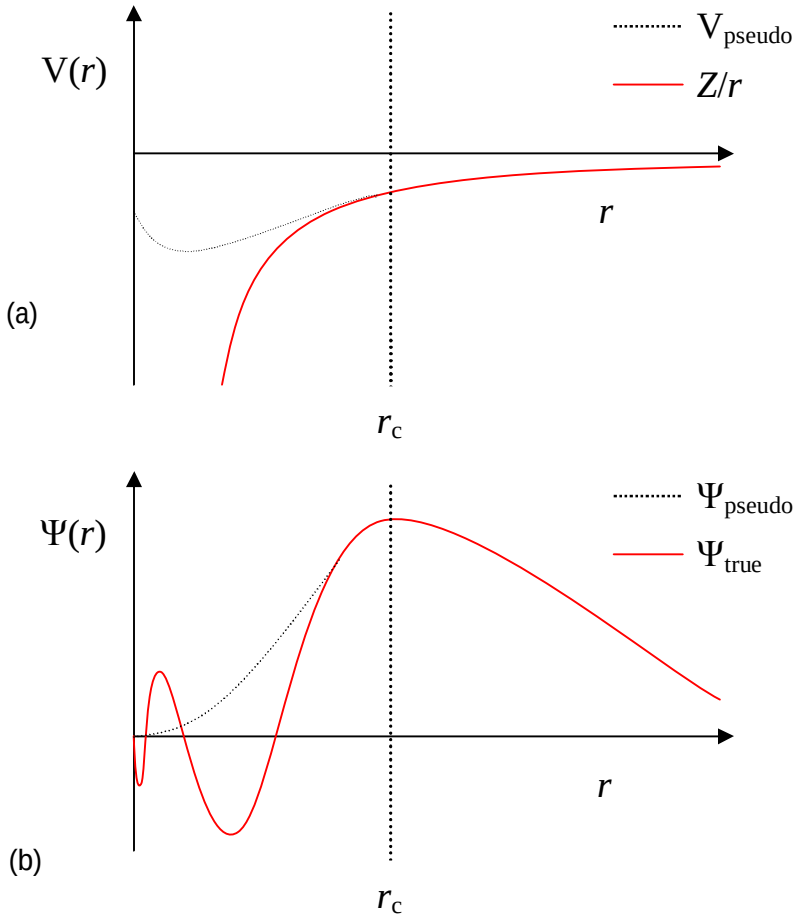

Figure 3.4: A graphical representation of the pseudopotential approximation. (a) The pseudopotential, V_{pseudo} and the true potential, Z/r. (b) The true wavefunction, Ψ_{true} and pseudo wavefunction, Ψ_{pseudo} for a 4s orbital in a Ca atom.

It is noteworthy to add that comparisons of total energy between pseudopotential and all-electron calculations are invalid because of the neglected core electrons in the pseudopotential approach. However, the total energy differences obtained from the two methods are generally meaningful and can be used for comparison.

3.4.4 Projector Augmented Waves (PAWs)

While the pseudopotential method provides a computationally efficient way of approximating the wavefunction, it can never be used to calculate the exact true wavefunction. The PAW method was developed by Blöchl [28] in 1994 and it provides an approach for calculating the all-electron wavefunction while still retaining computational efficiency. This method uses a linear transformation term, T, to transform the smooth pseudo-wavefunction,$|\Psi\rangle$, into the true wavefunction, $|\tilde{\Psi}\rangle$,

$$\left|\Psi\right\rangle = T\left|\tilde{\Psi}\right\rangle \tag{3.35}$$

This transformation term must have a form where the pseudo- and true wavefunctions only differ in the core region and before the specified cutoff so that they remain identical for the valence region,

$$T = 1 + \sum_R T_R \tag{3.36}$$

where R is the position of the atoms and T_R is an operator that acts only within spheres centred on the nucleus that are within the cutoff distance around each atom**.** This is known as the augmentation region and must be defined with an appropriate cutoff distance so that these regions do not overlap.

Inside these spherical regions, the pseudo-wavefunction can be expanded in terms of partial waves which are in turn defined by a corresponding smooth auxiliary partial wave. Similar to the pseudo-wavefunctions, the partial waves must also remain identical outside of the augmentation regions. The expansion within each sphere can be written as,

$$\left|\tilde{\Psi}\right\rangle = \sum_i \left|\tilde{\Phi}_i\right\rangle c_i \tag{3.37}$$

where $\tilde{\Phi}_i$ represents the pseudo-partial waves and c_i are unknown expansion coefficients. As a result of T being linear, the expansion coefficients can be given by projector functions, $\tilde{p}$,

$$c_i = \left\langle \tilde{p}_i \middle| \tilde{\Psi} \right\rangle \tag{3.38}$$

The projector functions must also satisfy the biorthogonality condition,

$$\sum_i \left| \tilde{\Phi}_i \right\rangle \left\langle \tilde{p}_i \right| = 1 \tag{3.39}$$

From this relation and given that T_R is effectively zero outside of the augmentation regions; we can produce a full expression for the transformation operator

$$T = 1 + \sum_i \left(\left| \Phi_i \right\rangle - \left| \tilde{\Phi}_i \right\rangle \right) \left\langle \tilde{p}_i \right| \tag{3.40}$$

and for the all electron Kohn-Sham wavefunction by using the transformation operator

$$\left| \Psi \right\rangle = \left| \tilde{\Psi} \right\rangle - \sum_i \left| \tilde{\Phi}_i \right\rangle \left\langle \tilde{p}_i \middle| \tilde{\Psi} \right\rangle + \sum_i \left| \Phi_i \right\rangle \left\langle \tilde{p}_i \middle| \tilde{\Psi} \right\rangle \tag{3.41}$$

where Φ_i represents the all-electron partial waves.

The PAW method is therefore divided into three components which define the transformation function; the all-electron partial waves, the pseudo-partial waves and the projector functions. This allows for the direct calculation of the wavefunction (unlike for regular pseudopotential methods) and therefore any physical properties. Also, because the properties of the core electrons are still approximated and the valence electron properties are treated with smooth node-less pseudo wave-functions, there is no additional computational cost when compared to NCPP and USP methods.

3.5 Conclusions

We have given a brief introduction into the theory behind QM simulations on solid state systems. We have provided a description of DFT and the fundamental theories and methods it is based on. From these theories we have seen how it is possible to apply a series of approximations to reduce the impossible calculation of an effectively infinitely sized system with an infinite number of electrons to a fully tractable calculation that can be completed with relative computational ease.

References

[1] G. Kresse and D. Joubert, Computational Materials Science **6**, 15 (1996).

[2] R. G. Parr and Y. Weitao, *Density Functional Theory of Atoms and Molecules* (Oxford Univeristy Press USA, New York, 1995).

[3] W. Koch and M. C. Holthousen, *A Chemist's guide to Density Functional Theory* (Wiley VCH, New York, 2000).

[4] M. Born and R. Oppenheimer, Annalen der Physik **389**, 457 (1927).

[5] V. Fock, Zeitschrift für Physik A **61**, 126 (1930).

[6] V. Fock, Zeitschrift für Physik A **62**, 795 (1930).

[7] J. Slater, Physical Review **35**, 210 (1930).

[8] P. Hohenberg and W. Kohn, Physical Review B **136**, 864 (1964).

[9] N. Mermin, Physical Review A **137**, 1441 (1965).

[10] W. Ritz, Journal für die Reine und Angewandte Mathematik **135**, 1 (1908).

[11] W. Kohn and L. Sham, Physical Review A **140**, 1133 (1965).

[12] J. Kohanoff, *Electronic Structure Calculations for Solids and Molecules: Theory and Computational Methods* (Cambridge University Press, New York, 2006).

[13] D. M. Ceperley and B. J. Alder, Physics Review Letters **45**, 566 (1980).

[14] J. P Perdew and A. Zunger, Physical Review B **23**, 5048 (1981).

[15] W. Kohn and L. Sham, Physical Review A **140**, 1133 (1965).

[16] R. M. Martin, *Electronic Structure: Basic theory and Practical Methods* (Cambridge Univeristy Press, Cambridge, 2004).

[17] J. P Perdew, International Journal of Quantum Chemistry **28**, 497 (1985).

[18] M. K. Y. Chan and G. Ceder, Physical Review Letters **105**, 196403 (2010).

[19] M. J. Lucero, T. M. Henderson and G. E. Scuseria, Journal of Physics: Condensed Matter **24**, 145504 (2012).

[20] J. P. Perdew and Y. Wang, Physical Review B **45**, 13244 (1992).

[21] J. P. Perdew, K. Burke and M. Ernzerhof, Physical Review Letters **77**, 3865 (1996).

[22] P. Haas, F. Tran, P. Blaha, K. Schwarz and R. Laskowski, Physical Review B **80**, 195109 (2009).

[23] S. H. Vosko, L. Wilk, and M. Nusair, Canadian Journal of Physics **58**, 1200 (1980).

[24] P. J. Stephens, F. J. Devlin, and C. F. Chabalowski, Journal of Physical Chemistry **98**, 11623 (1994).

[25] A. D. Becke, Journal of Chemical Physics **98**, 5648 (1993).

[26] C. Lee, W. Yang, and R. G. Parr, Physical Review B **37**, 785 (1988).

[27] H. J. Monkhorst and J. D. Pack, Physical Review B **13**, 5188 (1976).

[28] P. E. Blöchl, Physical Review B **41**, 5414 (1990).

4

Rare-earth and Transition Metal Doping of $BaTiO_3$

4.1 Introduction

The perovskite structure can accommodate a wide range of both isovalent and aliovalent dopant ions. The work in this section focuses on aliovalent doping using rare earth (RE) and transition metal ions. Aliovalent doping can be sub-divided into donor or acceptor doping. The former is the doping of an ion with a higher valence state than the host ion, whereas the latter is the doping of an ion with a lower valence state than the host ion. Both types of aliovalent doping have noticeable effects on the electrical properties of $BaTiO_3$; however the effects of donor doping in particular can cause dramatic changes in the dielectric and conducting properties of the material [1-2] as well as the ferroelectric Curie temperature, T_c [3-4]. This is true even at low concentrations, as shown by the example of the large rare earth La^{3+} ion that donor dopes at the Ba-site [3] and causes a significant decrease in resistivity of $BaTiO_3$ [2].

The doping of La at the Ba-site in $BaTiO_3$ can produce a significant increase in electrical conductivity when the samples are processed in air or reducing atmospheres [5]. Conversely, sample preparation in flowing O_2 can also cause the samples to become insulating [5]. It has been reported that A-site La^{3+} doping of *h*-$BaTiO_3$ occurs by an electronic compensation mechanism [6] which permits a giant permittivity effect to be obtained without the need to induce or control the oxygen deficiency [6] in the material. Whether the charge compensation mechanism for this type of doping is electronic or ionic has been a controversial topic for many years.

Smaller RE cations such as Yb and Lu [7-8] and transition metal ions [9-12] generally act as acceptor dopants and substitute at the smaller Ti-site. It is agreed that

charge compensation for these dopants comes from oxygen vacancies. The main application for these doped materials is Ni-based MLCCs [13], although the presence of oxygen vacancies causes degradation of the capacitors. B-site transition metal doping can also cause a decrease in the cubic-hexagonal polymorphic phase transition of $BaTiO_3$. This stabilisation has been shown to be the most significant with Mn [14-16], Co [17-18], Fe [19] and Ni [20]. Various theories have been suggested to justify this stabilisation. Langhammer *et al.* [16] provides an overview and suggests that oxygen vacancies arising from the incorporation of these dopants have an important role in lowering the phase transition temperature. This view is corroborated by Jayanthi and Kutty [17] who suggest that oxygen vacancies and the corresponding defect complexes with multivalent dopant states stabilise the hexagonal polymorph to lower temperatures. It is noteworthy, however, that this stabilisation process is still a widely debated subject and that various other explanations have been proposed [9, 21].

Mid-sized RE cations like Eu, Gd and Ho can dope at both the Ba- and Ti-sites simultaneously and is referred to as 'self-compensation' [22-23].

Numerous classical simulations exist for perovskite systems [23-25] but surprisingly the actual work on $BaTiO_3$ is somewhat limited. The vast majority of this work was completed using a potential model developed by Lewis and Catlow [26] which has been used to study a number of intrinsic and extrinsic defects in $BaTiO_3$. This potential model adequately describes the structure of the perovskite material and suggested that Ba-site donor doping with electron compensation is favoured for large RE ions, but that self-compensation with RE ions simultaneously substituting on both the Ti and Ba sites is more favourable for smaller RE ions. Further calculations using this potential model were completed by Buscaglia *et al.* [27] and the four compensation schemes most commonly reported in experiment were all tested. Similarly to Lewis and Catlow [26] it was reported that Ba-site substitution with electron compensation for La and Pr is favoured and that self-compensation was the dominant mechanism for intermediate sized RE ions like Gd and Er. The Ti vacancy compensation scheme with the RE on the Ba site was found to be energetically unfavourable for all of the RE ions. A surprising result from the calculations of Buscaglia *et al.* was that the interaction between charged

defects (i.e. the binding energy) for RE doping to be small negative or even positive values. The binding energies for transition metal doping were, however, significantly stronger especially for the interaction between a trivalent dopant (i.e. Cr, Ni, Fe and Co) and a Ti vacancy. Unfortunately only the binding energies of defect pairs and not defect clusters were considered. Hence these results do not represent the whole Coulombic stabilisation present in the system.

In the work by Buscaglia *et al.* it is stated that a combination of values from different potential models were used to calculate the substitution energy for a Ti^{3+} at a Ti^{4+} site. This produces a value a 36 eV compared to the Lewis and Catlow value of 28.98 eV. These values only represent the direct calculation of substituting a Ti^{3+} at a Ti^{4+} site and do not include contributions from the ionisation energy and electron affinity. In addition to this difference, our own calculations using the Lewis and Catlow potential model show that there is also a significant difference for the cohesive energies of BaO, - 31.31 eV (Buscaglia *et al.*) and - 34.57 eV (Lewis and Catlow). This suggests that multiple potential models have been used for this calculation also. It is, therefore, problematic to assess the results for the solution energies reported because of the inconsistency present in calculating them.

One of the very few first-principles studies of RE doping of $BaTiO_3$ was completed by Moriwake *et al.* [28]. La-doping was reported to occur on the Ba-site with the charge compensation mechanism being dependent on the nature of the atmosphere simulated. For mid-sized ions like Dy and Ho, doping was found to occur at either the Ba- or Ti-site, again depending on the atmosphere. This is somewhat contradictory to experiment where self-compensation is usually observed [22-23]. The same authors also carried out simulations on Mn-doping using DFT [29]. In this work Mn was found to be stable on the Ti-site under four different thermodynamic environments although the valence state of the ion varies in these different environments. Other DFT simulations [21] calculated Co defect formation energies in tetragonal and hexagonal $BaTiO_3$. It was observed that beyond a critical concentration of Co (between 2.7 and 5.5 at%) the defect formation energy for Co incorporation was significantly less in the hexagonal polymorph compared with the tetragonal polymorph. The computational expense of these DFT

simulations means that only small cells can be used and it is therefore difficult to obtain a full description of the system. The need for an improved potential model capable of accurately describing the defect chemistry of $BaTiO_3$ is therefore essential.

Through the use of the new potential model we look to confirm experimental findings on the doping of $BaTiO_3$ and enable prediction of site preference, charge states in the case of transition metals and the resulting charge compensation. We also use these results to assess the stabilisation of *h*-$BaTiO_3$ by transition metal doping and discover with which dopant ions and charge states this effect is strongest, if any.

4.2 Methods

4.2.1 Potential Development

The full $BaTiO_3$ potential model used in this chapter and for the majority of the work in this thesis is given in table 4.1. The values for the shell model parameters (see chapter 2) are also provided.

Buckingham Potentials			
Interaction	A (eV)	ρ (Å)	C (eV Å^{-6})
Ba^{2+} - O^{2-}	1150.0	0.3804	55.0
O^{2-} - O^{2-} [26]	22764.0	0.1490	43.0

Lennard-Jones 7-6 Potentials		
Interaction	A (eV Å^7)	B (eV Å^6)
Ti^{4+} - O^{2-}	1234.208	471.9723

Three-body Potentials			
Interaction	k_2 (eV)	θ_0 (°)	Cutoffs (Å)
O^{2-} - Ti^{4+} - O^{2-}	1.82	90	2.5 2.5 3.5

Shell Model		
Species	Shell Charge	k (eV Å^{-2})
Ba^{2+}	- 1.45	56.23
O^{2-}	- 2.47	15.41

Table 4.1: $BaTiO_3$ potential and shell model parameters.

A complete description of the development of the potential model that we have used throughout this work is given by Freeman *et al.* [30]. Unlike previous $BaTiO_3$ models,

this model uses a Lennard-Jones potential to model the Ti-O interaction. This type of potential was chosen since unlike a Buckingham potential, a Lennard-Jones potential generates a potential energy well which represents the bonding character shown to be present in the Ti-O interaction by DFT simulations [31]. A 7-6 Lennard-Jones potential was chosen as the 7 index for the repulsive element of the interaction best represents the shape of a Buckingham potential, the standard potential type for these types of calculations which generally produces good agreement with atomic separations. A three-body term O-Ti-O was also used to provide further rigidity to the TiO_6 octahedra and was fitted using unrestricted Hartree-Fock single point calculations on distorted TiO_6 clusters. In this work Ti^{4+} is treated as a non-polarisable species. All these calculations were completed by C. L. Freeman.

A Buckingham potential was used to model the Ba-O interaction as no significant covalency has been reported for this interaction. The O-O Buckingham potential was taken from the original Lewis and Catlow $BaTiO_3$ model [26] to ensure consistency between other oxide materials and defect-oxygen interactions. This oxygen potential has been used to model a range of other perovskite systems [25, 32]. Both the Ti-O and Ba-O potential parameters were fitted to give accurate values for the cohesive energies and lattice parameters of *c*-$BaTiO_3$, *h*-$BaTiO_3$ and the associated end members, TiO_2 (rutile) and BaO. A Monte Carlo (MC) algorithm was used to vary both the Buckingham and Lennard-Jones potential parameters to ensure the best fit to experimental data. In order to accurately simulate the defect chemistry of $BaTiO_3$ or indeed any ceramic material, it is essential that the Buckingham and Lennard-Jones potentials can reliably model the energetics and structures of the end members. It is also important that the model is capable of accurately calculating the energetics of these systems at different internuclear separations. The cohesive energies and lattice parameters using the new potential model are given in tables 4.2 and 4.3.

Cohesive energy of formula unit (eV)			
Crystal	Experiment	Lewis and Catlow	This Work
c-$BaTiO_3$	- 159.86	- 148.02	- 160.02
h-$BaTiO_3$	- 159.73	- 147.69	- 159.94
TiO_2	- 125.50	- 112.47	- 127.64
BaO	- 31.90	- 34.57	- 32.58

Table 4.2: Cohesive energies of *c*-$BaTiO_3$, *h*-$BaTiO_3$, TiO_2 and BaO. Experimental cohesive energies are derived using a Born-Haber cycle as described in Freeman *et al.* [30] and in figure 4.1.

		Lattice parameter (Å)	
Crystal	Parameter	Experiment [33]	This Work
c-$BaTiO_3$	a	4.00	4.01
h-$BaTiO_3$	a, c	5.74, 14.05	5.80, 14.21
TiO_2	a, c	4.59, 2.96	4.49, 3.14
BaO	a	5.52	5.33

Table 4.3: Lattice parameters of *c*-$BaTiO_3$, *h*-$BaTiO_3$, TiO_2 and BaO.

The potential model clearly describes both the energetics and lattice parameters of all the necessary crystal structures with very good accuracy. The interatomic separations are also similar to the experimental values. All RE interatomic potentials as well as the Ti^{3+}-O^{2-} potential were taken from Lewis and Catlow [26]. The transition metal potentials used here are also taken from Lewis and Catlow as well as Buscaglia *et al.* [27], with the exception of the Fe^{4+} - O^{2-} potential which is taken from Cherry *et al.* [34].

A cutoff distance of 12 Å was used for all the $BaTiO_3$ potentials and a cutoff distance of 10 Å was used for the dopant potentials.

We have used the GULP code [35] for all our defect calculations.

4.3 Rare-earth Doping of *c*-$BaTiO_3$

4.3.1 Defect Chemistry

In order to compensate for the change in charge that occurs when a trivalent ion dopes at a divalent or tetravalent ion site, a further defect must be formed to ensure charge neutrality. We consider the five major charge compensation schemes for RE^{3+} doping of $BaTiO_3$. With the exception of scheme 5 (substitution at a Ba-site with Ba vacancy compensation) all these mechanisms were also considered by Buscaglia *et al.* [27]. By the calculation of all of these terms, the solution energy (E_s) for a defect can be found.

1. Substitution of M^{3+} at Ba^{2+} with conduction electron compensation.

$$M_2O_3 + 2Ba_{Ba} \longrightarrow 2M_{Ba}^{\bullet} + \frac{1}{2}O_2 + 2e' + 2BaO \tag{4.1}$$

$$E_s = \frac{1}{2}[2E_{sub,Ba}^{M^{3+}} + 2E_{sub}^{Ti^{3+}} + 2E^{e'} - \frac{1}{2}D_{O_2} + E_A^{O^{2-}} + 2E_L^{BaO} - E_L^{M_2O_3}] \tag{4.2}$$

2. Substitution of M^{3+} at Ba^{2+} with Ti^{4+} vacancy compensation.

$$2M_2O_3 + 4Ba_{Ba} + Ti_{Ti} \longrightarrow 4M_{Ba}^{\bullet} + V_{Ti}'''' + 3BaO + BaTiO_3 \tag{4.3}$$

$$E_s = \frac{1}{4}[4E_{sub,Ba}^{M^{3+}} + E_{vac}^{Ti^{4+}} + E_L^{BaTiO_3} + 3E_L^{BaO} - 2E_L^{M_2O_3}] \tag{4.4}$$

3. Substitution of M^{3+} at Ti^{4+} with O^{2-} vacancy compensation.

$$M_2O_3 + 2Ti_{Ti} + O_O \longrightarrow 2M_{Ti}' + V_O^{\bullet\bullet} + 2TiO_2 \tag{4.5}$$

$$E_s = \frac{1}{2}[2E_{sub,Ti}^{M^{3+}} + E_{vac}^{O^{2-}} + 2E_L^{TiO_2} - E_L^{M_2O_3}] \tag{4.6}$$

4. Substitution of M^{3+} at Ba^{2+} and M^{3+} at Ti^{4+} leading to self-compensation.

$$M_2O_3 + Ba_{Ba} + Ti_{Ti} \longrightarrow M^{\bullet}_{Ba} + M'_{Ti} + BaTiO_3 \quad (4.7)$$

$$E_s = \frac{1}{2}[E^{M^{3+}}_{sub,Ba} + E^{M^{3+}}_{sub,Ti} + E_L^{BaTiO_3} - E_L^{M_2O_3}] \quad (4.8)$$

5. Substitution of M^{3+} at Ba^{2+} with Ba^{2+} vacancy compensation.

$$M_2O_3 + 3Ba_{Ba} \longrightarrow 2M^{\bullet}_{Ba} + V''_{Ba} + 3BaO \quad (4.9)$$

$$E_s = \frac{1}{2}[2E^{M^{3+}}_{sub,Ba} + E^{Ba^{2+}}_{vac} + 3E_L^{BaO} - E_L^{M_2O_3}] \quad (4.10)$$

Term	Description	Value (eV)
$E^{M^{3+}}_{sub,site}$	Substitution energy required to replace a M^{3+} ion on a regular Ba^{2+} or Ti^{4+} site	See table 4.5
$E^{Ba^{2+}}_{vac}$	Energy required to move a Ba^{2+} from its regular lattice site to infinity	19.50
$E^{Ti^{4+}}_{vac}$	Energy required to move a Ti^{4+} from its regular lattice site to infinity	98.96
$E^{O^{2-}}_{vac}$	Energy required to move a O^{2-} from its regular lattice site to infinity	24.66
$E^{Ti^{3+}}_{sub}$	Energy required to substitute a Ti^{3+} on a regular Ti^{4+} site	49.23
$E^{e'}$	Energy required (in the gas phase) for the process, $Ti^{4+} + e' \rightarrow Ti^{3+}$	- 43.24 [36]
D_{O_2}	Dissociation energy of molecular oxygen	5.16 [36]
$E_A^{O^{2-}}$	Sum of the first and second electron affinity of oxygen in trivalent oxides	See table 4.5
E_L^{BaO}	Cohesive energy of BaO	- 32.58
$E_L^{TiO_2}$	Cohesive energy of TiO_2	- 127.64
$E_L^{BaTiO_3}$	Cohesive energy of *c*-$BaTiO_3$	- 160.02
$E_L^{M_2O_3}$	Cohesive energy of M_2O_3	See table 4.5

Table 4.4: Description of terms used in the calculation of solution energies for *c*-$BaTiO_3$.

The results for the vacancy calculations are considerably different from previous results calculated by Buscaglia *et al.* [27]. The values for both oxygen and titanium vacancies have increased significantly, while the value for a barium vacancy has decreased. Such differences are to be expected, as the Ti-O potential used in this work produces a far stronger interaction than that of the previous model and hence the energy required to remove ions from this interaction is higher. Substitution energies represent the energy required to bring a defect ion into the lattice from infinity and remove the ion it is replacing to infinity. The substitution energies calculated for *c*-$BaTiO_3$ are consistent with ion-size arguments as from the large ion (La) to the smaller ion (Lu), the substitution becomes more favourable as the charge density is increasing (i.e. the ion size is getting smaller).

Rare Earth	$E_{sub,Ba}^{M^{3+}}$(eV)	$E_{sub,Ti}^{M^{3+}}$ (eV)	Cohesive energy, $E_L^{M_2O_3}$ (eV)	Sum of first and second oxygen electron affinity, $E_A^{O^{2-}}$ (eV)
La	- 22.37	58.46	- 126.16	7.53
Nd	- 23.70	55.93	- 129.28	6.76
Eu	- 24.63	54.17	- 132.46	6.18
Gd	- 24.83	53.72	- 133.07	7.23
Ho	- 25.79	51.90	- 135.80	7.01
Yb	- 26.37	50.62	- 137.79	6.90
Lu	- 26.66	50.14	- 138.62	7.81

Table 4.5: Substitution energies, cohesive energies and the sum of the first and second oxygen electron affinities for RE dopants and their respective oxide.

For charge compensation scheme 1, the sum of the first and second electron affinities of oxygen must be determined. However, unlike the first electron affinity of oxygen which is well known and has been determined by experiment, the second

electron affinity of oxygen is dependent upon the crystal structure and therefore must be calculated for each M_2O_3. This calculation can be completed using a Born-Haber cycle as illustrated in figure 4.1. A description of the Born-Haber cycle method is available elsewhere [37]. Values used in this cycle were taken from the literature [36, 38-39] with the exception of the cohesive energies which were calculated using potentials.

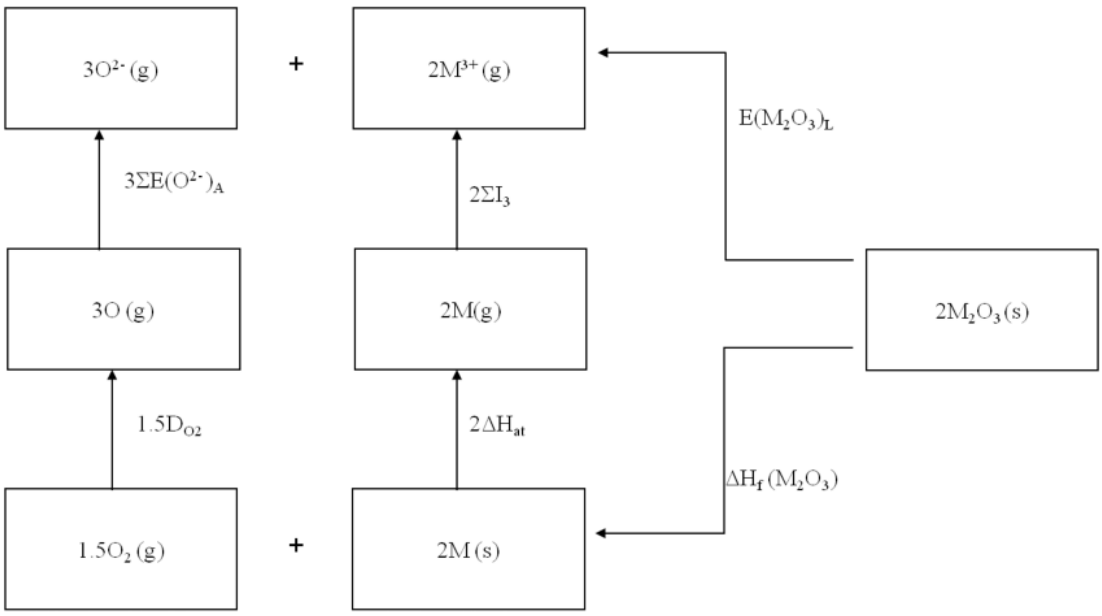

Figure 4.1: Born-Haber cycle for the formation on M_2O_3. ΔH_f (M_2O_3) is the enthalpy of formation of M_2O_3, ΔH_{at} is the enthalpy of atomisation for the rare-earth ions, ΣI_3 is the sum of the first, second and third ionisation energy of the rare-earth ions. Other terms are defined in table 4.4.

4.3.2 Solution Energies for *c*-$BaTiO_3$

The energy of solution (E_s) for each dopant species and for each charge compensation scheme calculated using the relevant cohesive energies, substitution energies and vacancy energies is given in table 4.6. The fraction present in each charge compensation scheme ensures the solution energy is calculated per dopant ion.

		Solution Energy, E_s (eV)				
Rare Earth	Ionic Radii (Å)	RE_{Ba} + e'	RE_{Ba} + V_{Ti}	RE_{Ti} + V_O	RE_{Ba}+ RE_{Ti}	RE_{Ba} + V_{Ba}
La	1.032	9.06	1.01	6.23	1.11	1.59
Nd	0.983	9.68	1.24	5.26	0.74	1.82
Eu	0.947	10.63	1.90	5.09	0.99	2.48
Gd	0.938	10.21	2.00	4.94	0.97	2.58
Ho	0.901	10.72	2.41	4.49	0.94	2.99
Yb	0.868	11.20	2.82	4.21	1.01	3.41
Lu	0.861	10.87	2.95	4.14	1.04	3.53

Table 4.6: Solution energies for the different schemes in *c*-$BaTiO_3$.

The initial solution energies suggest that self-compensation is the favoured compensation mechanism for all RE ions excluding La incorporation for which is the favoured compensation by Ti vacancies. It is noteworthy that the energy difference between these two mechanisms is within 1 eV for a number of RE ions and therefore that either mechanism is possible. While these mechanisms are reasonable for large and mid-sized ions [5, 22-23], they are certainly not correct for small sized ions as it has been confirmed experimentally that they dope at the Ti-site exclusively [7-8]. The reason for this contrast is the fact that solution energies only consider isolated defects and in a real solid state system, the dopant and oppositely charged compensating defect interact. The binding energies for these configurations must be therefore calculated. In rare cases, strain effects can dominate the electrostatic interaction between these defects.

4.3.3 Binding Energies for *c*-$BaTiO_3$

Binding energies for each scheme have been calculated and the results for the lowest energy clusters are given in table 4.7. In comparison with the weak or nonexistent binding energies calculated by Buscaglia *et al.*, our binding energies are all negative and in some cases very strong depending on the charges of the defects in the cluster. The lowest energy clusters for schemes 2 (RE_{Ba} + V_{Ti}) and 3 (RE_{Ti} + V_O) are shown in figure 4.2.

		Binding Energy (eV)				
Scheme		1	2	3	4	5
Rare Earth	Ionic Radii (Å)	RE_{Ba} + e'	RE_{Ba} + V_{Ti}	RE_{Ti} + V_O	RE_{Ba}+ RE_{Ti}	RE_{Ba} + V_{Ba}
La	1.032	- 0.15	- 0.24	- 8.34	- 0.14	- 0.48
Nd	0.983	- 0.10	- 0.24	- 7.71	- 0.14	- 0.44
Eu	0.947	- 0.06	- 0.43	- 7.34	- 0.12	- 0.40
Gd	0.938	- 0.07	- 0.57	- 7.25	- 0.13	- 0.40
Ho	0.901	- 0.07	- 1.09	- 6.91	- 0.14	- 0.40
Yb	0.868	- 0.11	- 1.75	- 6.73	- 0.19	- 0.46
Lu	0.861	- 0.12	- 1.93	- 6.66	- 0.22	- 0.48

Table 4.7: Binding energies for the different schemes in *c*-$BaTiO_3$.

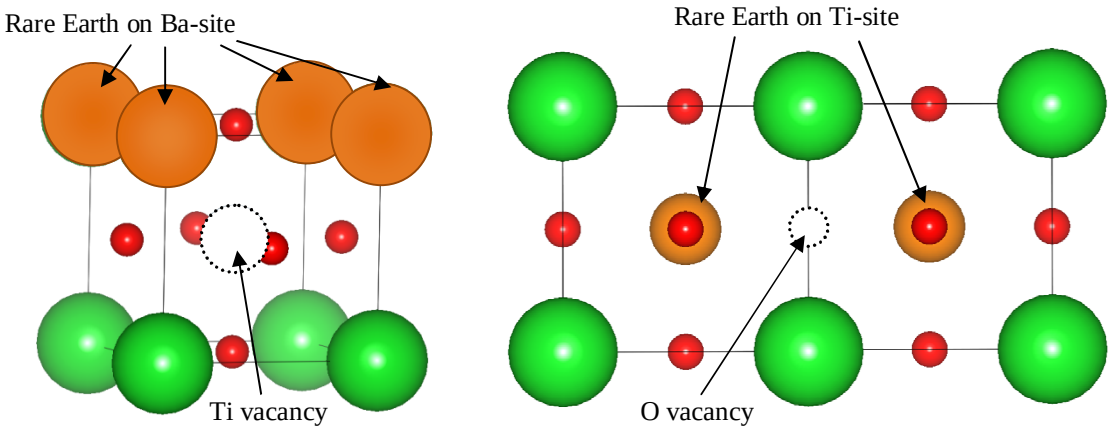

Figure 4.2: Lowest binding energy clusters for schemes 2 (left) and 3 (right).

The binding energies produced by scheme 1 (electron compensation) are small negative values. This is as a result of the relatively weak interaction between the +1 charged RE site and the -1 charged Ti-site produced from the addition of an electron to the original Ti^{4+} ion. There is no strong trend in binding energies for the defects in this scheme.

For scheme 2 ($RE_{Ba} + V_{Ti}$) the binding energies become more negative in energy as the RE ion decreases in size. As the RE ion size decreases, its charge density increases which creates a stronger Coulombic interaction between the RE_{Ba}^{1+} sites and the negatively charged Ti^{4-} vacancy. Also, the introduction of RE_{Ba} creates stronger RE–O interactions compared to the Ba–O interactions due to the greater charge on the RE ion. Furthermore, the V_{Ti}^{4-} results in the adjoining O anions being pulled closer to the other neighbouring cations resulting in even greater RE-O interactions. This effect becomes stronger with decreasing RE ion size as the strength of the RE-O interaction increases. These effects all cause the binding energy to become more negative with decreasing ion size.

Scheme 3 ($RE_{Ti} + V_O$) produces the most substantial binding energies by far which decrease in magnitude with decreasing RE ion size (the opposite trend to what was observed for scheme 2). The strong binding energy results from the large positive O vacancy that can couple strongly to both the RE sites due to the close binding network formed by the TiO_6 octahedra. The trend of decreasing binding energy with decreasing RE ion size is because of the weaker RE-O interactions produced by substitution of the Ti with a RE cation compared to the original Ti-O interaction. This RE-O interaction is weakest with the larger RE ions and hence when a V_O is introduced to the system, the loss of a RE-O interaction has less of an energetic effect than the loss of a Ti-O interaction or a RE-O interaction where the rare-earth is smaller and the interaction is stronger. Therefore, the system prefers to maintain the stronger RE-O or Ti-O interaction to avoid a larger energetic penalty, whereas the penalty is not as large for a weaker RE-O interaction from a larger RE ion.

The self-compensation scheme has small binding energies as the charged defect sites created are singly charged unlike some other schemes and there is only a defect pair binding as opposed to a defect cluster. Generally, binding energy becomes stronger with decreasing ion size, although the binding energy does deviate slightly from this trend for the similarly sized Eu and Gd ions. Similar, to scheme 2, an energy gain is achieved from the stronger RE-O interactions formed (compared to the Ba-O interactions), this is especially true for small RE ions. However, this effect is reduced because of the loss of the stronger Ti-O interaction caused by the introduction of RE_{Ti}.

For the final scheme which binds two RE_{Ba} to a V_{Ba}, relatively weak binding energies are observed, although stronger than the previous scheme as now three defects are binding and the V_{Ba} is doubly charged. The binding energies do not follow a clear trend but generally all fluctuate around approximately the same value. It is likely that large separation between the A-sites in comparison to other schemes where defects are closer is the reason why no trend is observed with RE ion size.

4.3.4 Binding Modified Solution Energies for *c*-$BaTiO_3$

By combining the previously calculated solution energies with the binding energies, a true representation of the energetics involved in dopant incorporation can be established. The amount of binding energy added to the solution energy depends upon the number of rare-earth ions doping in each scheme and is equivalent to the fraction used within each scheme (equations (4.1) – (4.10)), with the exception of scheme 1 where the full binding energy is used as each RE ion can bind with one Ti^{3+} ion. The modified solution energies are shown in table 4.8 and plotted in figure 4.3. Additionally, all schemes excluding scheme 1 are plotted in figure 4.4.

		Binding Modified Solution Energy, E_s (eV)				
Rare Earth	Ionic Radii (Å)	RE_{Ba} + e'	$RE_{Ba} + V_{Ti}$	$RE_{Ti} + V_O$	RE_{Ba}+ RE_{Ti}	$RE_{Ba} + V_{Ba}$
La	1.032	8.91	0.95	2.06	1.04	1.35
Nd	0.983	9.58	1.18	1.40	0.67	1.60
Eu	0.947	10.57	1.79	1.42	0.93	2.28
Gd	0.938	10.14	1.86	1.32	0.90	2.38
Ho	0.901	10.65	2.14	1.03	0.87	2.79
Yb	0.868	11.09	2.39	0.84	0.91	3.18
Lu	0.861	10.75	2.47	0.81	0.93	3.29

Table 4.8: Binding modified solution energies for the different schemes in *c*-$BaTiO_3$.

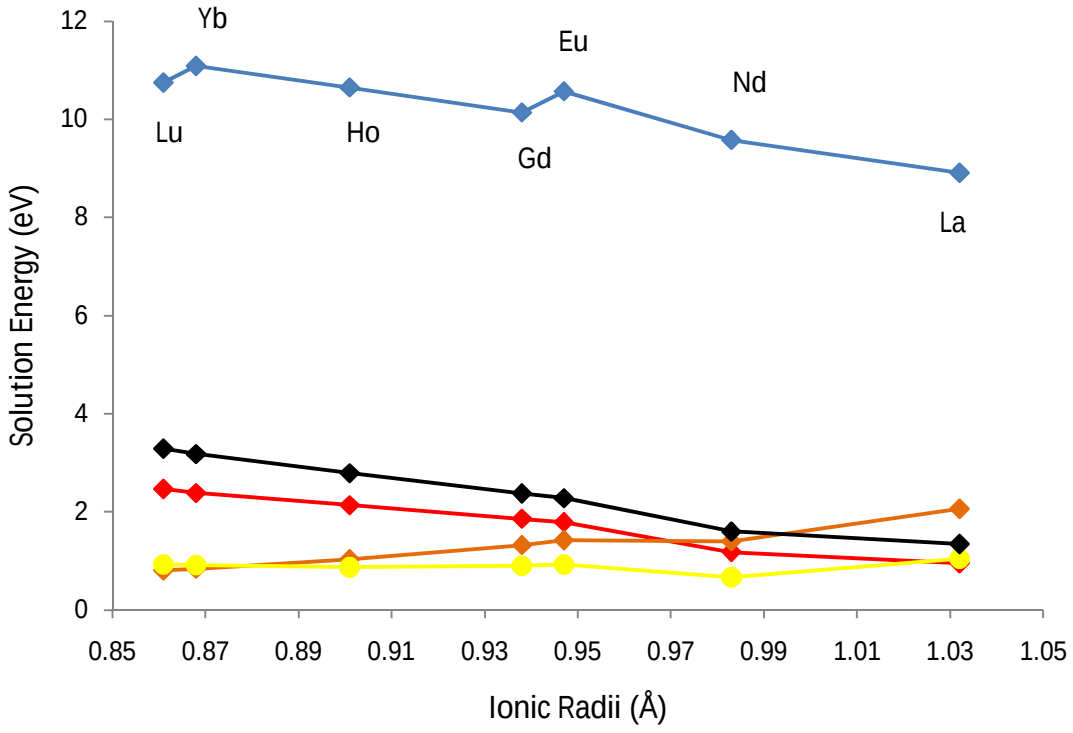

Figure 4.3: Solution energies for the five charge compensation schemes modified by the addition of the defect binding energies. Code: Blue – Scheme 1 (RE_{Ba} + e^-); Red – Scheme 2 (RE_{Ba} + V_{Ti}); Orange – Scheme 3 (RE_{Ti} + V_O); Yellow – Scheme 4 (RE_{Ba} + RE_{Ti}); Black – Scheme 5 (RE_{Ba} + V_{Ba}).

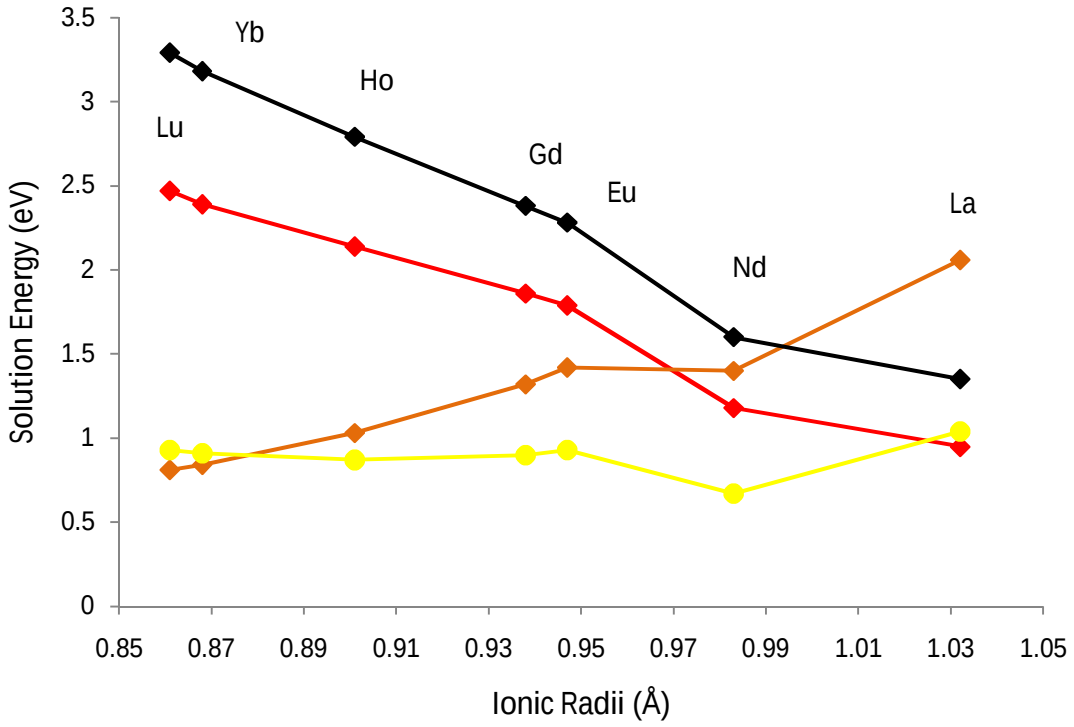

Figure 4.4: Solution energies for the four lowest energy charge compensation schemes modified by the addition of the defect binding energies. Code: Red – Scheme 2 (RE_{Ba} + V_{Ti}); Orange – Scheme 3 (RE_{Ti} + V_O); Yellow – Scheme 4 (RE_{Ba} + RE_{Ti}); Black – Scheme 5 (RE_{Ba} + V_{Ba}).

The electron compensation scheme is clearly significantly higher in energy compared to the four alternative mechanisms. There is a difference of at least 6 eV between these mechanism and the next most favourable mechanisms for any particular RE ion. It is noteworthy to add that such an energy difference cannot be bridged by any small error in the values of the second electron affinities of oxygen. Experimentally this mechanism is believed to be the mechanism of incorporation for La and the explanation for the conducting properties of this doped material. However, as previously explained this topic has led to significant controversy [5, 40]. The implications for this result are discussed in the following section. The small variations in this scheme with respect to

ion size are as a result of the variation in oxygen electron affinities caused by subtle differences between the M_2O_3 lattices.

As expected, smaller RE ions preferentially dope at the Ti-site, whereas larger ions prefer the Ba-site. Although the substitution energies for both Ba- and Ti-site substitution decrease with decreasing RE ion size, this does not outweigh the larger increase in stability of the M_2O_3 environment and hence larger cohesive energy for smaller RE ions. Therefore, generally as the RE cation size decreases, the solution energies increase with the exception of scheme 3 (because of the energy gain from two RE_{Ti} defects) and scheme 4 (which generally remains constant with RE ion size). For all schemes the Nd ion is lower than expected, this is especially noticeable for schemes 3 and 4. This is due to the lower than expected cohesive energy of Nd_2O_3 based on its ion size. This is a feature of the Nd-O potential fitted by Catlow and Lewis.

Our results show excellent agreement with experimental findings and improve on the theoretical/experimental agreement observed in the calculations of Buscaglia *et al.* and Lewis and Catlow. Our results suggest that large RE ions such as La dope preferentially at the Ba-site with charge compensation by Ti vacancies. This is confirmed by experiment [3, 5, 41]. However as discussed there is controversy over whether electrons or cation vacancies are responsible for the compensation. DFT calculations also confirm substitution on the Ba-site [28] in all thermodynamic environments excluding the Ti-TiO_2 rich environment, where both A- and B-site substitution are possible. It was found that in oxidising conditions charge compensation from Ti vacancies is favoured and in reducing conditions electron compensation is favoured. Again it should be noted that although scheme 2 is the lowest in energy for La, there are two other competing schemes within 1 eV.

Experimental agreement is also found for mid-sized ions, namely Gd^{3+}, Eu^{3+} and Ho^{3+}. In both our calculations and in experiment, self-compensation dominates for these ions [22-23]. In experiments the doping site of the RE is also dependent upon other factors such as the sintering atmosphere and Ba/Ti ratio. For example control of the Ba/Ti ratio gives control of the doping site for Gd [23]. DFT calculations [28] did not consider the possibility of self-compensation but did predict that Ho is capable of

doping at both the A- and B-sites of $BaTiO_3$. Classical calculations with the previous $BaTiO_3$ potential model also predicted self-compensation for mid-sized ions [27].

Our simulations show that small RE ions (Yb^{3+} and Lu^{3+}) are energetically favoured to dope at the Ti-site with oxygen vacancy charge compensation. This is confirmed by X-ray diffraction and electron paramagnetic resonance experiments [8, 42]. Simulations by Buscaglia *et al.* showed that self-compensation was preferred as the incorporation mechanism for small ions, contrary to experiment. The self-compensation mechanism is also low in energy for small RE ions in our calculations also.

One important difference between the simulations in this work and experiment is the concentration of the RE defects. In this methodology defects are at infinite dilution, whereas in experiment the dopant concentration is finite (usually between 1 and 20 mol%). Therefore for even greater comparison with experiment these defects should be simulated as solid solutions. This is a possible future topic to address.

4.3.5 Implications for Conduction of La-doped *c*-$BaTiO_3$

Donor-doping $BaTiO_3$ with La causes a significant alteration in the conduction properties of the material [3]. It is generally agreed that this conduction must either come from electron compensation or from oxygen vacancies present in the sample. At the infinitely dilute limit, our simulations clearly suggest this must be a result of oxygen vacancies, as the mechanisms for electron compensation is considerably higher than any other possible mechanisms considered. For the previous classical calculations carried out by Lewis and Catlow and Buscaglia *et al.*, La-doping occurred via electron compensation and was favoured significantly over the V_{Ti} mechanism. The difference between the two potential models comes from the increase in energy required to substitute a Ti^{3+} ion at a Ti^{4+} site in the new model (49.23 eV –for the new model and 36.00 eV for the old model). This substantial increase arises from the stronger Ti-O potential fitted in the new model which causes a greater energetic penalty when Ti^{3+} is substituted. Regardless of this fact, the difference between the solution energy for electron compensation and the other schemes is somewhat surprising. In order to justify

this difference, calculations were carried to confirm the accuracy and validity of the Lewis and Catlow Ti^{3+} potential we have used. The Ti^{3+}-O^{2-} Buckingham potential was fitted before the discovery of covalency between the Ti and O ions [31]. We used DFT calculations to analyse and compare the local charge on the Ti atoms in rutile TiO_2, corundum Ti_2O_3 and perovskites $BaTiO_3$ and $LaTiO_3$. We used the Vienna *Ab initio* simulation package (VASP) [43] with the local density approximation (LDA) [44-45] and projector augmented-wave method [46-47]. A Γ-point centred 5 X 5 X 5 *k*-point mesh was used for Brillouin zone integration and a plane wave cutoff energy of 500 eV was applied for the calculations. The results of the Bader charge analysis [48] are given in table 4.9. Bader charge analysis works by dividing molecules into atomic volumes by zero flux surfaces where the charge density is a minimum perpendicular to the surface.

Crystal	Ti Formal Atomic Charge (a.u.)	Ti Bader Atomic Charge (a.u.)
TiO_2	+ 4.0	+ 2.67
$BaTiO_3$	+ 4.0	+ 2.21
Ti_2O_3	+ 3.0	+ 2.28
$LaTiO_3$	+ 3.0	+ 2.35

Table 4.9: Bader charge analysis of the Ti ion in TiO_2, $BaTiO_3$, Ti_2O_3 and $LaTiO_3$.

For the crystals with the Ti^{3+} ions, the Bader charge is significantly closer to the formal charge when compared to crystals containing Ti^{4+} ions. Furthermore, in the perovskite structure the Ti^{4+} ion has a smaller Bader charge than when in the binary oxide structure, this is not observed for Ti^{3+}. These results suggest the Buckingham potential should be adequate for the Ti^{3+}-O^{2-} interaction as Ti^{3+}-O^{2-} has less covalent character than Ti^{4+}-O^{2-}. Lattice statics calculations were also performed for Ti_2O_3 using the Lewis and Catlow potential and it was found that the potential was accurate for both the cohesive energy and lattice parameters. We therefore conclude there is no serious error associated with this potential.

Furthermore, recent experiments and calculations [49] completed using our new potential model have shown the energy required to remove oxygen from La-doped $BaTiO_3$ which has been charge compensated by titanium vacancies is less than the energy required for electron compensation. Calculations by Freeman *et al*. [49] show that for La concentrations ranging from the dilute limit to 12 mol%, compensation from titanium vacancies is favoured and that when oxygen vacancies are introduced to the system the energetic penalty is still far smaller than that of the electron compensation mechanism. The energy required to dope La and introduce oxygen vacancies (compensated for by the reduction of Ti^{4+} to Ti^{3+}) ranges from 3.23 eV at the dilute limit to 14.61 eV at 12 mol% La. This is in comparison to the much larger values of 9.06 eV at the dilute limit to 36.98 eV at 12 mol % La for electron compensation. This suggests the source of conduction in this doped material is indeed oxygen vacancies and not electron compensation as has been widely accepted since the 1960's. Further details on these calculations and the supporting experimental evidence are available in [49].

4.4 Rare-earth Doping of *h*-$BaTiO_3$

4.4.1 Defect Chemistry

The same five charge compensation mechanisms used for the doping of the cubic polymorph have been used for *h*-$BaTiO_3$. The cohesive energy of *h*-$BaTiO_3$ is calculated to be - 159.94 eV, the values for the vacancy and substitution energies are given in tables 4.10 and 4.11, respectively. All other values in the schemes are the same as in the cubic case. Unlike *c*-BaTiO3, *h*-$BaTiO_3$ has two crystallographically distinct sites for each element and therefore different defect energetics for each.

Ion Site	Vacancy Energy (eV)
Ba1	20.54
Ba2	20.25
Ti1	105.52
Ti2	101.39
O1	23.99
O2	26.55

Table 4.10: Vacancy energies for *h*-$BaTiO_3$.

The vacancy energies for *h*-$BaTiO_3$ are generally higher than those for *c*-$BaTiO_3$ as a result of the reduced interatomic distances between certain cations and oxygen ions and the generally more complex coordination environments. Exception to this is the energy for the O1 face-sharing ion. This is confirmed by a variety of experimental studies including findings from neutron diffraction studies for undoped [50], Ga-doped [51] and 3d transition-metal doped [11-12] *h*-$BaTiO_3$ which show that face-sharing oxygen vacancies (O1) are in higher concentrations than corner-sharing oxygen vacancies (O2). DFT simulations completed by Colson *et al.* [52] also calculated O1 vacancies to be more favourable than O2 vacancies. Similar to *c*-$BaTiO_3$, the most unfavourable defects are Ti vacancies. Our calculations suggest that the Ti1 site in *h*-$BaTiO_3$ is more stable than the Ti2 site as the Ti1 vacancy energy is higher than the Ti2 vacancy energy. It is proposed that this is due to the destabilisation from the shorter interatomic cation distance between the Ti2 sites (~ 2.9387 Å) within the face sharing dimers compared to the closest Ti1/Ti2 distance (~ 4.0730 Å) associated with corner shared octahedra and that this causes increased Coulombic repulsion in the former case. This is supported by the fact that cubic close packed perovskites based exclusively on corner shared BO_6 octahedra are far more common than hexagonal close packed perovskites where face sharing octahedra are present such as *h*-$BaTiO_3$. Tolerance factors also play an important role in the favouring of the cubic structure over the hexagonal structure.

	Ba-site substitution, $E^{M^{3+}}_{sub,Ba}$(eV)		Ti-site substitution, $E^{M^{3+}}_{sub,Ti}$ (eV)	
Defect Ion (3+)	Ba1 site	Ba2 site	Ti1 site	Ti2 site
La	- 21.66	- 21.16	58.34	58.19
Nd	- 22.74	- 22.18	56.00	55.85
Eu	- 23.49	- 22.89	54.34	54.19
Gd	- 23.65	- 23.05	53.91	53.76
Ho	- 24.43	- 23.82	52.19	52.01
Yb	- 24.90	- 24.25	50.97	50.76
Lu	- 25.13	- 24.45	50.51	50.28
Ti	-	-	49.42	49.52

Table 4.11: Substitution energies for *h*-$BaTiO_3$.

Similarly to the cubic polymorph, the substitution energies are consistent with ion-size arguments. In the case of Ba-site substitution, Ba1 site doping is energetically preferred. For Ti-site substitution, the Ti2 site is preferred (with the exception of Ti^{3+} substitution). It is noteworthy to add that the energy difference between Ti1 site and Ti2 site doping is small compared to the difference between Ti vacancies.

4.4.2 Solution Energies for *h*-$BaTiO_3$

To take into account the effects of charge compensation, solution energies were calculated for each metal cation site. The solution energies for the lowest energy configurations (i.e. the configurations with the lowest substitution and vacancy energies) are presented in table 4.12.

Rare Earth	Ionic Radii (Å)	Solution Energy, E_s (eV)				
		$RE_{Ba1} + e_{Ti1}$	$RE_{Ba1} + V_{Ti2}$	$RE_{Ti2} + V_{O1}$	$RE_{Ba1} + RE_{Ti2}$	$RE_{Ba1} + V_{Ba2}$
La	1.032	9.96	2.37	5.62	1.41	2.67
Nd	0.983	10.83	2.85	4.84	1.26	3.15
Eu	0.947	11.96	3.69	4.78	1.65	4.00
Gd	0.938	11.58	3.83	4.65	1.66	4.14
Ho	0.901	12.27	4.41	4.26	1.76	4.72
Yb	0.868	12.86	4.94	4.01	1.90	5.25
Lu	0.861	12.59	5.13	3.95	1.96	5.44

Table 4.12: Solution energies of the lowest energy configurations for doping of *h*-$BaTiO_3$.

The solution energies show that self-compensation at the Ba1 and Ti2 sites is the favoured mechanisms for all the RE ions. For the other mechanisms, vacancies are preferred at the O1, Ba2 and Ti2 sites. As previously discussed, these solution energies do not take into account the binding energy between the charged defects and they only represent isolated defects.

4.4.3 Binding Energies for *h*-$BaTiO_3$

Within the hexagonal phase there are numerous possible configurations of defects and hence numerous binding energies with varying magnitudes. All nearest and second nearest neighbour configurations were simulated and the most favourable binding energies for the lowest energy configurations (table 4.12) are given in table 4.13.

Rare Earth	Ionic Radii (Å)	Binding Energy, E_s (eV)				
		$RE_{Ba1} + e_{Ti1}$	$RE_{Ba1} + V_{Ti2}$	$RE_{Ti2} + V_{O1}$	$RE_{Ba1} + RE_{Ti2}$	$RE_{Ba1} + V_{Ba2}$
La	1.032	- 0.56	- 5.29	- 6.69	- 0.68	- 1.54
Nd	0.983	- 0.56	- 5.58	- 6.57	- 0.71	- 1.59
Eu	0.947	- 0.55	- 5.90	- 6.55	- 0.74	- 1.70
Gd	0.938	- 0.55	- 6.04	- 6.56	- 0.78	- 1.76
Ho	0.901	- 0.55	- 6.59	- 6.57	- 0.89	- 2.03
Yb	0.868	- 0.55	- 7.24	- 6.66	- 1.02	- 2.39
Lu	0.861	- 0.54	- 7.60	- 6.64	- 1.08	- 2.54

Table 4.13: Binding energies of the lowest energy cluster configurations for doping of *h*-$BaTiO_3$.

For scheme 1 (RE_{Ba} + electron compensation) the binding energies are relatively weak and no strong trend is observed with dopant ion size. Such small energies are a result of the interaction between a (+1) charged defect site (RE_{Ba}) and a (-1) charged defect site (Ti'_{Ti}). We suggest that the large distance between the Ba1 and Ti1 sites explains why the energies show no strong trend and remain reasonably constant with dopant ion size.

In comparison to scheme 1, the binding energies for scheme 2 ($RE_{Ba} + V_{Ti}$) are far larger and a clear trend of increasing binding energy with decreasing RE ion size is observed. These large energies are caused by the strong interaction between the Ti vacancy (charge -4) and RE_{Ba} (charge +1) defects and the proximity of these defects. The same explanation suggested for the cubic polymorph of the increase of the RE-O interaction with the dopant size decrease and that the negatively charged V_{Ti} further pushes the O anions towards the RE cation is proposed.

Like scheme 2, scheme 3 ($RE_{Ti} + V_O$) also has large binding energies, but the energies are far less affected by the decrease in ion size from La to Lu. The strong interaction between the negatively charged O vacancy and positively charged RE_{Ti} sites

is the cause of these large values. The lowest energy configuration for this scheme (RE_{Ti2} + V_{O1}) exhibits a unique pattern is observed. For the other configurations tested a trend similar to *c*-$BaTiO_3$ was observed, i.e. the binding energy became less negative with decreasing dopant ion size. However, for this configuration the binding energy becomes less negative with decreasing ion size up to Eu and then for smaller ions the binding increases up to Yb. Simulations on this configuration show that larger RE ions such as La cause other O1 ions to be marginally displaced as the La-O bonds are longer than, for example, shorter and stronger Lu-O bonds. In this particular configuration the separation between the O1 ions and the RE_{Ti2} sites is significantly smaller compared to that in the rest of the lattice which restricts the displacement of the O1 ions as illustrated by figure 4.5. This suggests a possible strain effect where there is competition between the energetically favoured larger RE^{3+} cations and the strain that these large cations cause.

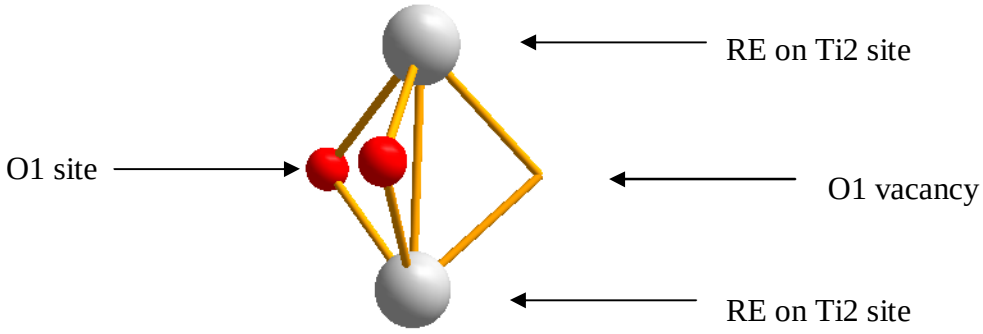

Figure 4.5: Representation of the strongest binding energy defect cluster for scheme 3 in *h*-$BaTiO_3$ [53] (explicit permission to reuse this image has been granted).

For scheme 4 (RE_{Ba} + RE_{Ti}) relatively weak binding energies are observed that increase with decreasing RE ion size. Like scheme 1, this scheme only has a singly charged positive defect and a singly charged negative defect. However, unlike scheme 1 there is a trend with RE ion size which is caused by the stronger RE-O interactions formed as a result of the increased charge density of the smaller RE^{3+} ions.

Scheme 5 exhibits the same trend as scheme 2; however, the binding energies are not as strong as the vacancy now has a charge of -2 as opposed to the -4 charge of V_{Ti} in scheme 2.

A comparison of the binding energies for the cubic and hexagonal polymorphs of $BaTiO_3$ yields a few notable differences. However, it should be noted that direct comparison between different crystal structures can be difficult. Generally, the magnitude of the binding energies is greater in *h*-$BaTiO_3$ and this is especially true for schemes 2 and 5. In *c*-$BaTiO_3$, the four RE_{Ba} ions are located in the cubic plane, which causes an increase in repulsion in the system. However in *h*-$BaTiO_3$ the separation between the Ba-sites is generally much larger, meaning the repulsion is far less which results in a stronger binding energy. This is also true for the $RE_{Ba1} + V_{Ti2}$/ $RE_{Ba1} + V_{Ba2}$ configurations. Generally, the trends in the binding energies between the two structures are similar with the exception of the example for scheme 3 as previously discussed.

4.4.4 Binding Modified Solution Energies for *h*-$BaTiO_3$

The solution energies modified with the appropriate fraction of binding energy were calculated and the results for the lowest energy configuration are presented in table 4.14 and graphically in figure 4.6.

Rare Earth	Ionic Radii (Å)	Binding Modified Solution Energy, E_s (eV)				
		$RE_{Ba1} + e_{Ti1}$	$RE_{Ba1} + V_{Ti2}$	$RE_{Ti2} + V_{O1}$	$RE_{Ba1} + RE_{Ti2}$	$RE_{Ba1} + V_{Ba2}$
La	1.032	9.40	1.04	2.28	1.07	1.90
Nd	0.983	10.27	1.45	1.56	0.91	2.36
Eu	0.947	11.41	2.21	1.50	1.28	3.15
Gd	0.938	11.03	2.32	1.37	1.27	3.26
Ho	0.901	11.72	2.77	0.98	1.31	3.71
Yb	0.868	12.31	3.13	0.68	1.39	4.06
Lu	0.861	12.05	3.23	0.63	1.42	4.17

Table 4.14: Binding modified solution energies of the lowest energy configurations for doping of *h*-$BaTiO_3$.

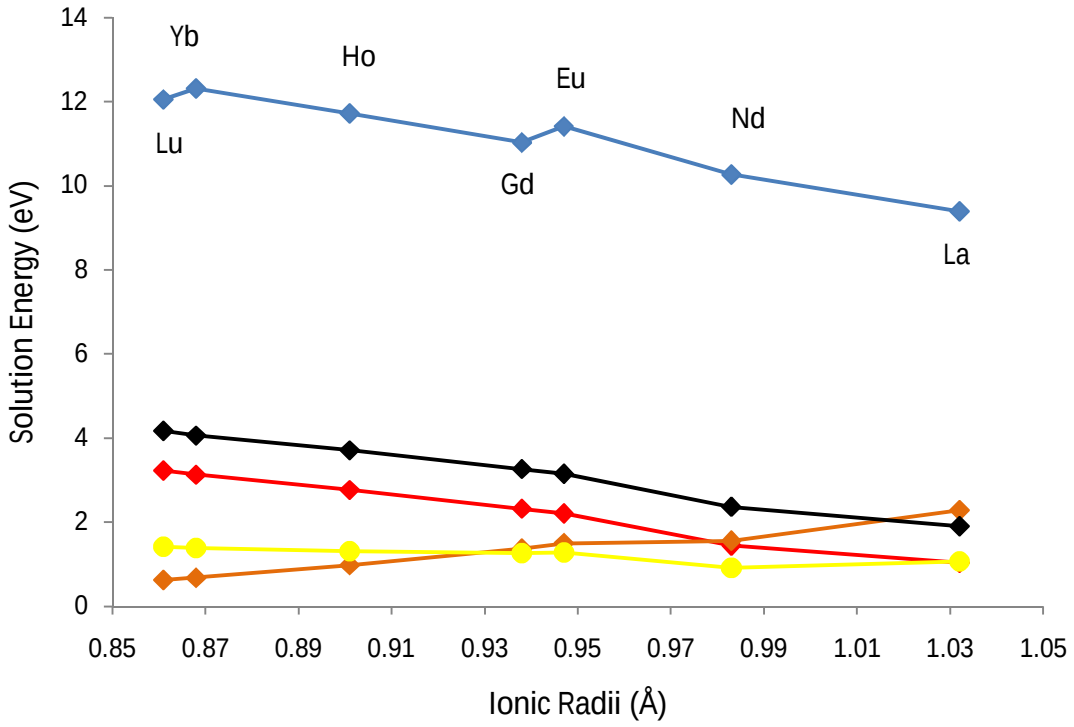

Figure 4.6: Solution energies for the five charge compensation schemes modified by the addition of the defect binding energies for *h*-$BaTiO_3$. Code: Blue – Scheme 1 (RE_{Ba} + e^-); Red – Scheme 2 (RE_{Ba} + V_{Ti}); Orange – Scheme 3 (RE_{Ti} + V_O); Yellow – Scheme 4 (RE_{Ba} + RE_{Ti}); Black – Scheme 5 (RE_{Ba} + V_{Ba}).

Again the most noticeable feature of figure 4.6 is the high energy cost of doping via the electron compensation mechanism. This mechanism is ~ 7-8 eV higher in energy than the next most favourable compensation scheme. Scheme 5 is not the preferential scheme for any of the RE dopants. This is in good agreement with experiment as the scheme is considered less plausible than the other four mechanisms in *h*-$BaTiO_3$ [54], at least for samples prepared in air.

Like the cubic phase, Nd appears to be more energetically favourable than would be expected on the basis of its ion size alone. This effect, however, is not as strong as in the cubic phase and is again a result of the interatomic potential producing a more positive cohesive energy in comparison to its size which means it is easier to remove

Nd from its oxide environment. It is, however, interesting to note that the largest solid solution for the self-compensation mechanism found from experimental studies is for Nd [54].

For scheme 2, an interesting feature is observed where there are two competing low energy defect configurations. The mechanism favoured is based entirely on the doping RE ion, as illustrated by table 4.15 and figures 4.7 and 4.8.

	Solution Energy (eV)		Binding Energy (eV)		Final Energy (eV)	
Rare Earth	$RE_{Ba1} + V_{Ti2}$	$RE_{Ba2} + V_{Ti2}$	$RE_{Ba1} + V_{Ti2}$	$RE_{Ba2} + V_{Ti2}$	$RE_{Ba1} + V_{Ti2}$	$RE_{Ba2} + V_{Ti2}$
La	3.19	3.75	- 6.94	- 8.30	1.46	1.67
Nd	3.83	4.44	- 7.36	- 9.53	1.99	2.06
Eu	4.80	5.43	- 7.83	- 10.63	2.84	2.77
Gd	4.96	5.60	- 7.99	- 10.96	2.97	2.86
Ho	5.67	6.35	- 8.91	- 12.52	3.44	3.22
Yb	6.28	6.98	- 9.14	- 13.92	4.00	3.50
Lu	6.50	7.20	- 9.87	- 14.40	4.03	3.60

Table 4.15: Comparison of two Scheme 2 defect configuration energetics for *h*-$BaTiO_3$.

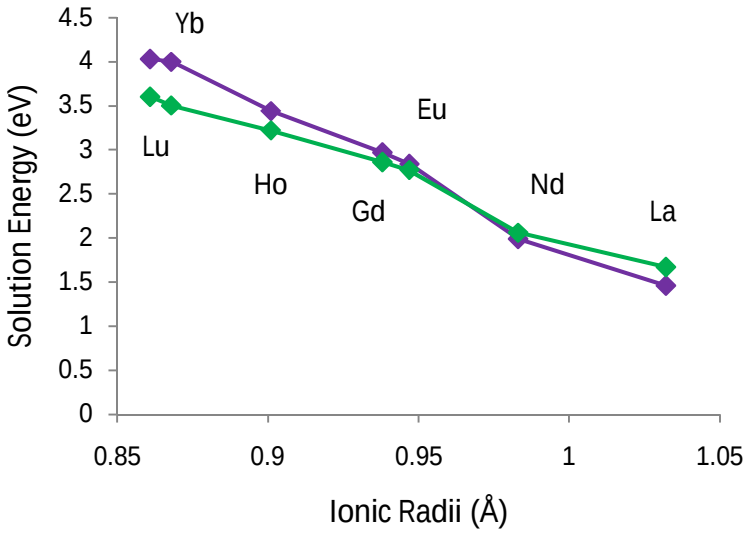

Figure 4.7: Binding modified solution energies of two defect configurations for Scheme 2 versus dopant ionic radius for doped *h*-$BaTiO_3$. Code: Purple - RE_{Ba1} + V_{Ti2}; Green - RE_{Ba2} + V_{Ti2}.

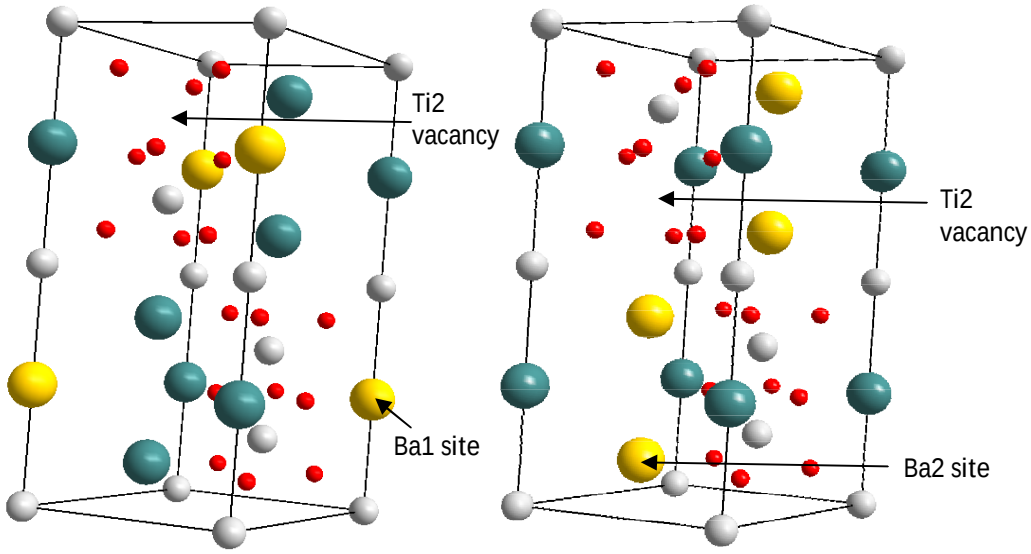

Figure 4.8: Lowest energy binding clusters for two scheme 2 configurations - (a) RE_{Ba1} + V_{Ti2} (b) RE_{Ba2} + V_{Ti2}. Code: Blue – Barium, Red – Oxygen, White – Titanium and Yellow – Rare Earth dopant at a Ba1site (a) or a Ba2 site (b) [53] (explicit permission to reuse this image has been granted).

Figure 4.7 is a clear illustration of how important the binding energies are and how can they influence the final solution energies for the RE ions. For La- and Nd-doping, the $RE_{Ba1} + V_{Ti2}$ configuration (also featured in figure 4.6) is energetically preferred. However, as the RE ion size decreases the binding energies for the $RE_{Ba2} + V_{Ti2}$ configuration become far more significant meaning that for RE ions smaller than Nd, this configuration becomes more energetically preferable. It is thought that the strong binding energy for small ions in this configuration is due to the close proximity of the RE_{Ba2} sites and the Ti2 vacancy, as shown in figure 4.8 (b). This proximity results in a strong interaction between the -4 charged vacancy and the surrounding +1 charged RE substitution defects.

A similar 'crossover' effect is observed for the electron compensation scheme. Although the $RE_{Ba1} + e_{Ti1}$ configuration has the lowest solution energies, the $RE_{Ba1} + e_{Ti2}$ configuration has stronger binding energies. This means that larger dopant ions with generally weaker binding energies prefer the $RE_{Ba1} + e_{Ti1}$ configuration, whereas mid-sized and smaller ions with generally stronger binding energies prefer the $RE_{Ba1} + e_{Ti2}$ configuration.

4.4.5 Comparison with *c*-$BaTiO_3$

There is a lot of similarity in the behaviour of these two polymorphs of $BaTiO_3$. The same ion size trends are observed and also the same compensation schemes are preferred for certain ions, for example large ions again prefer La prefer A-site occupation. Mid-sized ions such as Nd prefer self-compensation and small ions like Yb prefer substitution at the Ti-site with an oxygen vacancy mechanism, all in agreement with experimental findings [54-55] and the results for the cubic polymorph.

There is, however, a difference between the relative energies of the schemes in the two polymorphs. For example Ba-site doping is generally less favoured in the hexagonal polymorph as shown by the solution energies of schemes 1, 2, 5 and to a lesser extent scheme 4 in comparison to the cubic polymorph. The main reasons for this are that the energies for Ba and Ti vacancies in the hexagonal phase are higher than in

the cubic phase and Ba-site substitution energies are not as favourable as in the cubic phase. Conversely, for scheme 3 the lowest energy configuration for *h*-$BaTiO_3$ is lower in energy for mid and small sized RE ions than the equivalent scheme in *c*-$BaTiO_3$. This is a direct result of the strong binding energies in this configuration and the low energy cost for V_{O1} in *h*-$BaTiO_3$. It should be noted that such comparisons only apply to the lowest energy (and therefore theoretically most likely) defect configurations of *h*-$BaTiO_3$. Other less favourable configurations produce significantly different results albeit with the same general trends.

4.5 Phase Stabilisation of Transition Metal Doped *h*-$BaTiO_3$

4.5.1 Defect Chemistry

The existence of multivalent states of transition metal dopant ions means that a different charge compensation scheme is necessary for each valence state. We have considered dopant ions in the 2+, 3+ and 4+ charge states and the appropriate charge compensation schemes are taken from Akhtar *et al.* [32]. The schemes have been reproduced for the convenience of the reader (Eqns. 4.16 - 4.22). Only Ti-site substitution has been considered in this section as this is the cause of the stabilisation of the hexagonal polymorph.

1. Substitution of M^{2+} at Ti^{4+} sites with O^{2-} vacancy compensation.

$$MO + Ti_{Ti} + O_O \longrightarrow M''_{Ti} + V_O^{\bullet\bullet} + TiO_2 \tag{4.11}$$

$$E_S = E_{sub,Ti}^{M^{2+}} + O_{vac}^{2-} + E_L^{TiO_2} - E_L^{MO} \tag{4.12}$$

2. Substitution of M^{3+} at Ti^{4+} with O^{2-} vacancy compensation.

$$M_2O_3 + 2Ti_{Ti} + O_O \longrightarrow 2M'_{Ti} + V_O^{\bullet\bullet} + 2TiO_2 \tag{4.13}$$

$$E_s = \frac{1}{2}[2E_{sub,Ti}^{M^{3+}} + E_{vac}^{O^{2-}} + 2E_L^{TiO_2} - E_L^{M_2O_3}] \tag{4.14}$$

3. Substitution of M^{4+} at Ti^{4+} sites.

$$MO_2 + Ti_{Ti} \longrightarrow M_{Ti} + TiO_2 \quad (4.15)$$

$$E_S = E_{sub,Ti}^{M^{4+}} + E_L^{TiO_2} - E_L^{MO_2} \quad (4.16)$$

In addition to these schemes, we have also considered the oxidation of Ni^{2+} to Ni^{3+} (Eqns. 4.17 and 4.18) and Fe^{3+} to Fe^{4+} (equations (4.19) and (4.20)) during incorporation at the Ti-site in $BaTiO_3$ (the equations have been reproduced from Buscaglia *et al.* [27]).

$$2NiO + 2Ti_{Ti} + O_o + \frac{1}{2}O_2 \longrightarrow 2Ni'_{Ti} + V_O^{\bullet\bullet} + 2TiO_2 \quad (4.17)$$

$$E_S = \frac{1}{2}\left[\left(2E_{sub,Ti}^{Ni^{3+}} + 2E_{ion}^{III,Ni}\right) + E_{vac}^{O^{2-}} + \left(E_A^{O^{2-}} + \frac{1}{2}D_{O_2}\right) + 2E_L^{TiO_2} - 2E_L^{NiO}\right] \quad (4.18)$$

$$Fe_2O_3 + 2Ti_{Ti} + \frac{1}{2}O_2 \longrightarrow 2Fe_{Ti} + 2TiO_2 \quad (4.19)$$

$$E_S = \frac{1}{2}\left[\left(2E_{sub,Ti}^{Fe^{4+}} + 2E_{ion}^{IV,Fe}\right) + \left(E_A^{O^{2-}} + \frac{1}{2}D_{O_2}\right) + 2E_L^{TiO_2} - E_L^{Fe_2O_3}\right] \quad (4.20)$$

For transition metal doping the energy of solution for a particular dopant ion is calculated from a number of values; the cohesive energies of its oxide and of TiO_2, the oxygen vacancy energy and its substitution energy at the relevant Ti-site. Table 4.16 shows the calculated substitution and cohesive energies for each transition metal ion. The cohesive energies for Ni_2O_3 and FeO_2 are omitted as they are not required for the oxidation mechanisms. For the solution energy of the oxidation schemes, extra terms are required; these terms are described in table 4.17. The second electron affinity of oxygen ($E_A^{O^{2-}}$) for both transition metal oxides has again been calculated using a Born-

Haber cycle with values taken from the literature [36, 39, 56]. All other values have been previously discussed.

Transition Metal	Cubic - $E_{sub,Ti}^{M^{3+}}$(eV)	Hexagonal (Ti1) - $E_{sub,Ti1}^{M^{3+}}$ (eV)	Hexagonal (Ti2) - $E_{sub,Ti2}^{M^{3+}}$ (eV)	Cohesive energy, $E_L^{M_2O_3}$ (eV)
Co^{2+}	70.50	72.45	71.11	- 41.06
Mn^{2+}	72.76	74.53	73.26	- 38.90
Ni^{2+}	69.77	71.79	70.41	- 41.84
Co^{3+}	40.62	41.34	40.38	- 158.13
Fe^{3+}	43.59	44.24	43.55	- 150.85
Mn^{3+}	43.14	43.79	43.09	- 151.93
Ni^{3+}	41.38	42.08	41.20	-
Co^{4+}	9.35	9.21	8.86	- 116.47 [57]
Mn^{4+}	12.36	12.24	12.20	- 114.41
Fe^{4+}	8.86	8.72	8.39	-

Table 4.16: Substitution and cohesive energies for transition metal dopants at Ti-sites in $BaTiO_3$.

Term	Description	Value (eV)
$E_{ion}^{III,Ni}$	Third ionization energy of Ni	35.17
$E_{ion}^{IV,Fe}$	Fourth ionization energy of Fe	54.80
$E_A^{O^{2-}}$ (NiO)	Sum of the first and second electron affinities for oxygen in NiO	6.46
$E_A^{O^{2-}}$ (Fe_2O_3)	Sum of the first and second electron affinities for oxygen in Fe_2O_3	5.57

Table 4.17: Description of terms used in the calculation of transition metal solution energies in $BaTiO_3$.

Substitutions of divalent ions into the cubic polymorph require less energy than at both Ti sites in *h*-$BaTiO_3$. For trivalent ions, however, Ti2 substitution within the Ti_2O_9 dimers of the hexagonal polymorph is more favourable and both hexagonal Ti-sites are preferred over the cubic polymorph for tetravalent dopants. The difference in substitution energy between the different charge states of the dopant ions is dramatic, for example there is an energetic difference of 62.29 eV between Mn^{2+} and Mn^{4+} at the Ti1 site in *h*-$BaTiO_3$. While these energies suggest that Ti-site substitution is more favourable in the hexagonal polymorph for higher charged dopants, they only represent an isolated defect.

4.5.2 Transition Metal Solution Energies for *c*- and *h*-$BaTiO_3$

Solution energies for both the cubic and hexagonal polymorphs are given in table 4.18. For the hexagonal polymorph, solution energies are given for each possible defect configuration. Also as no oxygen vacancy compensation is required for Mn^{4+} and Co^{4+} substitution and the oxidation of Fe^{3+}, only two values are presented for each dopant ion.

Generally, the energies of solution for the *h*-$BaTiO_3$ polymorph are higher than those of the cubic polymorph, with the exception of doping at the Ti2 sites with O1 vacancies. With regard to the ionic radii of the dopant ions, a general trend exists where the larger ions have lower solution energy. This is contrary to that observed for trivalent rare earth dopants, where a decrease in ionic radius resulted in a decrease in solution energy. This suggests that smaller transition metal ions are more stable in their oxides than in the $BaTiO_3$ environment. This is clearly observed from the cohesive and substitution energies given in table 4.16. For example, the cohesive energy of Co_2O_3 is 6.2 eV lower than that of Mn_2O_3, whereas the substitution energy of Co^{3+} is only 2.3 eV lower than that of Mn^{3+} in *c*-$BaTiO_3$. This is also true for divalent ions, although to a lesser extent as seen by the small difference in solution energies for each configuration.

		Solution Energy, E_s (eV)				
		c-$BaTiO_3$	*h*-$BaTiO_3$			
Transition Metal	Ionic Radii (Å)	Ti/O	Ti1/O1	Ti1/O2	Ti2/O1	Ti2/O2
Co^{2+}	0.65	8.58	9.86	12.42	8.52	11.08
Mn^{2+}	0.67	8.68	9.78	12.34	8.51	11.07
Ni^{2+}	0.69	8.63	9.98	12.54	8.60	11.16
Co^{3+}	0.55	4.38	4.76	6.04	3.80	5.08
Fe^{3+}	0.55	3.71	4.02	5.30	3.33	4.61
Mn^{3+}	0.58	3.80	4.11	5.39	3.41	4.69
Co^{4+}	0.53	- 1.82	-1.96	-1.96	- 2.31	- 2.31
Mn^{4+}	0.53	- 0.87	- 0.99	- 0.99	- 1.03	- 1.03
$Ni^{2+} \rightarrow Ni^{3+}$	$0.69 \rightarrow 0.56$	7.60	7.97	9.25	7.09	8.37
$Fe^{3+} \rightarrow Fe^{4+}$	$0.55 \rightarrow 0.59$	15.52	15.38	15.38	15.05	15.05

Table 4.18: Solution energies for transition metal doping of *c*-$BaTiO_3$ and *h*-$BaTiO_3$.

The oxidation of Ni^{2+} to Ni^{3+} is energetically more favourable in both polymorphs than the incorporation of Ni^{2+} without oxidation. This seems reasonable as experimentally Ni has been observed in various valence states; however, no Ni^{2+} was detected [20]. Alternatively, the opposite is true for the oxidation of Fe^{3+} where solution energies of greater than 15 eV were calculated as a result of the high fourth ionization potential of Fe. Again this correlates well with experiment as Fe^{4+} ions are only observed in small concentrations and Fe^{3+} exists as the dominant species [19, 58].

4.5.3 Transition Metal Binding Energies for *c*- and *h*-$BaTiO_3$

Given the high charges and relatively small ionic radii of the defects, it would be expected that the binding energies of these defect clusters will be high and this is indeed

the case. Table 4.19 gives the binding energies for each cluster. The magnitude of the binding, however, varies significantly between the charge of the dopant ion and the substituting site/oxygen site in the case of the hexagonal polymorph. No binding energies exist for tetravalent ions as there is no requirement for oxygen vacancy compensation.

		Binding Energy (eV)				
		c-$BaTiO_3$	*h*-$BaTiO_3$			
Transition Metal	Ionic Radii (Å)	Ti/O	Ti1/O1	Ti1/O2	Ti2/O1	Ti2/O2
Co^{2+}	0.65	- 4.16	- 1.67	- 6.28	- 5.22	- 6.25
Mn^{2+}	0.67	- 4.32	- 1.72	- 6.37	- 5.24	- 6.21
Ni^{2+}	0.69	- 4.14	- 1.66	- 6.30	- 5.26	- 6.32
Co^{3+}	0.55	- 6.59	- 1.16	- 5.18	- 7.82	- 5.60
Fe^{3+}	0.55	- 6.61	- 1.20	- 5.12	- 7.66	- 5.43
Ni^{3+}	0.56	- 6.50	- 1.16	- 5.10	- 7.63	- 5.46
Mn^{3+}	0.58	- 6.42	- 1.15	- 5.00	- 7.46	- 5.29

Table 4.19: Binding energies for transition metal doping of *c*-$BaTiO_3$ and *h*-$BaTiO_3$.

For the cubic polymorph, the binding between two trivalent ions doped at Ti-sites (-1 charge) and an O vacancy (+2 charge) is significantly stronger than the binding between a divalent ion doped at a Ti-site (-2 charge) and an O vacancy. This suggests that, although a divalent dopant creates a (-2) charged site, the two smaller singly charged trivalent dopant sites have a stronger electrostatic interaction with the O vacancy. With regard to divalent ions, a clear trend exists between the ionic radius of the ions and the binding energy. The binding energy becomes more negative with increasing ionic radius of the M^{2+} dopant; the same trend that was observed for trivalent rare earth doping. This

is the result of the energy loss caused by the loss of an M-O interaction associated with an oxygen vacancy. This energy loss is more significant for stronger M-O interactions as is the case for Ni^{2+} and Co^{2+} ions. Such an energy penalty means the binding energies of smaller dopant ions are not as strong as those for larger dopant ions. There is no such trend for trivalent dopants as the difference in ionic radius is minimal and there is only small variation in the magnitude of the binding energy.

The binding energies between *h*-$BaTiO_3$ configurations differ significantly. This is especially the case for the Ti1/O1 configuration, where the difference in binding energies of both di and trivalent dopant clusters to other configurations is of the order of at least 4 eV. The reason for such poor binding in this configuration is simply the increased distance between the Ti1 and O1 sites compared to the distance between other defect sites. The shortest interatomic distance between a Ti1 site and an O1 site is 4.52 Å, whereas, for example, the shortest distance between a Ti1 and an O2 site is only 1.98 Å. The Coulombic interaction is lessened in the Ti1/O1 configuration. For divalent dopant ions, the Ti1/O2 and Ti2/O2 configurations have the strongest binding energy as a result of their close proximity (1.98 Å and 1.96 Å, respectively). The lowest energy cluster for the trivalent dopants is the Ti2/O1 cluster; as with rare earth doping this is primarily due to the O1 sites being directly in between two Ti2 sites. This creates strong binding between the two (-1) charged dopant sites and the (+2) charged oxygen vacancy site without substantial Coulombic repulsion between the dopant ions.

Unlike the cubic polymorph, binding energies of divalent dopants and oxygen vacancies are stronger than those for trivalent dopants in the hexagonal polymorph, with the exception of the Ti2/O1 configuration. While it has been stated that the distance between most defect pairs is small, in the case of trivalent dopants, binding occurs between two dopants and one oxygen vacancy and in all configurations (excluding Ti2/O1) the distance between the oxygen vacancy and the second dopant site is much larger, thus weakening the Coulombic interaction. This is illustrated for the Ti2/O2 configuration by figure 4.9. For this particular cluster there is also increased Coulombic repulsion between the M^{3+} ions. This of course is not the case in the cubic

polymorph as an oxygen vacancy can sit an equal distance away from two dopant sites. Generally, there is little correlation between ionic radius and binding energy in the hexagonal polymorph. This is most likely due to the relatively small change in ionic radius, especially for the trivalent dopants. The variation in magnitude of binding energies between different dopants is also small.

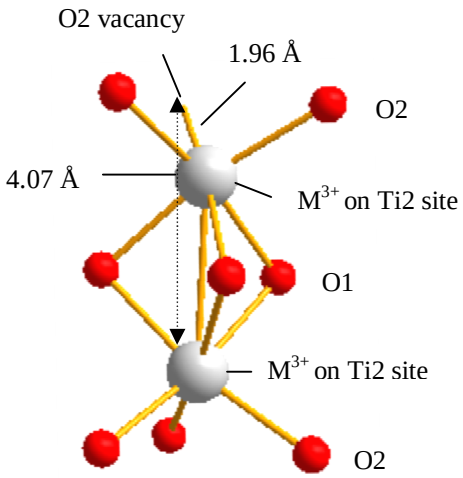

Figure 4.9: Interatomic distances between an O2 vacancy and its first and second M^{3+} dopant neighbours for the Ti2/O2 defect cluster in *h*-$BaTiO_3$.

The magnitude of binding energies for all divalent dopant ions in the hexagonal polymorph, excluding the Ti1/O1 configuration, is larger than in the cubic polymorph, whereas for trivalent ions the opposite is true, excluding the strong binding energies of the Ti2/O1 cluster. The reasoning for these observations has been previously touched upon; the distance between such defect pairs is somewhat shorter in the hexagonal polymorph meaning a stronger Coulombic interaction. However for trivalent dopants, the distance between the defects in the cluster is greater in the hexagonal polymorph which weakens the Coulombic interaction.

4.5.4 Transition Metal Binding Modified Solution Energies for *c*- and *h*-$BaTiO_3$

For divalent ions, the full binding energy is used, whereas for trivalent ions only half the binding energy is used as determined by the fraction in the charge compensation scheme (equation (4.14)). All final solution energy results are presented in table 4.20. Results for the cubic polymorph and the lowest energy cluster of the hexagonal polymorph (Ti2/O1) are plotted in figure 4.10.

		Binding Modified Solution Energy, E_s (eV)				
		c-$BaTiO_3$	*h*-$BaTiO_3$			
Transition Metal	Ionic Radii (Å)	Ti/O	Ti1/O1	Ti1/O2	Ti2/O1	Ti2/O2
Co^{2+}	0.65	4.42	8.19	6.14	3.30	4.83
Mn^{2+}	0.67	4.36	8.06	5.97	3.27	4.86
Ni^{2+}	0.69	4.49	8.32	6.24	3.34	4.84
Co^{3+}	0.55	1.09	4.18	3.45	- 0.11	2.28
Fe^{3+}	0.55	0.41	3.42	2.74	- 0.50	1.90
Mn^{3+}	0.58	0.59	3.54	2.89	- 0.32	2.05
Co^{4+}	0.53	- 1.82	- 1.96	- 1.96	- 2.31	- 2.31
Mn^{4+}	0.53	- 0.87	- 0.99	- 0.99	- 1.03	- 1.03
$Ni^{2+} \rightarrow Ni^{3+}$	0.69 → 0.56	4.35	7.39	6.70	3.28	5.64
$Fe^{3+} \rightarrow Fe^{4+}$	0.55 → 0.59	15.52	15.38	15.38	15.05	15.05

Table 4.20: Binding modified solution energies for transition metal doping of *c*-$BaTiO_3$ and *h*-$BaTiO_3$.

Unlike the binding energies, there exists a general trend between ionic radius and solution energy in this data. For di and trivalent ions, an increase in ionic radius is met with a decrease in solution energy (with the exception of the divalent Ti2/O2 cluster). This trend is continued from the starting solution energies for divalent dopants and for the majority of configurations. The more negative binding energies of larger dopants strengthen this trend. Similarly, the same trend is observed in the original solution energies for trivalent ions and can be accounted for by the energetic favorability of the environment of the smaller dopant ions in the binary oxide compared to that in $BaTiO_3$.

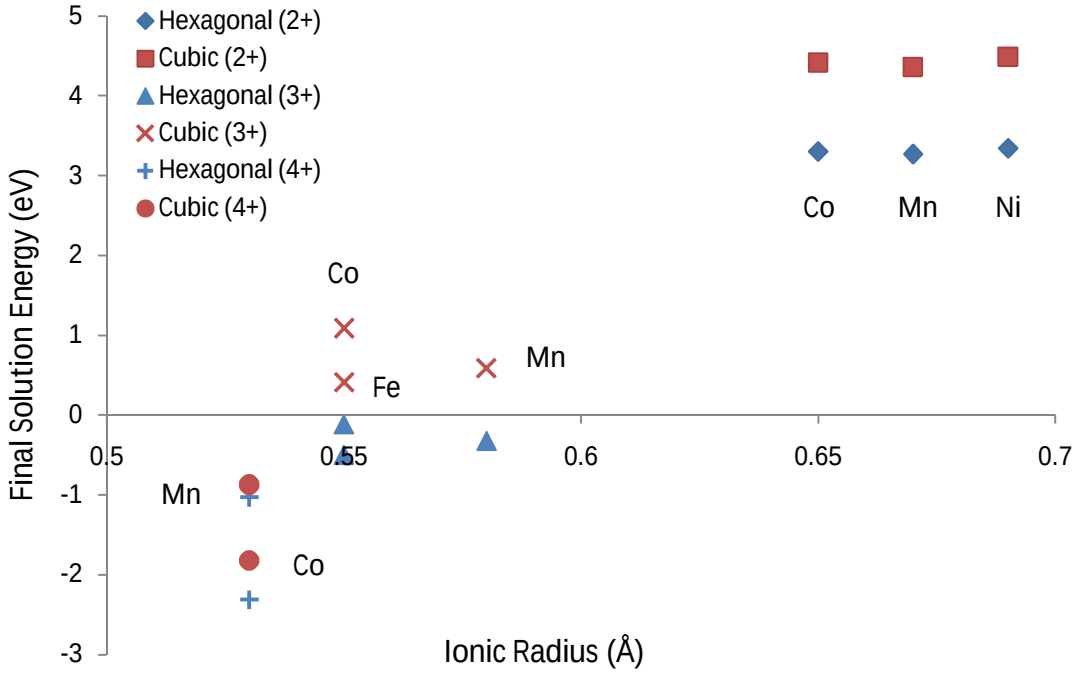

Figure 4.10: Binding modified solution energies versus ionic radius for multivalent transition metal doped *c*-$BaTiO_3$ and *h*-$BaTiO_3$ (Ti2/O1 defect configuration).

Oxidation of Ni^{2+} to Ni^{3+} on incorporation into *c*-$BaTiO_3$ is 0.14 eV energetically more favourable than incorporation without oxidation. For *h*-$BaTiO_3$, oxidation is preferred for compensation via an O1 site vacancy. As discussed above, it has been shown through both experiment and modelling that corner sharing O2 vacancies are not as favoured as O1 vacancies. It can therefore be assumed that Ni^{2+} oxidation is likely during incorporation into *h*-$BaTiO_3$. Fe^{3+} oxidation to Fe^{4+} is energetically unfavourable in both polymorphs. These observations are confirmed by experiment [19-20]. Figure 4.10 clearly shows the preference for the incorporation of higher charged dopant ions for samples prepared in air. For example the final solution energy for Mn^{2+} in the cubic polymorph is 4.36 eV, compared to – 0.87 eV for Mn^{4+}. While it is difficult to suggest that such a small value is also the case for other tetravalent ions, it is certain that on the basis of these calculations the major concentration of dopant ions will be in the trivalent state and tetravalent state (when available). Given the large size of the divalent ions compared to the Ti^{4+} ion, this seems a reasonable a conclusion and is supported experimentally where trivalent dopants are most commonly observed [13-15, 19].

The Ti2/O1 dopant pair/cluster is again the lowest in energy for the hexagonal polymorph and is also lower in energy than the cubic polymorph for all dopant ions, as shown by figure 4.10. For the trivalent ions, the solution energy becomes negative for this configuration which suggests an actual energetic stabilisation occurs with the introduction of these ions. This is also true for tetravalent ions doping at either Ti-site in *h*-$BaTiO_3$, but to a lesser extent. Additionally, there is a significant reduction in solution energy of ~ 1.1 eV for divalent ions. These results strongly suggest that a significant stabilisation of the hexagonal polymorph takes place with the incorporation of transition metal ions occupying the Ti2 sites. This energetic preference may explain why transition metal doping of the undoped cubic polymorph lowers the phase transition temperature for the hexagonal polymorph and can result in full stabilisation at room temperature for low levels of doping, i.e. ~ 2-5 at%. Excluding configurations involving the unfavourable O2 vacancies, the only possible configuration for Ti1 site doping is the Ti1/O1 configuration, however, this configuration is also the highest in energy. This

suggests a considerable preference for Ti2 site occupation and that the concentration of Ti1 sites occupied is low in comparison. Experimentally, site preference is dependent on the dopant ion [15].

4.6 Conclusions

Using a newly designed $BaTiO_3$ potential set capable of accurately reproducing its structural and energetic properties, classical simulations have been carried out on the RE and transition metal doping of *c*- and *h*-$BaTiO_3$. Excellent agreement with experiment has been observed for RE doping and substantial improvements on the results from the previous model have been made. La-doping in both polymorphs has been shown to occur via Ti-site vacancies and that electron compensation is energetically unfavoured, suggesting that conduction must occur as a result of oxygen vacancies. For *h*-$BaTiO_3$, the preference of O1 face-sharing vacancies over O2 corner-sharing vacancies and an energetic penalty for Ba-site doping (when compared to *c*-$BaTiO_3$) has been confirmed.

The phase stabilisation of *h*-$BaTiO_3$ and the energetic consequences of transition metal doping have been established. Through combined solution and binding energies, an accurate picture of energetically preferred dopant ions, valency states and defect sites is observed. Results show that doping at the Ti2 sites in face-sharing dimers with O1 face-sharing vacancy compensation in *h*-$BaTiO_3$ is preferred for all dopant ions and is significantly energetically more favourable than doping in the cubic polymorph. In the case of tri and tetravalent ions, the solution energies for this incorporation are negative which suggests preferential stabilisation of the hexagonal polymorph, consistent with experimental studies for samples prepared in air. Incorporation of higher charged dopant ions (e.g. 4+) were found to be favoured over lower charged ions (e.g. 2+). This is consistent with samples prepared in air where Mn^{4+} and mixed Co^{3+}/Co^{4+} ions have been established from a combination of Neutron Diffraction studies combined with magnetic susceptibly measurements, Electron Energy Loss Spectroscopy and X-ray Absorption Near Edge Structure studies [11, 59]. It is noteworthy that it is possible to

stabilise Mn^{3+} and Co^{2+}/Co^{3+} ions in *h*-$BaTiO_3$ by processing in inert and reducing conditions, respectively [11, 59] to promote oxygen-loss. Oxidation of Ni^{2+} to Ni^{3+} is lower in energy compared to incorporation for the cubic polymorph and for the hexagonal polymorph when O1 vacancies are present, whereas oxidation of Fe^{3+} was found to be very unfavourable; both these findings are also supported by experiment.

The results of such calculations have provided an extensive description of the aliovalent doping of $BaTiO_3$ and have succeeded in both the confirmation of experimental observations and in providing an understanding into these defect processes.

References

[1] S. Guillemet-Fritsch, Z. Valdez-Nava, C. Tenailleau, T. Lebey, B. Durand and J. Chane-Ching, Advanced Materials **20**, 551 (2008).

[2] G. H. Jonker, Solid-State Electronics **7**, 895 (1964).

[3] F. D. Morrison, D. C. Sinclair and A. R. West, Journal of Applied Physics **86**, 6355 (1999).

[4] D. F. K. Hennings, B. Schreinemacher and H. Schreinemacher, Journal of the European Ceramic Society **13**, 81 (1994).

[5] F. D. Morrison, A. M. Coats, D. C. Sinclair and A.R West, Journal of Electro-ceramics **6**, 219 (2001).

[6] H. Natsui, J. Yu, A. Masuno, M. Itoh, O. Odawara and S. Yoda, Ferroelectrics **378**, 195 (2009).

[7] D. W. Hahn and Y. H. Han, Japanese Journal of Applied Physics **48**, 111406 (2009).

[8] Y. Tsur, T. D. Dunbar and C. A. Randall, Journal of Electro-ceramics **7**, 25 (2001).

[9] G. M. Keith, M. J. Rampling, K. Sarma, N. Mc. Alford and D. C. Sinclair, Journal of the European Ceramic Society **24**, 1721 (2004).

[10] G. M. Keith, K. Sarma, N. Mc. Alford and D. C. Sinclair, Journal of Electro-ceramics **13**, 305 (2004).

[11] L. Miranda, A. Feteira, D. C. Sinclair, K. Boulahya, M. Hernando, J. Ramfrez, A. Varela, J. M. Gonzalez-Calbet and M. Parras, Chemistry of Materials **21**, 1731 (2009).

[12] I. E. Grey, C. Li, L. M. D. Cranswich, R. S. Roth, T. A. Vanderah, Journal of Solid State Chemistry **135**, 312 (1998).

[13] H. J. Hagemann and H. Ihrig, Physical Review B **20**, 3871 (1979).

[14] R. M. Glaister and H. F. Kay, Proceedings of the Physical Society **76**, 763 (1960).

[15] H. Natsui, C. Moriyoshi, F. Yoshida, Y. Kuroiwa, T. Ishii, O. Odawara, J. Yu and S. Yoda, Applied Physics Letters **98**, 132909 (2011).

[16] H. T. Langhammer, T. Muller, A. Polity, K. -H. Felgner, H. -P. Abicht, Materials Letters **26**, 205 (1996).

[17] S. Jayanthi and T. R. N. Kutty, Journal of Materials Science: Materials in Electronics **19**, 615 (2008).

[18] J. G. Dickson, L. Katz and R. Ward, Journal of the American Chemical Society **83**, 3026 (1961).

[19] N. Maso, H. Beltran, E. Cordoncillo, P. Escribano and A. R. West, Journal of Materials Chemistry **16**, 1626 (2006).

[20] R. Bottcher, H. T. Langhammer and T. Muller, Journal of Physics: Condensed Matter **23**, 115903 (2011).

[21] Y. Li, Q. Liu, T. Yao, Z. Pan, Z. Sun, Y. Jiang, H. Zhang, Z. Pan, W. Yan and S. Wei, Applied Physics Letters **96**, 091905 (2010).

[22] D. Makovec, Z. Samardzija and M. Drofenik, Journal of the American Ceramic Society **87**, 1324 (2004).

[23] Y. Mizuno, H. Kishi, K. Ohnuma, T. Ishikawa and H. Ohsato, Journal of the European Ceramic Society **27**, 4017 (2007).

[24] N. A. Benedek, A. L. S. Chua, C. Elsaesser, A. P. Sutton and M. W. Finnis, Physical Review B **78**, 064110 (2008).

[25] G. C. Mather, M. S. Islam and F. M. Figueiredo, Advanced Functional Materials **17**, 905 (2007).

[26] G. Lewis and C. R. A. Catlow, Journal of Physics C: Solid State Physics **18**, 1149 (1985).

[27] M. Buscaglia, V. Buscaglia, M. Viviani and P. Nanni, Journal of the American Ceramic Society **84**, 376 (2001).

[28] H. Moriwake, C. A. J. Fisher and A. Kuwabara, Japanese Journal of Applied Physics **48**, 09KC03 (2009).

[29] H. Moriwake, C. A. J. Fisher, A. Kuwabara, Japanese Journal of Applied Physics **49**, 09MC01 (2010).

[30] C. L. Freeman, J. A. Dawson, H. Chen, J. H. Harding, L. -B. Ben and D. C. Sinclair, Journal of Materials Chemistry **21**, 4861 (2011).

[31] S. Piskunov, E. Kotomin, E. Heifets, J. Maier, R. Eglitis and G. Borstel, Surface Science **575**, 75 (2005).

[32] M. J. Akhtar, Z. -U. -N. Nisa, R. A. Jackson and C. R. A. Catlow, Journal of the American Ceramic Society **78**, 421 (1995).

[33] R. Wycoff, *Crystal Structures* (John Wiley and Sons Ltd., New York, 1965).

[34] M. Cherry, M. S. Islam and C. R. A. Catlow, Journal of Solid State Chemistry **118**, 125 (1995).

[35] J. Gale and A. Rohl, Molecular Simulation **29**, 291 (2003).

[36] D. Lide, *CRC Handbook of Chemistry and Physics* (CRC Press, Boca Raton, 1998).

[37] A. R. West, *Basic Solid State Chemistry* (John Willy and Sons Ltd., Chichester, 1999).

[38] M. K. Karapet'yants and M. L. Karapel'yants, *Thermodynamic Constants of Inorganic and Organic Compounds* (Ann Arbor-Humphrey Science Publishers, Michigan, 1970).

[39] M. W. Chase, *NIST-JANAF Thermochemical Tables* (American Chemical Society; American Institute of Physics for the National Institute of Standards and Technology, Woodbury, 1971).

[40] H. Beltran, E. Cordoncillo, P. Escribano, D. C. Sinclair and A. R. West, Journal of the American Ceramic Society **87**, 2132 (2004).

[41] F. Morrison, D. C. Sinclair and A. R. West, Journal of the American Ceramic Society **84**, 474 (2001).

[42] L. Xue, Y. Chen and R. Brook, Materials Science and Engineering B Solid State Materials for Advanced Technology **1**, 193 (1998).

[43] G. Kresse and J. Furthmüller, Computational Materials Science **6**, 15 (1996).

[44] D. M. Ceperley and B. J. Alder, Physical Review Letters **45**, 566 (1980).

[45] J. P. Perdew and A. Zunger, Physical Review B **23**, 5048 (1981).

[46] P. E. Blöchl, Physical Review B **50**, 17953 (1994).

[47] G. Kresse and D. Joubert, Physical Review B **59**, 1758 (1999).

[48] R. F. W. Bader, *Atoms in Molecules: A Quantum Theory* (Oxford University Press, Oxford, 1990).

[49] C. L. Freeman, J. A. Dawson, H. Chen, L. - B. Ben, J. H. Harding, A. R. West and D. C. Sinclair, Advanced Functional Materials (accepted) (2012).

[50] D. C. Sinclair, J. M. S. Skakle, F. D. Morrison, R. I. Smith and T. P. Beales, Journal of Materials Chemistry **6**, 1327 (1999).

[51] A. Feteira, G. M. Keith, M. J. Rampling, C. A. Kirk, I. M. Reaney, K. Sarma, N. Mc. Alford and D. C. Sinclair, Crystal Engineering **5**, 439 (2002).

[52] T. A. Colson, M. J. S. Spencer and I. Yarovsky, Computational Materials Science **34**, 157 (2005).

[53] J. A. Dawson, C. L. Freeman, L. -B. Ben, J. H. Harding and D. C. Sinclair, Journal of Applied Physics **109**, 084102, (2011).

[54] L. -B. Ben, *Structure-Composition-Property Relationships of RE Doped $BaTiO_3$ Ceramics* (University of Sheffield, PhD Thesis, 2010).

[55] N. Hirose, J. M. S. Skakle and A. R. West, Journal of Electro-ceramics **3**, 233 (1999).

[56] W. L. Masterton, E. J. Slowinski and C. L. Stanitski, *Chemical Principles* (CBS College Publishing, San Francisco, 1983).

[57] J. M. Tarascon, G. Vaughan, Y. Chabre, L. Seguin, M. Anne, P. Strobel and G. Amatucci, Journal of Solid State Chemistry **147**, 410 (1999).

[58] I. E. Grey, C. Li, L. M. D. Cranswick, R. S. Roth and T. A. Vanderah, Journal of Solid State Chemistry **135**, 312 (1998).

[59] L. Miranda, K. Boulahya, M. Hernando, D. C. Sinclair, F. Jimenez-Villacorta, A. Varela, J.M. Gonzalez-Calbet, and M. Parras, Chemistry of Materials **23**, 1050 (2011).

5

Energetics and Local Strain in $BaTiO_3$ Solid Solutions

5.1 Introduction

The ability for the ABO_3 perovskite structure of compounds such as $BaTiO_3$, $SrTiO_3$ and $CaTiO_3$ to accept isovalent dopants on both the A- and B-sites is crucial in manipulating the electrical properties. While B-site doping of $BaTiO_3$ can have a dramatic effect on both the permittivity and the phase transition temperatures of the compound [1-3], A-site doping is often used to alter the ferroelectric Curie temperature (T_c) in addition to other phase transition temperatures such as the tetragonal to orthorhombic transition [4-6]. Common A-site isovalent dopants for these materials include alkaline earth metals such as Ca^{2+}, Ba^{2+} and Sr^{2+} or similarly sized post-transition metals e.g. Pb^{2+}.

As a result of the importance of the electrical properties of these materials which include ferroelectricity and high intrinsic permittivity [7-10], there has been a significant amount of research on both the undoped compounds and mixed compounds over the full solid solution range. For the $Ba_{1-x}Sr_xTiO_3$ mix (BST) complete solubility exists and T_c decreases with increasing Sr^{2+} concentration as the smaller ion effectively stabilises the cubic phase [11]. The solid solution limit for the $Ba_{1-x}Ca_xTiO_3$ system (BCT) is only 24 mol% due to the increased size mismatch between the two A-site cations [6]. Furthermore, an unusual T_c effect is observed for this mixed compound; T_c rises from 403K for undoped $BaTiO_3$ to 410K for 8 mol% Ca concentration and then decreases up to the solid solution limit [6, 11]. This anomaly cannot be explained by a simple cation size effect as for the Sr-doped compound. Sinclair and Attfield attribute the initial increase in T_c to a strain effect associated with size mismatch of Ca and Ba on the A-site, whereas the decrease in T_c for compositions with $x > 8$ mol% Ca is attributed

to a size effect [11]. There is less information in the literature on Ba-doped $CaTiO_3$ (CBT) solid solution; however, a solubility limit of 14 mol% has been obtained for the addition of Ba to orthorhombic $CaTiO_3$ and full phase equilibria studies of the $BaTiO_3$-$CaTiO_3$ system have been reported [12-13]. Beyond the two solubility limits for BCT and CBT there exists a phase mixture of tetragonal BCT and orthorhombic CBT. Figure 5.1 shows the solid solution limits for the $BaTiO_3$-$CaTiO_3$ system as well as the two-phase region beyond these solid solution limits. At low concentrations of Ca (x < 5 mol%) there is a small increase in the unit cell volume i.e. the volume of mixing is positive. This is contrary to simple size arguments, where the smaller Ca ion causes a reduction in volume and further suggests that strain has an influence on this solid solution at low Ca concentrations.

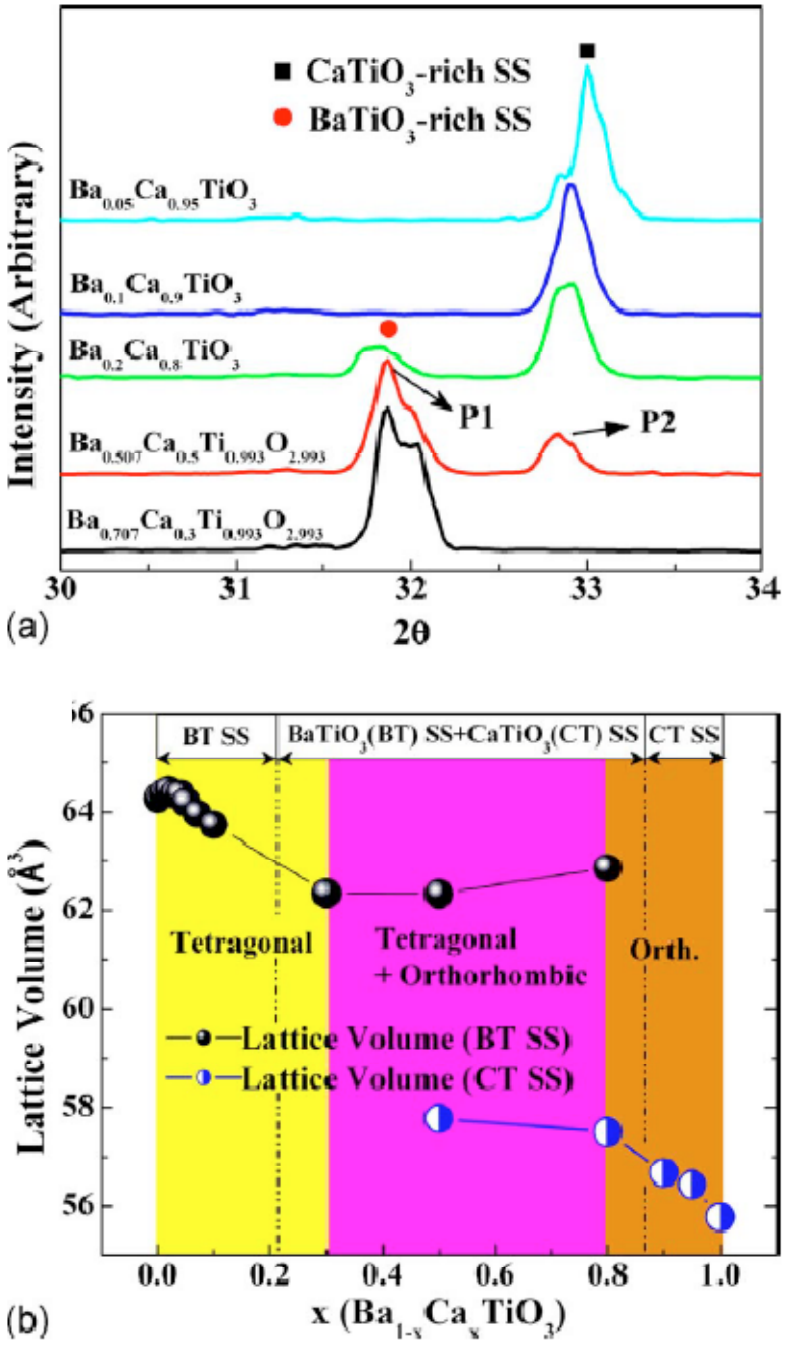

Figure 5.1: (a) XRD patterns of x = 0.3-0.95 $Ba_{1-x}Ca_xTiO_3$ (b) XRD results showing the variation of lattice volume with Ca concentration, solid solution limits are denoted by dashed lines [12] (explicit permission to reuse this image has been granted).

In addition to the well studied phase transition temperatures of these materials, there also exists an abundance of other work on their various electrical properties. The dielectric properties of $Ba_{1-x}Sr_xTiO_3$ are one such example and are crucial in many of its technological applications such as high dielectric capacitors and PTC thermistors [14-15]. The permittivity at T_c of $Ba_{1-x}Sr_xTiO_3$ varies with Sr^{2+} concentration and a peak value is achieved at 60 mol% Sr^{2+} [16]. In addition to Sr^{2+} concentration, the sintering temperature has also been shown to have a significant effect on the dielectric properties of $Ba_{1-x}Sr_xTiO_3$ and at the Curie point the peak permittivity was dependent on both the $SrTiO_3$ concentration and the average grain size [17]. BCT has also received a considerable amount of interest due to its use in electrical applications such as capacitors [18-19] and as a photo-refractive material [20-21]. One of the first thorough studies into the dielectric properties of this mix was completed by Mitsui and Westphal [6] who recorded permittivity over a range of temperatures and Ca^{2+} concentrations. The effects of Ca^{2+} addition on the phase transition temperatures of $BaTiO_3$ including an almost constant value of T_c up to the solid solution limit were also reported. A more recent study concludes that Ca-doping reduces the permittivity of $BaTiO_3$ single crystals and that increasing the frequency for a given Ca^{2+} concentration further reduces permittivity [22]. It is noteworthy that considerable effort has also gone into studying the effects of Ca-doped $BaTiO_3$ at the B-site (BTC) and its applications in electronic devices [5, 23-24].

Given the significant amount of attention devoted to these materials experimentally, it is somewhat surprising that there is not also a large body of computational studies. The majority of work completed has been done using molecular dynamics with the focus on the BST mixture. Two such papers make use of molecular dynamics to model the structure and electrical properties; Tanaka *et al.* [25] report a peak permittivity at Sr^{2+} 30 mol% as a result of Ti^{4+} ion displacement, whereas Tinte *et al.* [26] reproduce the phase behaviour of the solution as well as its constituent compounds and relates the ferroelectric behaviour of the solid solution to its cell volume. To the best of our knowledge there is no potential-based or electronic structure simulation work on the $BaTiO_3$-$CaTiO_3$ system. There are, however, in addition to results presented in chapter

4, lattice statics simulations of point defects in the pure compounds that can provide an insight into the energetics of doping at infinitely dilute concentrations [10, 27].

In this chapter, we use lattice statics methods to compare two sets of interatomic potentials in exploring the energies of mixing and structures of three sets of solid solutions, namely BST, BCT and CBT. Using the new $BaTiO_3$ potential set in conjunction with new Sr-O and Ca-O interatomic potentials, the local strain in BCT is investigated and its effects on ferroelectric performance assessed.

5.2 Method

5.2.1 Potential Models

Two sets of interatomic potentials and shell model values are used in calculating the energies of mixing curves. The first potential set combines the Ba-O, Ti-O and O-O potentials of Lewis and Catlow [27] developed in 1985 with the Sr-O potential of Akhtar *et al.* [28] and the Ca-O potential of Mather *et al.* [10]. These references also illustrate the use of these potentials in modelling the respective titanates. All these potentials take the Buckingham form and a cutoff of 10 Å was applied to all of these potentials. The second potential set is our $BaTiO_3$ potential set (described in chapter 4) with newly fitted Sr-O and Ca-O interatomic potentials (table 5.1). The Sr-O and Ca-O interatomic potentials were fitted to both the lattice energies and lattice parameters of their respective oxide and titanate (tables 5.2 and 5.3). A cutoff of 12 Å was applied to our potential set.

Buckingham Potentials			
Interaction	A (eV)	ρ (Å)	C (eV Å^{-6})
Sr^{2+} - O^{2-}	1250.0	0.3540	19.22
Ca^{2+} - O^{2-}	1375.0	0.3325	15.21

Shell Model		
Species	Shell Charge	k (eV Å^{-2})
Sr^{2+}	- 1.45	112.46
Ca^{2-}	- 1.45	150.00

Table 5.1: Sr-O and Ca-O potential and shell model parameters.

Lattice Energy of Formula Unit (eV)			
Crystal	Experiment	Lewis/Akhtar/Mather [10, 27, 28]	This Work
BaO	- 31.90	- 34.57	- 32.58
SrO	- 33.40	- 36.33	- 34.47
CaO	- 35.25	- 37.70	- 36.58
c-$BaTiO_3$	- 159.86	- 148.02	- 160.02
c-$SrTiO_3$	- 161.29	- 149.25	- 162.25
o-$CaTiO_3$	- 162.55	- 150.88	- 164.44

Table 5.2: Lattice energies of BaO, SrO, CaO, *c*-$BaTiO_3$, *c*-$SrTiO_3$ and *o*-$CaTiO_3$. Energies for BaO and *c*-$BaTiO_3$ are reproduced from chapter 4.

Table 5.2 shows the lattice energies of each crystal structure which have been calculated using Born-Haber cycles. The values for this cycle can be found in the literature [29-33]. It is clear that our potential set is far more accurate in calculating the

lattice energies of both the titanates and its respective binary oxide. Similarly, for the lattice parameters of the basic oxide materials, the new potential set replicates the experimental cell parameters most accurately. For the three titanate materials both potential sets accurately reproduce the experimental cell parameters. Such reliability is necessary when attempting to calculate the structural effects of mixing the compounds.

Cell Parameters (Å)			
Crystal	Experiment	Lewis/Akhtar/Mather [10, 27, 28]	This Work
BaO	a = 5.54 [34]	a = 5.02	a = 5.33
SrO	a = 5.16 [35]	a = 4.71	a = 5.04
CaO	a = 4.80 [35]	a = 4.60	a = 4.75
c-$BaTiO_3$	a = 4.00 [34]	a = 3.96	a = 4.01
c-$SrTiO_3$	a = 3.91 [36]	a = 3.90	a = 3.96
o-$CaTiO_3$	a = 5.38 [37] b = 5.44 c = 7.64	a = 5.39 b = 5.45 c = 7.68	a = 5.49 b = 5.44 c = 7.74

Table 5.3: Unit cell lengths of BaO, SrO, CaO, c-$BaTiO_3$, c-$SrTiO_3$ and o-$CaTiO_3$. Unit cell lengths for BaO and c-$BaTiO_3$ are reproduced from chapter 4.

5.2.2 Thermodynamics of Mixing

A solid solution can exist in any given number of configurations, however only the low energy configurations (local minima, K) will contribute to the thermodynamic properties of the system. By finding and averaging the energies of these configurations, the full thermodynamic properties of the solid solution can be found [38]. The configurations at local minima can be found by optimising the atomic positions of the atoms in the crystal. This can be expressed mathematically:

$$H = \frac{\sum_{k}^{K} H_k \exp(-G_k / k_B T)}{\sum_{k}^{K} \exp(-G_k / k_B T)} \tag{5.1}$$

$$G = -k_B T \ln \sum_{k}^{K} \exp(-G_k / k_B T) \tag{5.2}$$

where k_B is the Boltzmann constant, H_k, is the enthalpy of configuration k, and G_k is the Gibbs energy of configuration k. Given the size of the simulation cell it is impossible to calculate the energies of all K configurations. Therefore, the equation for the Gibbs free energy must be rewritten (equation (5.3)) to allow the calculation to be done for a selection of configurations, K'. Equation (5.3) is split into two terms; the first represents the ideal calculation (i.e. where all the configurations are sampled) and the second term represents the necessary correction to the ideal term. With an appropriate choice for the value for K', the thermodynamic properties can be converged to the required level of accuracy.

$$G = -k_B T \ln K - k_B T \ln \left(\frac{\sum_{k}^{K'} \exp(-G_k / k_B T)}{K'} \right) \tag{5.3}$$

In this work, we consider only the *energies* of mixing (i.e. the internal energies of the configurations are used as an approximation for the enthalpies). The calculations have been performed in the static limit as described in chapter 2. This means the configurational energies are independent of temperature and the vibrational contribution to the entropy is also neglected. These approximations are justified by the fact that the main aim of this chapter is to explore the strain relationships in these solid solutions and that the energies of mixing are mainly used as a test of whether they are capable of reproducing the general trends observed experimentally.

The energy of mixing is defined by a general formula:

$$\Delta E_{mix} = E_{sol} - (xE_1 + (1-x)E_2) \tag{5.4}$$

where ΔE_{mix} is the energy of mixing, E_{sol} is the lattice energy of the solid solution, E_1 and E_2 are the lattice energies of the pure compounds and x is the mole fraction of component 1 and is dependent on the A-site ion concentrations in the mixed compound.

Although no energy of mixing curves have been calculated for these titanate solid solutions, energy of mixing curves have been calculated for other oxide materials [39-40]. Energy of mixing curves were calculated over the full concentration range for the BST solution and up to the single phase limits of $x = 0.3$ and $x = 0.2$ for BCT and CBT, respectively. Supercells of 5 x 5 x 5 (625 atoms) were used for the BST and BCT solid solutions and 3 x 3 x 3 (540 atoms) for the CBT solid solutions. Configurations were constructed using a random number generator. The atomic coordinates of each A-site ion was assigned a random number and then sorted numerically to produce hundreds of individual configurations. The lowest energy state found for each concentration was used for the plotting of the curves; it is noteworthy that although hundreds of random configurations were simulated the energetic difference between the vast majority of configurations was surprisingly small (~0.05 eV for BST and ~0.2 eV for BCT and CBT).

Ideally, a tetragonal $BaTiO_3$ structure should have been used for simulating the BST and BCT solid solutions to correspond with the experiment [11]. Unfortunately due to the small difference between lattice parameters (c/a = 1.01 [41]) in the tetragonal structure and the favouring of Coulombic interactions over small dipole interactions by classical energy minimisation, the starting tetragonal structure optimises to the cubic structure. The difficulty in reproducing the tetragonal structure means that the cubic $BaTiO_3$ structure has been used in these calculations. These phases are structurally similar and the local relaxations caused by defects are also likely to be the similar or even the same. As the focus of this chapter is to investigate the structural effects and not to conduct property measurements (e.g. Curie temperature), it is therefore reasonable to suggest this is not a major issue. GULP [42] has again been used to perform all lattice statics calculations.

5.3 Energy of Mixing Curves

5.3.1 $Ba_{1-x}Sr_xTiO_3$ (BST) Solid Solutions

The energy of mixing curves for BST using both potential sets are presented in figure 5.2. The first thing that should be noted is the minute variation of ΔE_{mix} over the entire solid solution range. The maximum values of ΔE_{mix} are 0.006 eV (0.58 kJ mol^{-1}) obtained at ~ 48 % Sr content for the Catlow/Akhtar (CA) potential set and 0.0056 eV (0.54 kJ mol^{-1}) at ~ 58 % Sr content for the new potential set. Both these energy barriers can be overcome easily at room temperature (corresponds to 0.0025 eV). This corresponds well with experimental findings that complete solubility occurs in this system [11, 43]. Such low energies also suggest that the Ti-O interaction is by far the most dominant interaction in the system as the formation of the solid solution only has a small effect on the energetics in comparison with the pure end members. The CA energy curve is almost symmetrical, suggesting that both Ba addition to *c*-$SrTiO_3$ and Sr addition to *c*-$BaTiO_3$ require similar amounts of energy. The other potential set, however, produces a very different curve for low Sr concentrations. Negative energy values are found for concentrations of less than 15 % Sr which suggests some form of stabilisation at these concentrations, however given the very small energy gain (~ -0.001 eV) it is doubtful whether this could be verified by experiment. Point defect calculations also support this finding as shown in table 5.4.

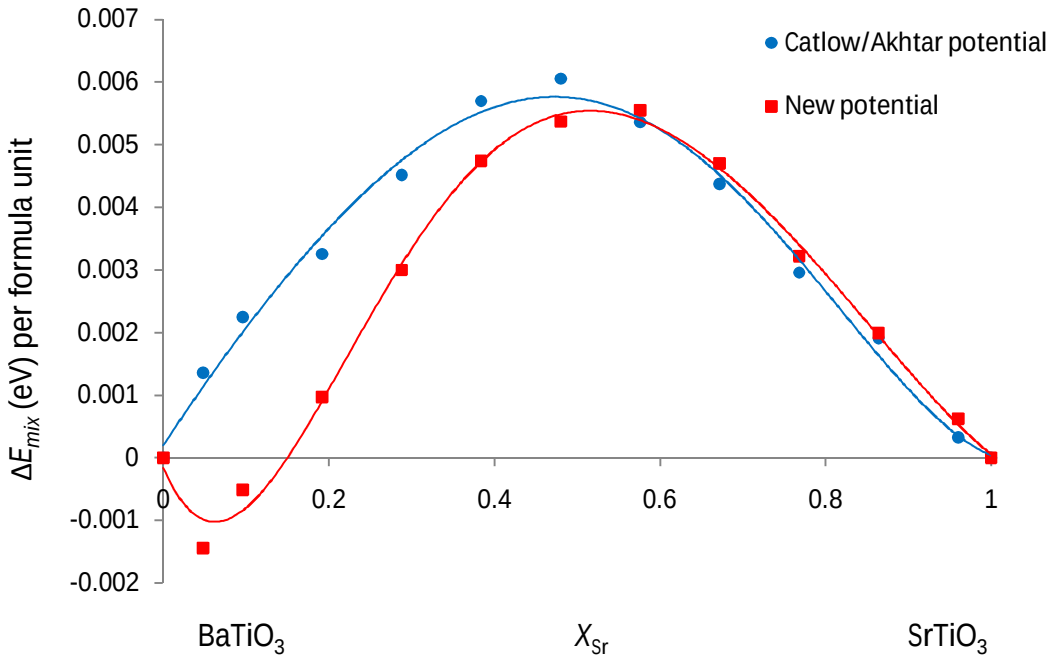

Figure 5.2: Calculated energy of mixing curves for $Ba_{1-x}Sr_xTiO_3$ (BST) using Eqn. 5.4 and both potential sets.

A-site defect	CA potential set (eV)	New potential set (eV)
Sr defect in *c*-$BaTiO_3$	- 1.17	- 2.21
Ba defect in *c*-$SrTiO_3$	1.24	2.24

Table 5.4: Point defect energies of Sr-doping of *c*-$BaTiO_3$ and Ba-doping of *c*-$SrTiO_3$.

From the point defect energies and the lattice energies of the binary oxides it is clear that at the infinitely dilute concentration, incorporation of Sr at a Ba-site in *c*-$BaTiO_3$ is preferred with the new potential set, whereas the opposite is true for Ba incorporation of *c*-$SrTiO_3$. A possible suggestion as for why the CA potential set does not show this effect can be found in the strength of the Sr-O interatomic potential used. Table 5.2 clearly shows a significant 2.93 eV discrepancy between the experimental and

calculated lattice energies (using the Akhtar *et al.* [28] Sr-O potential) of SrO. Therefore as a result of the potential overestimating the Sr-O interaction, the lattice contracts with higher Sr concentrations and an increased 'shrinking' effect on the supercell volume is observed, as illustrated by figures 5.3 and 5.4.

Using the ordered solid solutions as an illustration, the small increase in contraction of the supercell as a result of the Akhtar Sr-O potential is apparent. The total volume contraction for the ordered supercell using the CA potential set is 363.48 $Å^3$ compared to 264.67 $Å^3$ when using the FT potential set. A similar pattern is observed for Ti-O interatomic distances (figure 5.4) at low Sr concentrations. In pure $BaTiO_3$, the difference between the Ti-O interatomic distances is 0.023 Å using the two potential sets, whereas at X_{Sr} = 0.19 the difference between the shortest distances is 0.055 Å. While these values are small, it may explain why such a subtle effect is observed in the energy of mixing curve calculated using the new potential, but not in the CA curve.

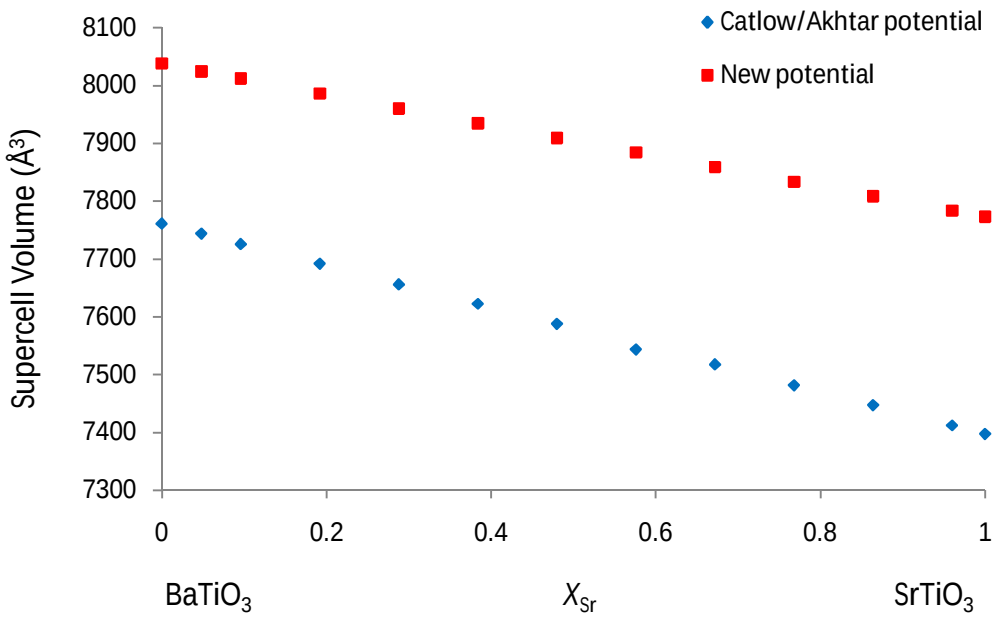

Figure 5.3: Supercell volume plotted against Sr concentration for the most ordered solid solution configuration (i.e. segregation of Sr and Ba ions).

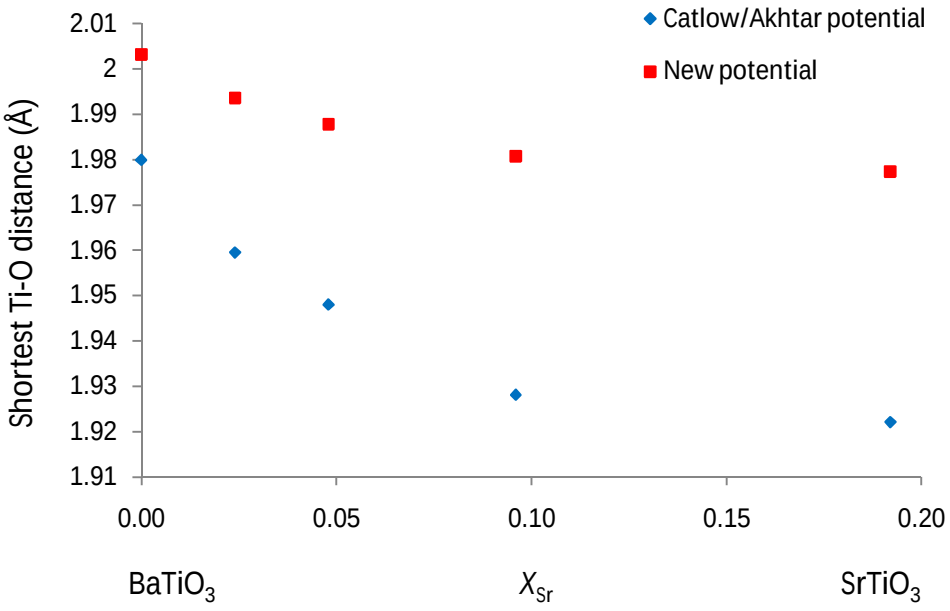

Figure 5.4: Shortest Ti-O interatomic distances plotted against Sr concentration (up to for the most ordered solid solution configuration (i.e. segregation of Sr and Ba ions).

5.3.2 $Ba_{1-x}Ca_xTiO_3$ (BCT) Solid Solutions

The $BaTiO_3$-$CaTiO_3$ system consists of tetragonal BCT and orthorhombic CBT solid solutions with a phase mixture existing between these two phases. The energy of mixing curve for BCT is plotted up to the solid single-phase limit (x = 0.3) in figure 5.5. At concentrations under X_{Ca} = 0.15, there is little variation between the two potentials, whereas at higher concentrations the deviation becomes more apparent although still only of the order of around 0.02 eV. All energy values are positive suggesting that there is no significant stabilisation of the system at particular concentrations, unlike BST with the new potential set. The magnitude of the energies is also far greater than was observed for the BST system. This is to be expected due to increased charge density of the Ca^{2+} ions and the increased size mismatch between Ca^{2+} (1.00 Å) and Ba^{2+} (1.35 Å) compared to Sr^{2+} (1.18 Å) and Ba^{2+} (1.35 Å)[46]. At the solid solution limit (X_{Ca} = 0.24) energies of ~0.08 eV (7.72 kJ mol^{-1}) for the Catlow/Mather (CM) potential set and ~0.09 eV (8.68 kJ mol^{-1}) for the new potential set are obtained. These energy barriers

are clearly more significant than for the BST solid solution suggesting full solubility does not exist in this system, in agreement with experimental results [12].

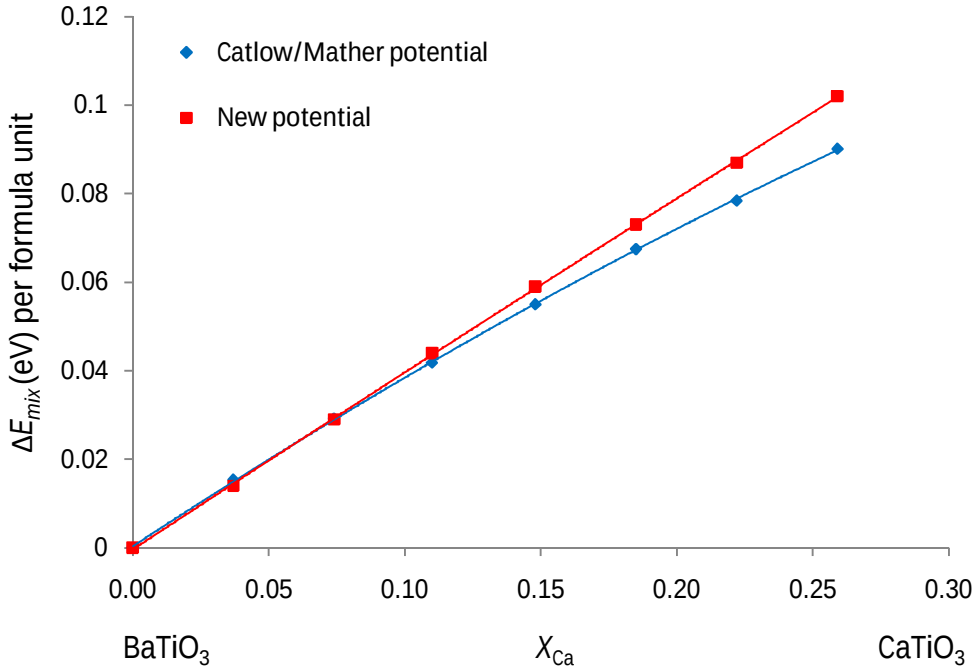

Figure 5.5: Calculated energy of mixing curves for $Ba_{1-x}Ca_xTiO_3$ (BCT) using Eqn. 5.4 and both potential sets.

As previously discussed, an unusual feature of this series is the almost constant T_c with the addition of Ca to $BaTiO_3$ in comparison to the linear decrease of T_c with the addition of Sr to $BaTiO_3$ [11]. It is thought that this is a feature of Ti-O strain created from Ca addition meaning that the ferroelectric phase is stabilised at higher temperatures. Ti-O interatomic distances for this system were measured at various Ca concentrations and are displayed in figure 5.6, when compared to the same data for the BST system; there is unfortunately no significant difference other than the increased contraction of the Ti-O distance as a result of inserting Ca as opposed to Sr. Experimentally it is observed that low concentrations of Ca cause a small increase in the

lattice volume of BCT [12]. This was tested by plotting supercell volume against Ca concentration as shown in figure 5.7. Similarly to the results for Ti-O distances, no unusual trends were observed and the increase in cell volume was not present. It is suspected that the increase in the Coulombic interaction from adding the smaller Ca ions is a far stronger effect compared to the subtle strain effect that causes the small increase in the volume of the system and therefore only a system volume decrease is observed.

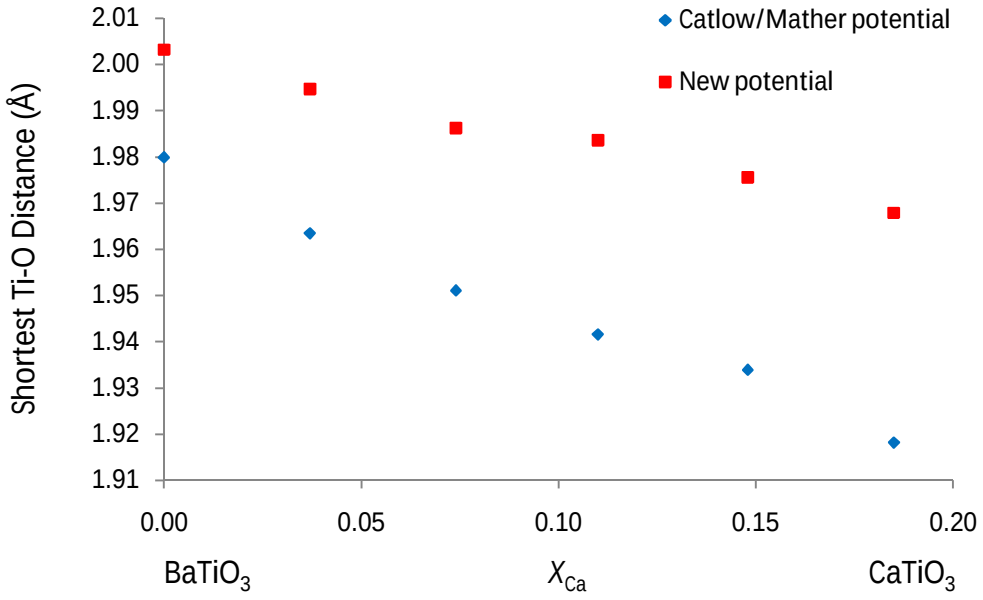

Figure 5.6: Shortest Ti-O interatomic distance (Å) plotted against Ca concentration (up to $X_{Ca} = 0.2$).

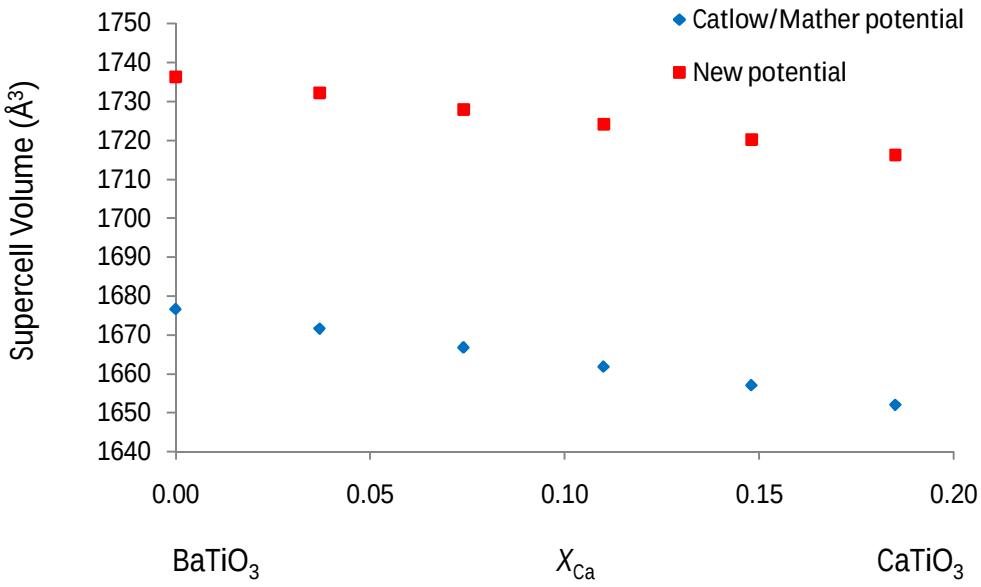

Figure 5.7: Supercell volume (Å^3) plotted against Ca concentration (up to X_{Ca} = 0.2).

5.3.3 $Ca_{1-x}Ba_xTiO_3$ (CBT) Solid Solutions

To simulate the full $BaTiO_3$-$CaTiO_3$ system, the solid solution formed at the end of the composition range of BCT must be considered so that a full energy of mixing diagram can be produced. Figure 5.8 shows the energy of mixing for the CBT solid solution, again up to the solubility limit (x = 0.14). This plot shows a significant variation over the Ba concentration for the two potentials. The new potential set suggests that Ba incorporation into the *o*-$CaTiO_3$ structure requires considerably more energy compared to the CM potential set, this energetic difference also increases with increasing Ba concentration. The ΔE_{mix} value at the solubility limit using the CM potential set is ~0.06 eV (5.79 kJmol^{-1}) per formula unit in comparison to a value of ~0.09 eV (8.68 kJmol^{-1}) per formula unit. It is likely that the smaller difference in lattice energies between $BaTiO_3$ and $CaTiO_3$ using the CM potentials (2.55 eV) compared to the larger difference using the new potential set (4.06 eV) is responsible for the lower energies of mixing observed in figure 5.9. A smaller energy difference between the end member compounds means that mixing can occur without such a high energy penalty, unlike for

the energy of mixing curve calculated using the new potential set. Through the combination of the BCT and CBT energy of mixing curves, the full single-phase $BaTiO_3$-$CaTiO_3$ system can be examined.

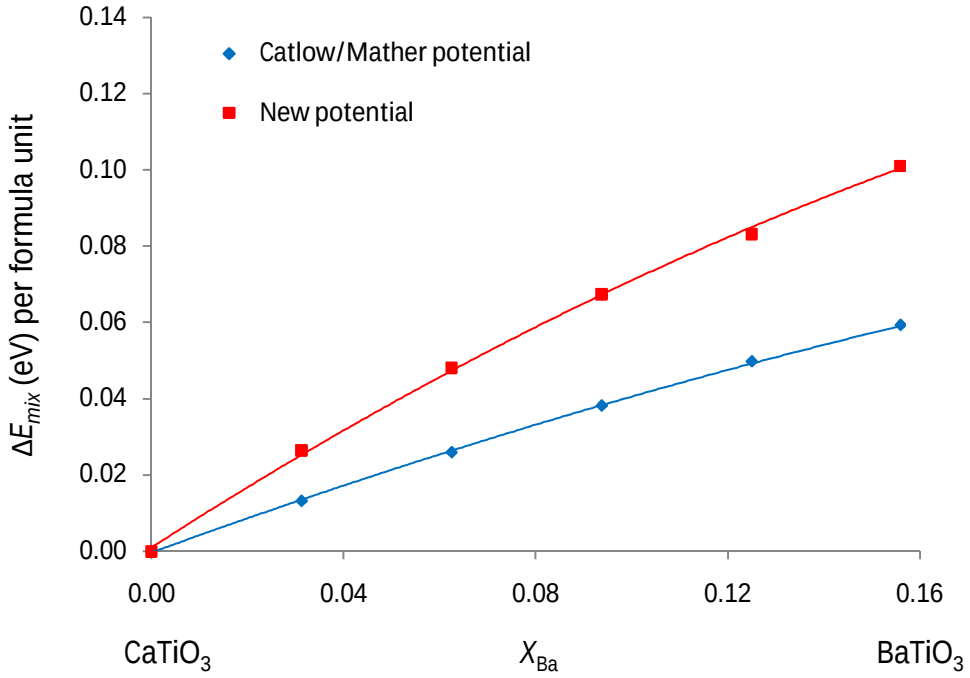

Figure 5.8: Calculated energy of mixing curves for $Ca_{1-x}Ba_xTiO_3$ using Eqn. 5.4 and both potential sets.

5.3.4 The Overall $BaTiO_3$-$CaTiO_3$ Solid Solution System

The overall energy of mixing plot for the $BaTiO_3$-$CaTiO_3$ solid solution system produced from combining figures 5.5 and 5.8 is given in figure 5.9 where the mixed phase region [12] has been excluded. The most important feature of this diagram is the energy of mixing at the solid solution limits. Using the new potential set, the energies at these limits is very similar (0.09 eV for BCT and 0.09 eV for CBT) whereas for the CM potential set the energy difference is more significant (0.08 eV for BCT and 0.06 eV for CBT). The fact that these energy differences are small proves the reliability of both of

these potential sets in modelling such solid solutions. This is especially true for the FT set as the energies are almost identical and excellent comparison with experimental work is achieved as the same amount of energy is required to introduce the maximum amount of Ca and Ba into $BaTiO_3$ and $CaTiO_3$, respectively. With regards to the CA potential set, equivalent energies are observed at similar dopant ion concentrations e.g. if we extrapolate the CBT (right hand side) curve in figure 5.9 to X_{Ca} = 0.76, an energy of ~0.08 eV is obtained which is equivalent to the energy obtained at the same concentration of Ca in BCT (X_{Ba} = 0.24, ΔE_{mix} = 0.08 eV). This element of symmetry in the CA potential energy curves suggests that the same amount of energy is required to incorporate a specific concentration of Ca into $BaTiO_3$ as well as the same concentration of Ba into $CaTiO_3$. As discussed, this is contrary to experiment where the solid solution limits are different for the BCT and CBT mixes [11, 12].

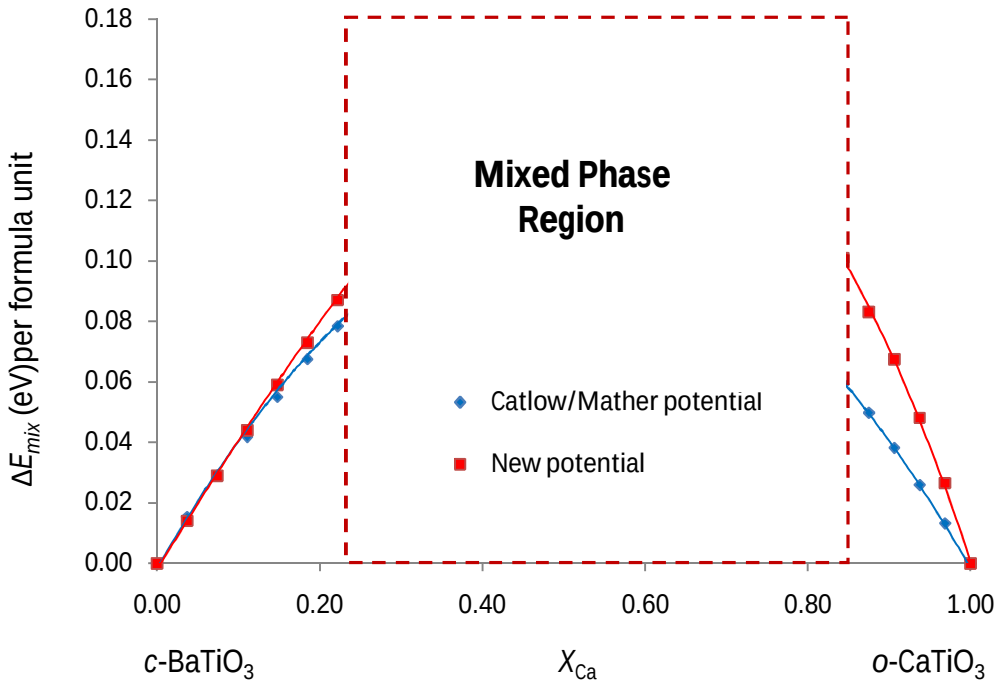

Figure 5.9: Calculated energy of mixing curves for $BaTiO_3$-$CaTiO_3$ system using both potential sets. The left and right boundaries of the phase mixture denote the solid solution limits according to experimental data [11, 12].

5.4 Local Disorder in the $Ba_{1-x}Ca_xTiO_3$ System

5.4.1 Ba-O, Ca-O and Ti-O Interatomic Distances

As discussed in the introduction, $Ba_{1-x}Ca_xTiO_3$ (BCT) exhibits an unusual T_c effect whereby T_c rises from 403 K for undoped $BaTiO_3$ to 410 K for 8 mol% Ca concentration and then decreases up to the solid solution limit. It has been proposed that this is a strain effect. Calculations on 7 x 7 x 7 (1715 atoms) supercells were used to investigate the effect on Ba-O, Ca-O and Ti-O interatomic distances from increasing Ca concentration. Figure 5.10 shows the average smallest and largest Ba-O/Ca-O distances calculated from around 30 of the lowest energy configurations and figure 5.11 gives the same information for Ti-O distances. The energy of mixing calculations have shown that the new potential set is better at simulating the BCT solid solution and has therefore been used for all the strain and displacement calculations.

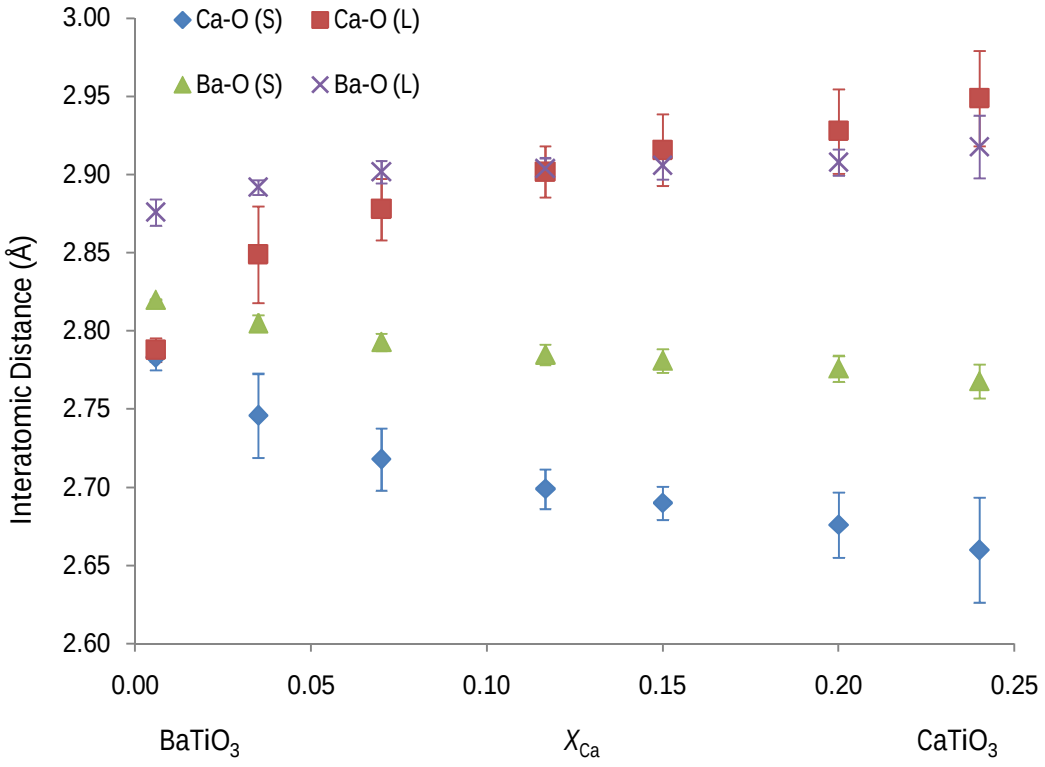

Figure 5.10: Calculated average values of the largest (L) and smallest (S) Ca-O and Ba-O interatomic distances in BCT. Error bars represent the standard deviation.

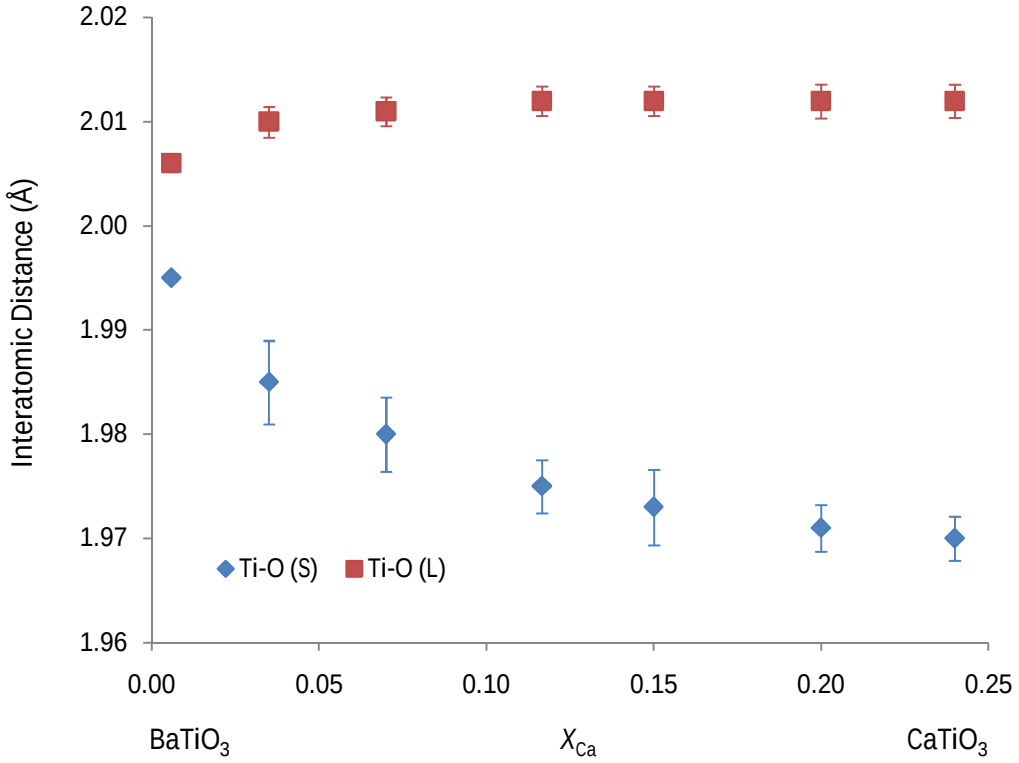

Figure 5.11: Calculated average values of the largest (L) and smallest (S) Ti-O interatomic distances in BCT. Error bars represent the standard deviation.

The BCT supercells decrease in size with increasing Ca concentration, as would be expected with Ca^{2+} (1.00 Å) being a smaller ion than Ba^{2+} (1.35 Å) [44]. Figure 5.10 does however show that the actual maximum Ca-O distances are increasing with Ca concentration. This suggests that strain is increasing in the system with the addition of more Ca up until the solid solution limit. This is especially so for the Ca-O bonds where beyond around 8 % Ca concentration, some of the Ca-O bonds are longer than the Ba-O bonds. It is possible that this is a result of reduction in co-ordination number of the A-site. The Ba-O average maximum and minimum distances also remain reasonably constant, whereas the Ca-O maximum and minimum distances continue to significantly deviate from each other up to the solid solution limit. Furthermore, the standard deviation is much greater for the Ca-O distances, with particularly large values between 3 and 8 % Ca concentration and near the solid solution limit. The Ca-O distances

calculated for *o*-$CaTiO_3$ range from 2.34 to 2.66 Å. These values are significantly smaller than the Ca-O distances calculated in BCT which suggests strong distortion is occurring in the CaO_{12} cluster. Figure 5.11 shows that the maximum Ti-O distances remains constant (unlike for Ca-O and Ba-O) and that the minimum Ti-O distances decreases with increasing Ca concentration due to the contraction of the cell resulting from the smaller Ca ions.

With regard to the ferroelectric behaviour of the system, these results do suggest that A-site strain may have a significant role at lower Ca concentrations, before size effects begin to dominate. One theory is that the distortion of these bonds at low concentrations (x < 8 %) causes increased displacement of the Ti^{4+} ions and hence stabilisation of the tetragonal phase. Beyond these low concentrations the deviation of the bond distances is not as dramatic resulting in T_c starting to decrease beyond 8 % Ca concentration. It is noteworthy to add that such levels of A-O disorder were not observed in the Sr-O and Ba-O bonds in BST. For these solid solutions, both sets of bond distances remained constant over the whole Sr concentration range. This further suggests a possible relationship between A-O bond disorder and the ferroelectric properties of BCT when compared to BST which experiences no unusual T_c effects with varying Sr concentrations.

5.4.2 Ca Off-centring in BCT

It is thought that A-site displacements (as opposed to the usually considered B-site displacements) may also contribute to this unusual T_c effect in BCT. A similar effect is witnessed in $PbTiO_3$, where A-site displacements are partially responsible for a high T_c in the material [45]. The potential for A-site displacements to contribute to the ferroelectric properties of BCT has been previously shown by XANES spectroscopy [46] and *ab initio* calculations [46-47]. Okajima *et al.* [46] used Ca K-edge XANES and DFT calculations to show that Ca ions substitute at Ba sites and that this substitution caused a small displacement in the *c*-axis as illustrated by figure 5.12. It has also been

suggested that the polarisation arising from Ca displacements works cooperatively with Ti-O distortions and that this stabilises the tetragonal phase of BCT [47].

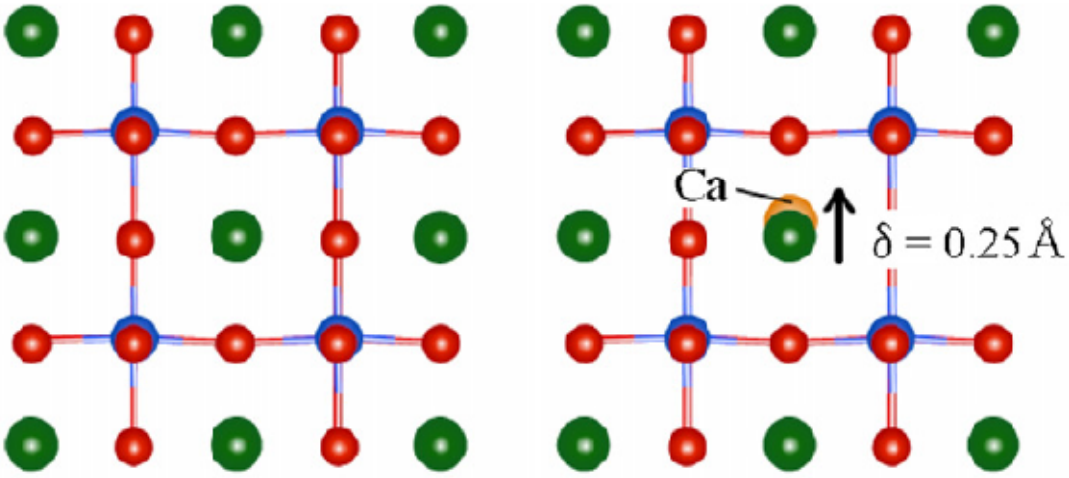

(a) (b)

Figure 5.12: The optimised structures obtained by PAW calculations for (a) $BaTiO_3$ and (b) Ca-doped $BaTiO_3$ [46] (explicit permission to reuse this image has been granted).

We used single point GULP simulations to calculate the energetic effect of displacement in a number of BCT configurations (~20) with varying Ca concentrations up to the solid solution limit. Each Ca ion in each configuration was systematically moved 0.01 Å around its lattice site in grid of 0.2 x 0.2 x 0.2 Å for a total of 9261 unique positions. The single point energy was then calculated after each movement. The lattice energies calculated were then compared to the lattice energy of the configuration without any displacements. These calculations were completed on a selection of 'strained' configurations where the difference between the shortest and longest Ca-O distances was at its largest and a selection of 'average' configurations chosen where the Ca-O distances were as consistent as possible. These sets of configurations were chosen to see if there were any additional effects from the most distorted configurations on the energy required for the displacements. Single point runs were chosen over full optimisation as it is impractical and far too time consuming to complete a full

optimisation after every Ca ion movement; this is especially true for the highest Ca concentrated configurations. Figure 5.13 shows the percentage of displacements (averaged out over each Ca ion) where the lattice energy was within a particular value compared to the original configuration lattice energy. These plots essentially show the ease with which displacements take place in the system.

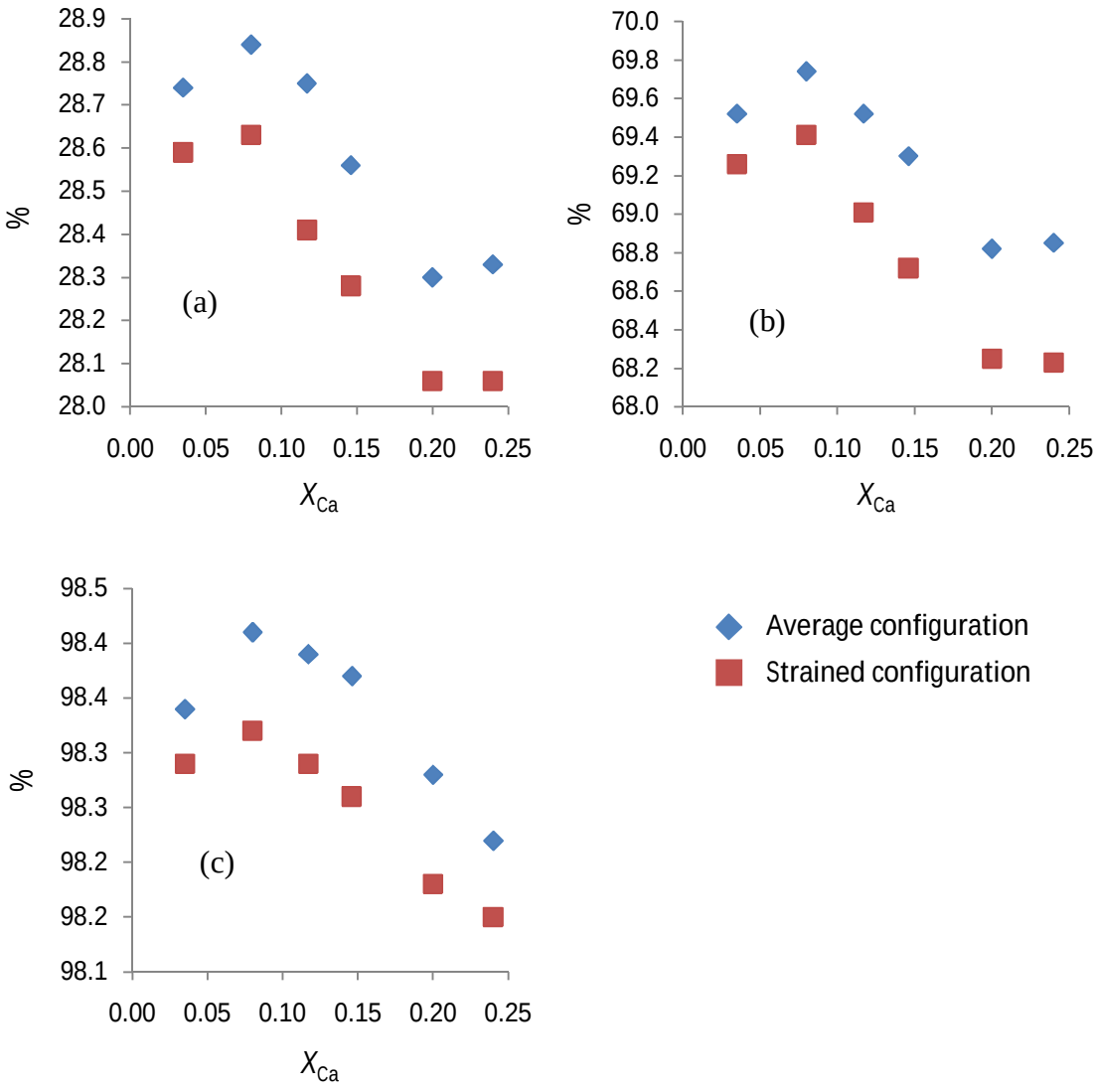

Figure 5.13: The percentage of configurations with displaced Ca ions with lattice energies within a set amount of the starting configuration lattice energy. (a) Within 1 eV, (b) within 2 eV and (c) within 4 eV.

The first thing to note about these calculations is that none of the thousands of unique displacements were energetically favoured when compared to the starting configuration i.e. the lattice energy of the displaced configuration is always higher than the energy of the starting point. However, there are a significant number of displacements (28-29 %) in both the average and strained configurations that are within an electronvolt of the starting configuration. Figure 5.13 also shows that displacements in the average configurations are energetically preferred over the entire solid solution range compared to the strained configurations, although the difference is minimal (~0.2 %). This is logical given that the distances of the Ca-O bonds in the less strained configurations tend to be more consistent and therefore there is less of an energetic penalty for a small displacement in a direction towards the neighbouring ions. This is not the case for the strained configurations where the Ca-O bond distances are considerably longer or shorter and as a result are closer to the surrounding cations. The closer proximity of the Ca ions to the surrounding cations means that even a small displacement will have a larger energetic penalty when compared to the Ca ions in the average configurations.

Both the strained and average configurations do exhibit the same trend of increasing ease of displacement up to ~8 mol% Ca followed by a decrease in the ease of displacement up to the solid solution limit. This is true for all three of the different energy thresholds. It is important that both sets of configurations display the same trend as it shows that if A-site displacements do contribute to the ferroelectric behaviour of BCT, then it is not only the most strained configurations that are responsible. The initial increase in Ca concentration causes a small increase in the ease with which displacements can occur. However, beyond the critical concentration the addition of more Ca begins to hinder Ca displacements. This is again suggests competing effects before and after the critical concentration of 8 mol% Ca and that size effects do still dominate after this concentration.

It is noteworthy that there is an interesting symmetry between the plots in figure 5.13 and the T_c plot for BCT given in figure 5.1. This symmetry suggests a direct relationship between T_c and possible Ca displacement in BCT. As suggested by Fu *et al.*

[47] it would seem that the off-centring of the Ca ions produces an electric dipole moment capable of stabilsing the tetragonal phase in BCT. At higher Ca concentrations this and any other strain effects are likely to be dominated by the size effect also seen in BST which stabilises the cubic structure [11].

5.5 Conclusions

We have calculated energy of mixing curves for the three perovskite solid solutions, $Ba_{1-x}Sr_xTiO_3$, $Ba_{1-x}Ca_xTiO_3$ and $Ca_{1-x}Ba_xTiO_3$. Two different potential sets have been used to calculate the curves and study the local structure of these solid solutions. A previous potential set used for calculations on $SrTiO_3$ and $CaTiO_3$ has been tested and compared to our new potential set combined with newly fitted Sr-O and Ca-O potentials. We have evaluated the validity of these potentials by comparing the results each produced as well as through comparison with experimental findings. Attempts to explain the unusual T_c behaviour of the $Ba_{1-x}Ca_xTiO_3$ system have also been made by investigating cation-oxygen interatomic distances and A-site displacement in the material.

It has been discovered that both potential sets succeed in replicating experimental trends. Low energies of mixing were found for the BST solid solution, suggesting full solubility which correlated with experiment. Our new potential set showed a small energy stabilisation at low concentrations of Sr that was not observed by the other potential set. This is thought to be a result of the stronger Sr-O interaction used in the CA potential set. Significantly larger energies of mixing were observed for the $BaTiO_3$-$CaTiO_3$ due to the increased size mismatch between the A-site Ba^{2+} and Ca^{2+} ions. These higher energy values also agreed with experiment as strict solubility limits exist in this system as opposed to the low energies and full solubility of the BST system. At the BCT and CBT solubility limits (24 mol% and 14 mol%, respectively) the FT potential set produced almost identical energies (~0.09 eV), suggesting good quantitative agreement with experiment.

Through the analysis of interatomic distances, we have discovered significant A-site disorder in the BCT solid solution, especially for Ca-O bonds. It is revealed that some Ca-O bonds are distorted and that these bonds are being stretched to lengths far greater than values seen in $CaTiO_3$. This distortion increases dramatically up to around 8 mol% Ca concentration and then increases further until the solid solution limit. Some bond distortion is also observed in Ba-O bonds; however this is at a far lesser extent than witnessed for Ca-O. Calculations on the off-centring of Ca ions in BCT also suggest a direct relationship between these displacements and the behaviour of T_c in the material. Displacements were shown to be favoured up to 8 mol% Ca concentration and then less favoured beyond this concentration. Our calculations strongly support the argument that strain plays a crucial role in controlling the ferroelectric properties of BCT up to 8 mol% and that the size effect begins to dominate beyond this point.

References

[1] S. Anwar, P. R. Sagdeo and N. P. Lalla, Journal of Physics: Condensed Matter **18**, 3455 (2006).

[2] D. Hennings, A. Schnell and G. Simon, Journal of the American Ceramic Society **65**, 539 (1982).

[3] Y. Hotta, G. W. J. Hassink, T. Kawai and H. Tabata, Japanese Journal of Applied Physics **42**, 5908 (2003).

[4] R. K. Zheng, J. Wang, X. G. Tang, Y. Wang, H. L. W. Chan, C. L. Choy and X. G. Li, Journal of Applied Physics **98**, 084108 (2005).

[5] L. Zhang, O. P. Thakur, A. Feteira, G. M. Keith, A. G. Mould, D. C. Sinclair and A. R. West, Applied Physics Letters **90**, 142914 (2007).

[6] T. Mitsui and W. B. Westphal, Physical Review **124**, 1354 (1961).

[7] C. L. Freeman, J. A. Dawson, H. Chen, J. H. Harding, L. -B. Ben and D. C. Sinclair, Journal of Materials Chemistry **21**, 4861 (2011).

[8] X. G. Tang, K. -H. Chew, J. Wang and H. L. W. Chan, Applied Physics Letters **85**, 991 (2004).

[9] S. Saha, T. P. Sinha and A. Mookerjee, European Physics Journal B **18**, 207 (2000).

[10] G. C. Mather, M. S. Islam and F. M. Figueiredo, Advanced Functional Materials **17**, 905 (2007).

[11] D. C. Sinclair and J. P. Attfield, Chemical Communications 1497 (1999).

[12] S. Lee, R. D. Levi, W. Qu, S. C. Lee and C. A. Randall, Journal of Applied Physics **107**, 023523 (2010).

[13] R. C. DeVries and R. Roy, Journal of the American Ceramic Society **38**, 142 (1955).

[14] K. Park, J. -G. Kim, K. -J. Lee, W. S. Cho and W. S. Hwang, Ceramics International **34**, 1573 (2008).

[15] H. Wen, X. H. Wang, L. Li and Z. Gui, Key Engineering Materials **280**, 65 (2005).

[16] L. Zhou, P. M. Vilarinho and J. L. Baptista, Journal of the European Ceramic Society **19**, 2015 (1999).

[17] J. -Ho. Jeon, Journal of the European Ceramic Society **24**, 1045 (2004).

[18] S. -S. Ryu, S. -K. Lee and D. -H. Yoon, Journal of Electroceramics **18**, 243 (2007).

[19] M. C. Chang and S. -C. Yu, Advanced Quantum Chemistry **37**, 179 (2000).

[20] M. E. Savinov, V. A. Trepakov, S. Kamba, S. E. Kapphan, J. Petzelt, R. Pankrath, I. L. Kislova, A. B. Kutsenko and L. Jastrabik, Ferroelectrics **295**, 31 (2003).

[21] A. Radoua, P. Delaye, R. Pankrath and G. Roosen, Journal of Optics A: Pure and Applied Optics **5**, S477 (2003).

[22] R. Varatharajan, S. B. Samanta, R. Jayavel, C. Subramanian, A. V. Narlikar and P. Ramasamy, Materials Characterization **45**, 89 (2000).

[23] Y. H. Han, J. B. Appleby and D. M. Smyth, Journal of the American Ceramic Society **70**, 96 (1987).

[24] Z. Q. Zhuang, M. P. Harmer, D. M. Smyth and R. E. Newnham, Materials Research Bulletin **22**, 1329 (1987).

[25] H. Tanaka, H. Tabata, K. Ota, and T. Kawai, Physical Review B **53**, 14112 (1996).

[26] S. Tinte, M. G. Stachiotti, S. R. Phillpot, M. Sepliarsky, D. Wolf and R. L. Migoni, Journal of Physics: Condensed Matter **16**, 3495 (2004).

[27] G. V. Lewis and C. R. A. Catlow, Journal of Physics and Chemistry of Solids **47**, 89 (1986).

[28] M. J. Akhtar, Z.-U.-N. Nisa, R. A. Jackson and C. R. A. Catlow, Journal of the American Ceramic Society **78**, 421 (1995).

[29] M. K. Karapet'yants and M. L. Karapel'yants, *Thermodynamic Constants of Inorganic and Organic Compounds* (Ann Arbor-Humphrey Science Publishers, Michigan, 1970).

[30] R. Crossley, Proceedings of the Physical Society **83**, 375 (1964).

[31] C. Moore, *Atomic Energy Levels*, vol. 3 (Clarendon Press, NBS (USA) Circular 467, 1958).

[32] C. Moore, *Atomic Energy Levels*, vol. 2 (Clarendon Press, NBS (USA) Circular 467, 1952).

[33] C. Moore, *Atomic Energy Levels*, vol. 1 (Clarendon Press, NBS (USA) Circular 467, 1949).

[34] R. Wycoff, *Crystal Structures* (John Wiley and Sons Ltd., New York, 1965).

[35] H. Zhang and M. S. T. Bukowinski, Physical Review B **44**, 2495 (1991).

[36] F. W. Lytle, Journal of Applied Physics **35**, 2212 (1964).

[37] S. Sasaki, C. T. Prewitt, J. D. Bass and W. A. Schulze, Acta Crystallographica C **43**, 1668 (1987).

[38] I. T. Todorov, N. L. Allan, M. Yu Lavrentiev, C. L. Freeman, C. E. Mohn and J. A. Purton, Journal of Physics: Condensed Matter **16**, S2751-S277 (2004).

[39] V. L. Vinograd, B. Winkler, A. Putnis, J. D. Gale and M. H. F. Sluiter, Chemical Geology **225**, 304 (2006).

[40] M. Yu. Lavrentiev, W. van Westrenen, N. L. Allan, C. L. Freeman and J. A. Purton, Chemical Geology **225**, 336 (2006).

[41] H. Salehi, N. Shahtahmasebi, and S. M. Hosseini, European Physics Journal B **32**, 177 (2003).

[42] J. Gale and A. Rohl, Molecular Simulation **29**, 291 (2003).

[43] D. Matra, *Ferroelectric Ceramics* (Maclaren and Sons LTD, London, 1966).

[44] R. D. Shannon, Acta Crystallographica **32**, 751 (1976).

[45] Y. Kuroiwa, S. Aoyagi, A. Sawada, J. Harada, E. Nishibori, M. Takata and M. Sakata, Physical Review Letters **87**, 217601 (2001).

[46] T. Okajima, K. Yasukawa and N. Umesaki, Journal of Electron Spectroscopy and Related Phenomena **180**, 52 (2010).

[47] D. Fu, M. Itoh, S. Koshihara, T. Kosugi and S. Tsuneyuki, Physical Review Letters **100**, 227601 (2008).

6

Oxygen Diffusion in $BaTiO_3$ and $SrTiO_3$

6.1 Introduction

Many of the fundamental properties and applications of perovskite materials are a result of diffusion. The understanding of oxygen ion diffusion in materials like $BaTiO_3$ and $SrTiO_3$ is therefore important for these and any future electrochemical applications. Oxygen diffusion is especially important in the main commercial use of $BaTiO_3$, multilayer ceramic capacitors (MLCCs). $BaTiO_3$ is often co-fired with Ni electrodes in a reducing atmosphere to avoid the oxidation of the Ni [1-2]. This reducing environment causes the formation of O vacancies which must be charge compensated by electrons and the reduction of Ti^{4+} to Ti^{3+} ions. However, these vacancies can seriously reduce the performance of the capacitor over its lifetime [3-4] and so acceptor dopants (e.g. rare-earth (RE)) are introduced to reduce the concentration of these O vacancies. These dopants have been shown to significantly reduce the oxygen diffusivity [5-6] and therefore increase the service time of these devices. The understanding of the rates and mechanisms of oxygen diffusion in $BaTiO_3$ is essential for improving the degradation of these ubiquitous devices.

Similar to $BaTiO_3$, $SrTiO_3$ has a number of electrical properties and applications which include strain-induced ferroelectricity for microwave devices [7] and a high relative permittivity for use in random access memory (RAM) [8]. Reduced $SrTiO_3$ also has a high Seebeck coefficient, necessary for thermoelectric applications [9], and was the first ternary oxide discovered to be superconducting [10]. Like $BaTiO_3$, many of the interesting features of $SrTiO_3$ are a result of its transport properties and in particular the transport properties of the most abundant point defect in $SrTiO_3$, O vacancies [11]. For

example, doped $SrTiO_3$ can be used as a varistor when prepared in a reducing atmosphere. In this application the O vacancies again create free electrons, but instead of hindering the device as is seen with $BaTiO_3$–based MLCCs, these vacancies help to create semiconducting grains [12]. $SrTiO_3$ also receives attention because of its ability to act as a reference system for mixed-conductors and for other similar perovskite systems [13-14]. Recently, $SrTiO_3$ has received additional interest because of its potential application in all-oxide electronics and as a memresistive element [13, 15-16]. For both of these uses, an understanding of O diffusion in the bulk material is paramount.

Given the importance of both these materials, it is unsurprising that there is a wealth of information on their diffusion properties available in the literature. Despite this fact, there are large variations in the experimentally measured chemical and self/tracer diffusion (see section 6.2.2) for both the doped and undoped materials. A compilation of diffusion data for $BaTiO_3$ from the literature is given in [1] and is discussed here. For the tracer diffusion of O, three data sets are provided and they all vary in magnitude significantly. For example, the diffusion data of Shirasaki *et al.* [6] shows a linear increase in diffusivity with temperature, with the diffusion coefficients, D_O, ranging from ~ 1 x 10^{-12} to 1 x 10^{-11} cm^2sec^{-1}. However, later results from Shirasaki *et al.* [17] show a far greater range of D_O over the ~ 1000 to 1700 K temperature range (~1 x 10^{-14} to 1 x 10^{-10} cm^2sec^{-1}). The chemical diffusion coefficients are unsurprisingly orders of magnitude greater than the tracer diffusion coefficients. The data from [1] also shows for donor (La)-doped $BaTiO_3$, diffusion is reduced when compared with the undoped material. This is in agreement with other results [3-4]. The tracer diffusion coefficient of O has also been reported to be ~ 2 x 10^{-11} cm^2sec^{-1} elsewhere [18-19]. The oxygen self-diffusion activation energy has been calculated at 48 $kJmol^{-1}$ in both single crystal and poly-crystalline samples [20].

A similar level of variation in the diffusion coefficients for $SrTiO_3$ also exists, as shown by the collection of experimental data presented in figure 6.1 [21]. Generally, the results show higher values for D_O compared to the values for $BaTiO_3$. Similar to $BaTiO_3$, the increase in diffusivity with temperature is far greater in some cases. For

example, plot 7 in figure 6.1 shows D_O increases by approximately 3 orders of magnitude (~ 1 x 10^{-11} to 1 x 10^{-8} cm^2sec^{-1}) over a temperature range of ~ 300 K, whereas over a larger temperature range (~ 600 K) other D_O data show an increase of less than 2 order of magnitude (~ 5 x 10^{-11} to 5 x 10^{-9} cm^2sec^{-1}) (see plots 1 and 2 from figure 6.1). Figure 6.1 also shows that again, donor-doping (in this case La and Dy) significantly reduces O diffusion in the material. A more recent study using time-of-flight secondary ion mass spectroscopy (ToF-SIMS) found the O tracer diffusion coefficient in single-crystal $SrTiO_3$ to be ~ 1 x 10^{-11} cm^2sec^{-1} with only a small increase with increasing temperature (950 K – 1150 K) [13]. An oxygen vacancy migration energy of 0.6 eV was calculated from this data.

Although there are numerous computational studies (using a variety of different methods) of diffusion in perovskites and similar metal oxide materials [22-24], there is a surprising lack of work on diffusion in $BaTiO_3$ and $SrTiO_3$. There are very few publications in the literature concerning the modelling of diffusion in $BaTiO_3$ and to the best of our knowledge there exists only one publication featuring mean square displacement (MSD) data for $BaTiO_3$ [25]. Kubo *et al.* [25] completed MSD calculations for Ba and O (as well as for Sr and O in $SrTiO_3$), however no diffusion activation energies were calculated. Another molecular dynamics study of oxygen vacancy diffusion in $BaTiO_3$ has been completed [26]. This work confirmed experimental findings that La-doping reduces O vacancy diffusion by the production of cation vacancies and the reduction of the lattice volume. Calculations by Lewis and Catlow [27] estimated that the activation energy of O vacancy diffusion in $BaTiO_3$ is 0.62 eV and that the cation vacancy activation energies are significantly larger i.e. (3.45 eV for V_{Ba} and 15.12 eV for V_{Ti}).

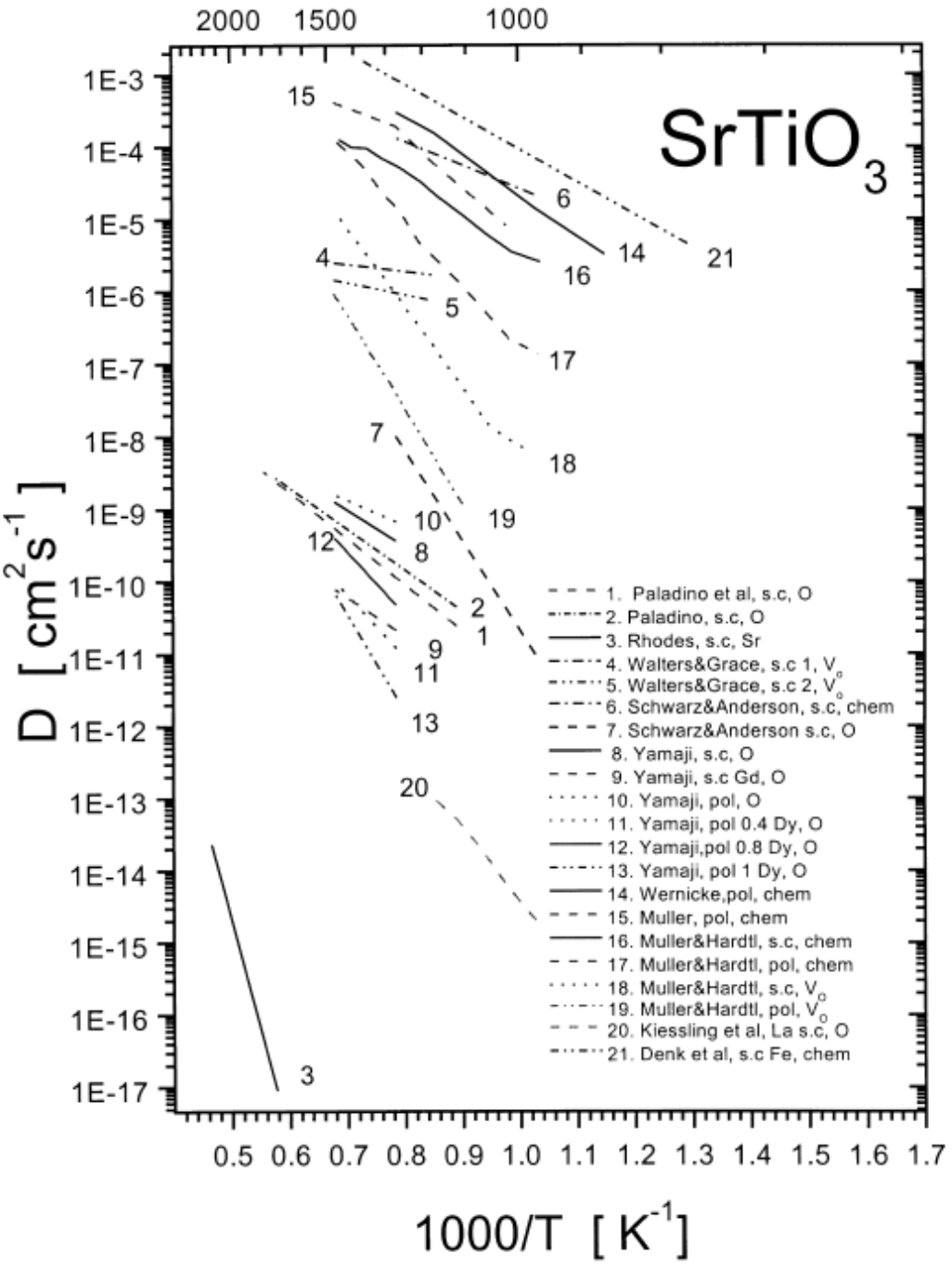

Figure 6.1: Comparison of the diffusion coefficients in $SrTiO_3$; s.c-single crystal, pol-polycrystalline specimen; O, Sr, V_O, chem-diffusion coefficients of oxygen, strontium, oxygen vacancies and chemical, respectively [21] (explicit permission to reuse this image has been granted).

For $SrTiO_3$, there are also calculations of the diffusion of oxygen vacancies in $SrTiO_3$ [28]. Values of D_O were calculated by MSD calculations and then converted to V_O diffusion coefficients, D_V, using,

$$D_V[V] = D_O[O] \tag{6.1}$$

An activation energy of 0.93 eV for O vacancy migration was derived from the diffusion coefficients. Lattice statics calculations were also used to examine the interactions and binding energies between adjacent O vacancies. Akhtar *et al.* [11] also used lattice statics to calculate an O vacancy activation energy of 0.75 eV. Density functional theory (DFT) calculations have estimated the O migration energy to be between 0.4 and 0.7 eV [29-30].

In this chapter we establish the correct charge compensation mechanism for O vacancies in $BaTiO_3$ and $SrTiO_3$ and which O vacancy concentration produces the best fit to experimental diffusion data and activation energies. This is done using MD simulations and in particular MSD plots to calculate D_O and activation energies of diffusion for a range of O vacancy concentrations. It is hoped that these results will give a better understanding into the process of O diffusion in these materials and also the application of these techniques in studying such phenomena.

6.2 Method

6.2.1 Diffusion in Solids

In solid materials diffusion can occur via a number of different mechanisms. Perhaps the most basic of these mechanisms is vacancy diffusion which involves the exchange of an atom at a regular atom site with a vacancy as shown pictorially in figure 6.2.

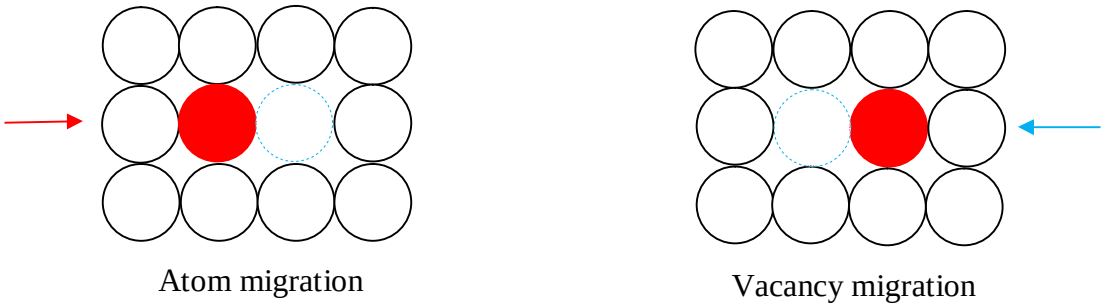

Figure 6.2: Illustration of vacancy diffusion in solids.

In vacancy diffusion, the atoms and vacancies are exchanging positions and therefore the diffusion is proportional to the concentration of vacancies. Atoms use the energy from thermal vibrations to 'break' the bonds with their neighbours and therefore diffusion increases with temperature.

Another type of diffusion in solids is interstitial diffusion. In this example, an atom at an interstitial lattice site 'jumps' to another interstitial position in the lattice (figure 6.3). This type of diffusion is more common with smaller ions as they are more likely to occupy interstitial sites.

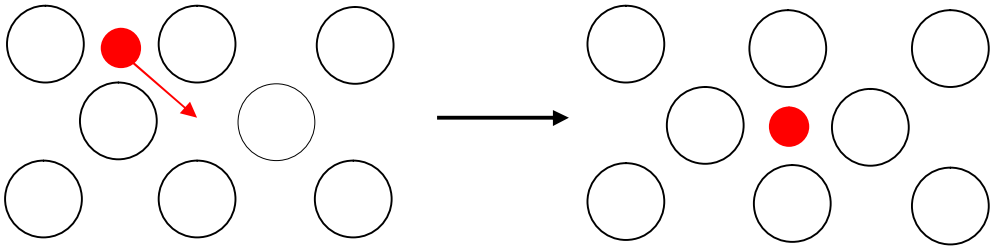

Figure 6.3: Illustration of interstitial diffusion in solids.

6.2.2 Calculating Diffusion Coefficients

Self-diffusion or tracer diffusion is defined as the diffusion of atoms without a concentration gradient. This is distinct from chemical diffusion where a concentration gradient is present when the diffusion coefficient is measured [31]. Chemical diffusion is often associated with binary systems such as alloys because of the migration of atoms from a high concentration area to a low concentration area, a process also known as interdiffusion [32-33]. The tracer diffusion is usually measured by introducing a small concentration of isotopes (e.g. ^{18}O to study O diffusion) which can be detected by analytical techniques such as secondary ion mass spectrometry (SIMS) [13].

The diffusion activation energy is calculated (both experimentally and in the calculations presented here) from an Arrhenius plot of $\ln[D_i(p,T)]$ against $1/T$,

$$D_i(p,T) = D_{i,0} \exp^{(-E_i^{act}(p.T)/k_B T)} \tag{6.2}$$

where $D_i(p,T)$ is the diffusion coefficient, $D_{i,0}$ is the pre-exponential factor and $E_i^{act}(p,T)$ is the activation energy.

In molecular dynamics we can use MSD plots to study the movement of ions and to calculate the diffusion coefficient for that particular species. The MSD for a species with N particles is expressed as,

$$\text{MSD} = \frac{1}{N}\sum_{n-1}^{N}\left\langle (r_n(t_0+t) - r_n(t_0))^2 \right\rangle \tag{6.3}$$

where t_0 represents the initial time origins and r_n represents the positions of the particles at a particular time, t. The MSD is an average of the distance travelled over time and is taken over all particles. The diffusion coefficient can be obtained from the MSD,

$$\text{MSD} = 6Dt + \text{constant} \tag{6.4}$$

where D is the diffusion coefficient. This expression is known as the Einstein relation, as Einstein showed that the mean square of the distance travelled by a particle via a random walk is proportional to the time elapsed [34]. This relation was based on Einstein's work on Brownian motion and its relation to diffusion in general.

6.2.3 MD Calculation Details

The calculations in this chapter were completed using the widely available MD code, DL_POLY_2 [35]. In these calculations, the ions are treated as rigid spheres (i.e. the rigid ion model [36]) and the shell model has not been applied to maximise computational efficiency. We have used the same $BaTiO_3$ and $SrTiO_3$ potential sets as previously discussed in chapters 4 and 5 and the same cut-off distance of 12 Å was applied for all the calculations. Supercells of 7 x 7 x 7 (1715 atoms) were used for the MSD calculations.

The starting configurations for all of the MD simulations were optimised using GULP [37] to start the simulation with the minima of that particular configuration. An equilibration time of 10 ps was used for the vast majority of the simulations which is around 1 % of the total simulation run time of 1 ns. Some simulations were run for 2 ns to ensure the most accurate MSD plots possible. A time step of 1 fs was used for all the calculations and the MSDs were calculated every 50 time steps. We used the canonical *NPT* ensemble and the Nose-Hoover thermostat/barostat with a relaxation time of 0.1 ps for both the thermostat and barostat. The leapfrog Verlet algorithm was used to integrate Newton's equations of motion.

For the diffusion calculations, a random distribution of O vacancies was inserted into each starting configuration. Charge compensation was achieved via a number of different mechanisms and is discussed in the results section.

6.3 Thermal Expansion of *c*-$BaTiO_3$ and *c*-$SrTiO_3$

In addition to being an important property, the coefficient of thermal expansion (CTE) provides a good measure of whether the potential sets are capable of accurately reproducing basic macroscopic properties. The calculated thermal expansion of these materials is given in figure 6.4. To order to obtain accurate values for volumes, the simulations were each run for 1 ns and equilibrated for 10 ps.

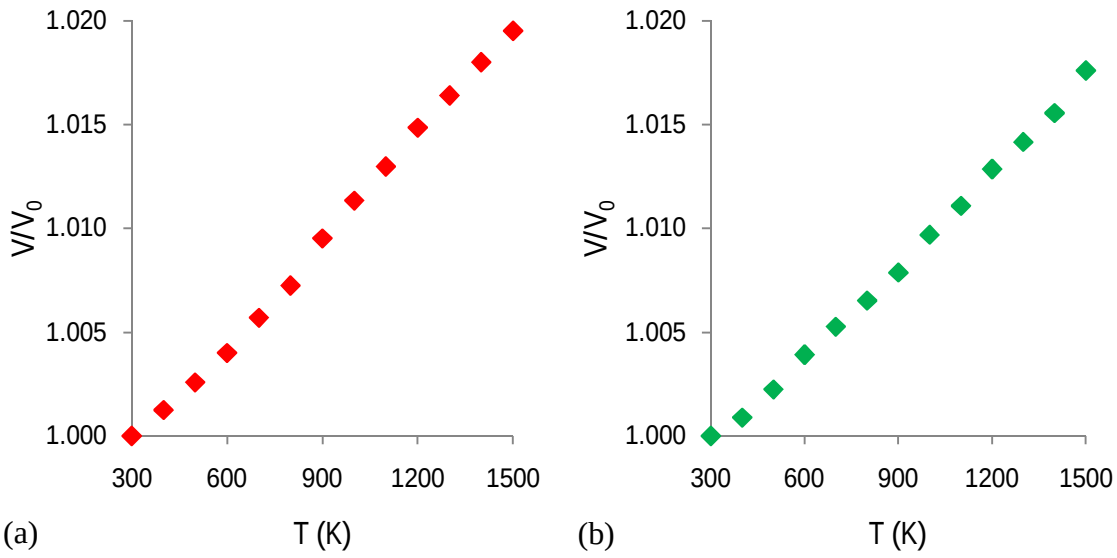

Figure 6.4: Volume thermal expansion as a function of temperature for (a) *c*-$BaTiO_3$ and (b) *c*-$SrTiO_3$.

For *c*-$BaTiO_3$, a volume thermal expansion coefficient of 1.63 x 10^{-5} K^{-1} and a linear thermal expansion coefficient of 0.54 x 10^{-5} K^{-1} were calculated. Slightly smaller values were calculated for *c*-$SrTiO_3$; 1.47 x 10^{-5} K^{-1} and 0.49 x 10^{-5} K^{-1} for the volume and linear coefficients, respectively. There is a large range of experimental values for the linear thermal expansion that vary significantly based on temperature, grain size and the structure. Xiao *et al.* [38] recorded values for the linear thermal expansion coefficient ranging from 0.23 x 10^{-5} K^{-1} for samples with large grain sizes at a sintering temperature of 1200 °C to 0.73 x 10^{-5} K^{-1} for samples with smaller grains at a sintering temperature of 1000 °C. In another study of the thermal properties of $BaTiO_3$, a linear thermal expansion coefficient of ~ 0.6 x 10^{-5} K^{-1} was observed at room temperature where $BaTiO_3$ is ferroelectric [39]. However, beyond the ferroelectric Curie temperature (i.e. the cubic structure) the values for linear expansion rises to ~ 1.1 x 10^{-5} K^{-1}. Kubo *et al.* [25] used MD calculations to calculate a value of 1.22 x 10^{-5} K^{-1}, although it is not clear whether this value is the volume or linear thermal expansion coefficient. DFT calculations produced values for the rhombohedral phase of 0.46 x 10^{-5} K^{-1} at 100 K and 0.69 x 10^{-5} K^{-1} at 180 K [40].

For *c*-$SrTiO_3$, we obtained a volume expansion coefficient of 1.47 x 10^{-5} K^{-1} and a linear expansion coefficient of 0.49 x 10^{-5} K^{-1}. These values are slightly smaller than those obtained for $BaTiO_3$. This is somewhat supported by experiment where a value of 1.04 x 10^{-5} K^{-1} (compared to ~ 1.2 x 10^{-5} K^{-1} for $BaTiO_3$) was obtained [25]. MD calculations also support this with the same thermal expansion value of 1.04 x 10^{-5} K^{-1} for $SrTiO_3$. Further MD calculations produced a somewhat larger value 0.73 x 10^{-5} K^{-1} compared to our calculations for the linear expansion coefficient [28].

Although the level of variation in the experimental and simulated values is high, our calculated values are in good agreement and are well within this variation. This suggests that our potential sets are capable of reproducing the basic structural properties of these materials.

6.4 Oxygen Diffusion in *c*-$BaTiO_3$

6.4.1 Mean Square Displacement of Oxygen Ions

We studied the diffusion of oxygen in $BaTiO_3$ cells with V_O concentrations of 10, 5, 3 and 2 %. These values were chosen to give a wide range of data and so that the significance of the V_O concentration can be assessed. A similar concentration range was chosen for other MD simulations on O diffusion in $SrTiO_3$ [28]. To charge compensate these vacancies, we considered three possible mechanisms,

1. Compensation by reduction of B-site ions ($2Ti^{4+}$ ions to $2Ti^{3+}$ per V_O).

2. Compensation by A-site vacancies (V_{Ba} per V_O).

3. Compensation by B-site vacancies (V_{Ti} per $2V_O$).

For the second mechanism, a V_O concentration of 10 % was not considered as this would require 10 % V_{Ba} concentration and is clearly not probable or indeed physically possible. A selection of MSD plots for different concentrations and mechanisms are given in figure 6.5. The final 10 % of the simulation time have been removed because

of the poor statistics usually associated with the final section of a MSD calculation. All MSD calculations were completed over a 1 ns duration apart from the calculations with 2 % V_O concentration which were calculated over a 2 ns duration. The temperature range for the simulations (900 – 1500 K) was chosen on the basis of experimental results.

Figure 6.5 shows that all of the MSD plots increase linearly with time and therefore that O ions migrate through the system. Unsurprisingly, the diffusivity increases in cells with higher concentrations of V_O. For example, the MSD for 2 % V_O concentration at 0.5 ns is ~ 0.3 $Å^2$ compared to ~ 1.3 $Å^2$ at the same time for 10 % V_O concentration, although of course the type of charge compensation will also contribute this difference. In order to appreciate the true effects of the vacancy concentration and the charge compensation mechanism, the diffusion coefficients and activation energies must be calculated.

6.4.2 Diffusion Coefficients for Oxygen

The diffusion coefficients for O were calculated using equation (6.4) for each of the V_O concentrations and each of the compensation mechanisms and are given in tables 6.1 - 6.3. The 2 % V_O concentration was only considered for the Ti^{3+} compensation mechanism because both the calculations here (sections 6.4.2 and 6.4.3) and experimental [42] results show this to be the correct charge compensation mechanism.

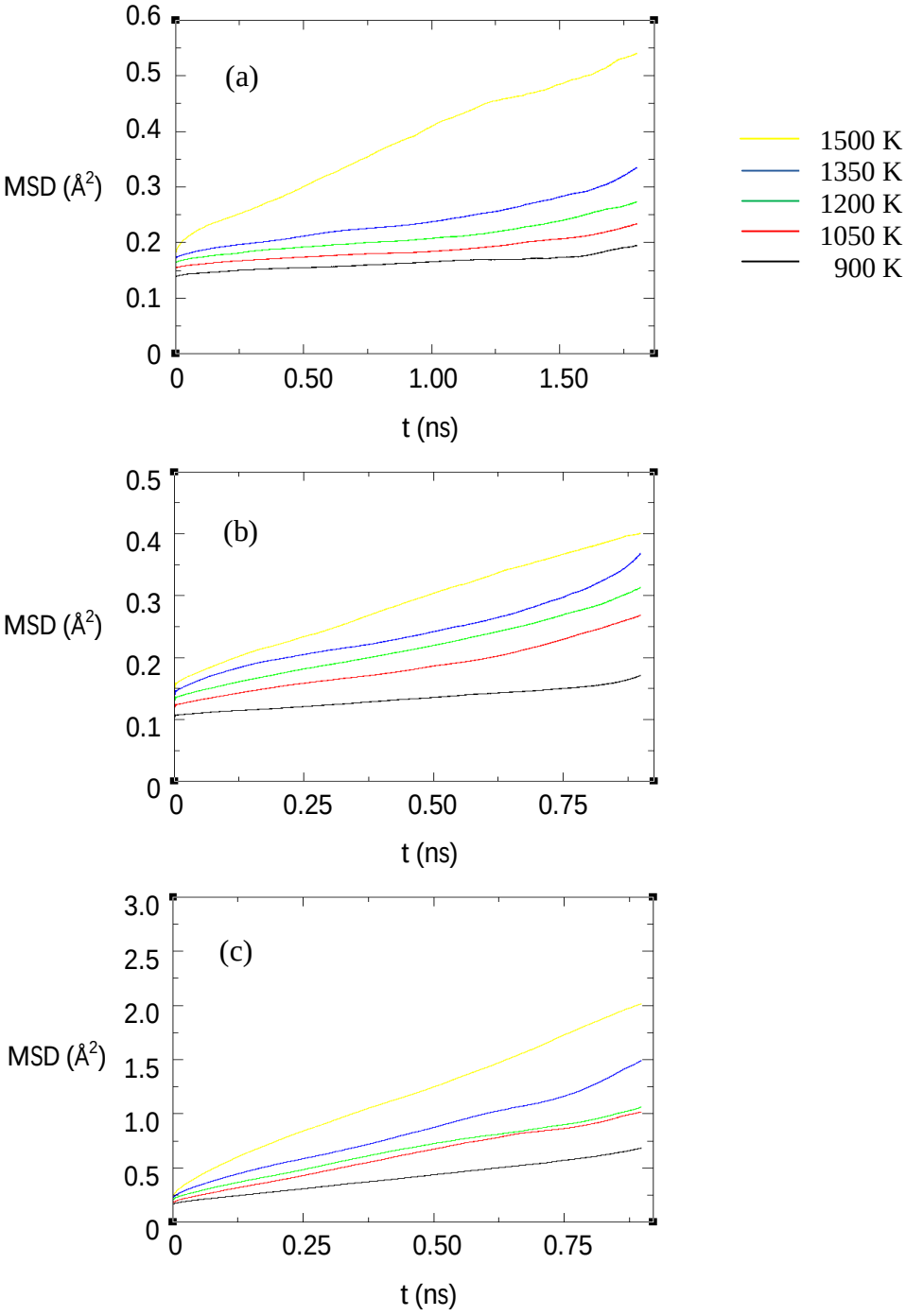

Figure 6.5: Mean square displacement (MSD) of O ions in cells with different V_O concentration and charge compensation mechanisms. (a) 2 % V_O concentration with Ti^{3+} charge compensation, (b) 3 % V_O concentration with V_{Ba} charge compensation and (c) 10 % V_O concentration with V_{Ti} charge compensation.

	Diffusion Coefficient (D_O) (cm^2s^{-1})			
Temperature (K)	10 % V_O	5 % V_O	3 % V_O	2 % V_O
900	4.99×10^{-9}	1.34×10^{-9}	1.15×10^{-9}	2.74×10^{-10}
1050	7.62×10^{-9}	4.11×10^{-9}	2.50×10^{-9}	6.40×10^{-10}
1200	1.28×10^{-8}	5.37×10^{-9}	3.42×10^{-9}	9.58×10^{-10}
1350	1.46×10^{-8}	4.98×10^{-9}	4.52×10^{-9}	1.42×10^{-9}
1500	2.03×10^{-8}	6.02×10^{-9}	5.70×10^{-9}	2.54×10^{-9}

Table 6.1: Oxygen diffusion coefficients for the Ti^{3+} charge compensation mechanism.

	Diffusion Coefficient (D_O) (cm^2s^{-1})	
Temperature (K)	5 % V_O	3 % V_O
900	3.22×10^{-9}	9.22×10^{-10}
1050	3.69×10^{-9}	2.62×10^{-9}
1200	3.88×10^{-9}	3.13×10^{-9}
1350	4.61×10^{-9}	3.50×10^{-9}
1500	1.19×10^{-8}	4.29×10^{-9}

Table 6.2: Oxygen diffusion coefficients for the V_{Ba} charge compensation mechanism.

	Diffusion Coefficient (D_O) (cm^2s^{-1})		
Temperature (K)	10 % V_O	5 % V_O	3 % V_O
900	8.54×10^{-9}	1.53×10^{-9}	1.40×10^{-9}
1050	1.37×10^{-8}	2.72×10^{-9}	1.66×10^{-9}
1200	1.67×10^{-8}	4.01×10^{-9}	1.66×10^{-9}
1350	1.88×10^{-8}	5.27×10^{-9}	2.70×10^{-9}
1500	3.09×10^{-8}	6.98×10^{-9}	5.47×10^{-9}

Table 6.3: Oxygen diffusion coefficients for the V_{Ti} charge compensation mechanism.

Tables 6.1 - 6.3 again shows that reducing the V_O concentration also reduces the O diffusivity because of the smaller concentration of defects that are available for

migration. In the majority of cases a decrease in V_O concentration from 10 to 2 % or 3 % causes a reduction in diffusivity of up to an order of magnitude. This illustrates the importance of choosing the correct concentration of V_O for these calculations and also how the calculated diffusion coefficients can be used to find the V_O concentration that best fits to experimental data. These results also show the difficulty that sometimes occurs in extracting diffusion coefficients from a MSD plot of a particle in a solid system. For example, the diffusion coefficients for 1050 K and 1200 K at a 3 % V_O concentration with V_{Ti} compensation suggest that diffusion has not increased for this temperature rise. This is a result of two MSD plots being very similar and the difficulty in sometimes selecting which place to calculate the gradient when the plot is not completely linear. Fortunately, this is only true for a couple of examples and has no major bearing on the calculated activation energy as long as the other diffusion coefficients increase appropriately with temperature.

An interesting feature of this data is that for a 3 % V_O concentration, the mechanism with the highest O diffusion is actually the Ti^{3+} compensation mechanism. This is somewhat counterintuitive as this cell actually has fewer vacancies in it compared to the cells of the other mechanisms at this V_O concentration. For the other V_O concentrations this is not the case and diffusion is higher for the V_{Ba} and V_{Ti} mechanisms. This suggests that at low V_O concentrations, O diffusion is favoured by a reduction in the strong Ti^{4+} - O^{2-} Coulombic interactions rather than simply more free space in the lattice caused by A- and B-site vacancies.

If we compare our results to experimental measurements of O tracer diffusion [1] as discussed in the introduction, we see that the 2 % V_O concentration with Ti^{3+} charge compensation has the best agreement. For the 900 – 1200 K temperature range, the calculated diffusion coefficients are around an order of magnitude greater than the experimental results of Shirasaki *et al.* [6]. At higher temperatures, the agreement is better [6, 17]. Given the difficulty of calculating diffusion coefficients comparable to experimental results using MD methods, the difference between our results and the experimental work is acceptable. Although much useful information can be gained from analysing the diffusion coefficients, it is the diffusion activation energies that reveal the

most significant information and answer the question whether our potential sets can accurately model the diffusion behaviour in these systems.

6.4.3 Diffusion Activation Energies for Oxygen

The O diffusion activation energies (E_{act}) calculated for each charge compensation mechanism and V_O concentration using equation (6.2) are presented in table 6.4. A selection of Arrhenius plots for these calculations are given in figure 6.6.

	Activation Energy (E_{act}) (eV)		
V_O concentration	Ti^{3+} compensation	V_{Ba} compensation	V_{Ti} compensation
10 % V_O	0.27	-	0.22
5 % V_O	0.27	0.20	0.29
3 % V_O	0.30	0.28	0.23
2 % V_O	0.41	-	-

Table 6.4: Oxygen diffusion activation energies for a range of charge compensation mechanisms and V_O concentrations.

With the exception of the V_{Ti} compensation mechanism, the activation energies increase with reducing V_O concentration as expected. For the experimentally proven mechanism (Ti^{3+} compensation) there is no change in activation energy between 10 % and 5 % V_O concentrations. However, at lower concentrations the activation energy rises to 0.41 eV, the largest value of activation energy for all possibilities simulated. The activation energies for the other mechanisms are lower and in the case of V_{Ti} compensation, there is no strong trend between V_O concentration and E_{act}. The lack of such a trend suggests that the high concentration of metal vacancies necessary to compensate V_O in these mechanisms is too high and is not realistic.

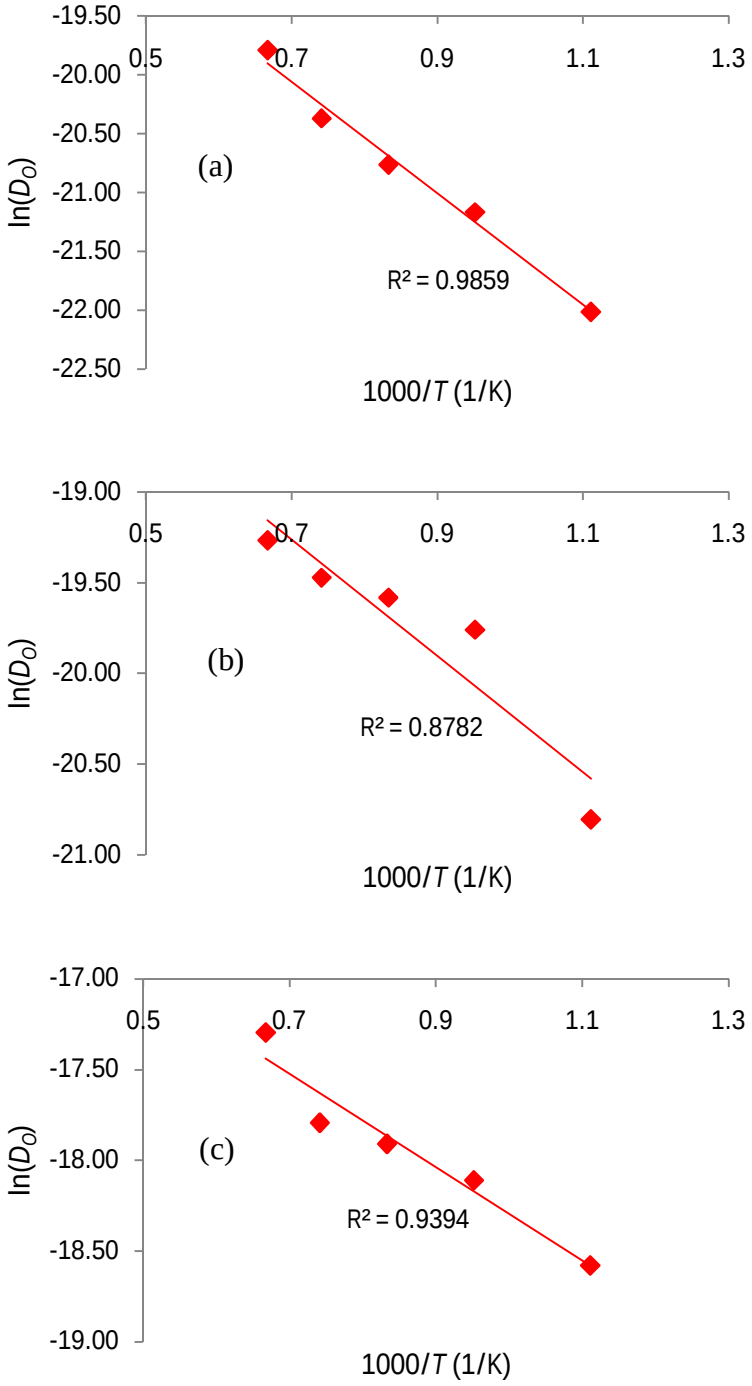

Figure 6.6: Arrhenius plots of ln (D_O) against 1/T for cells with different V_O concentration and charge compensation mechanisms. (a) 2 % V_O concentration with Ti^{3+} charge compensation, (b) 3 % V_O concentration with V_{Ba} charge compensation and (c) 10 % V_O concentration with V_{Ti} charge compensation.

These results indicate that in agreement with experiment, Ti^{3+} charge compensation is the dominant mechanism in O-deficient $BaTiO_3$.

As discussed there is a large range of calculated experimental and theoretical activation energies in the literature for O diffusion. Lin *et al.* [43] provides a good overview of some of the previously quoted values that have been obtained using various different methods. These values range from 0.44 eV [6] (tracer diffusion experiments) to 4.86 eV [44] (sintering model). Our value of 0.41 eV is in good agreement with the tracer diffusion value. When considering activation energies, self-diffusion data is often considered comparable to tracer diffusion because the activation energies are not usually affected by correlation effects and therefore it is reasonable to compare values from the two methods. Other activation energies obtained from self-diffusion measurements (0.55 eV) [19] and lattice statics calculations (0.62 eV) [45] are also in reasonable agreement. Again this shows that the Ti^{3+} charge compensation mechanism is in the best agreement with experiment and that the activation energies of the other mechanisms are too low. However, it is noteworthy to add that a significant difference between the calculations here and experiment is the contribution of the binding energy between defects. In reality, the activation energies for the V_{Ti} and V_{Ba} mechanisms would also contain the energy required to separate Coulombically attracted vacancies. For example, because of its charge $V_{Ti}^{'''}$ has a high migration energy and it will attract and bind $V_O^{\cdot\cdot}$.

6.5 Oxygen Diffusion in *c*-$SrTiO_3$

6.5.1 Mean Square Displacement of Oxygen Ions

For $SrTiO_3$, we studied the diffusion of oxygen with charge compensation by Ti^{3+} ions only. It is clear that this is the correct mechanism for $BaTiO_3$ and it is well known experimentally [46-48] that this is also the correct mechanism for $SrTiO_3$. The calculations on $BaTiO_3$ also indicate that a V_O concentration greater than ~ 3 % does not produce the correct diffusion properties. It is noteworthy to add that $SrTiO_3$ with a V_O

concentration of up to 10 % can be formed [46]. The MSD for 2 % V_O example is given in figure 6.7. The simulations were again run for a 1 ns and the same temperature range was used.

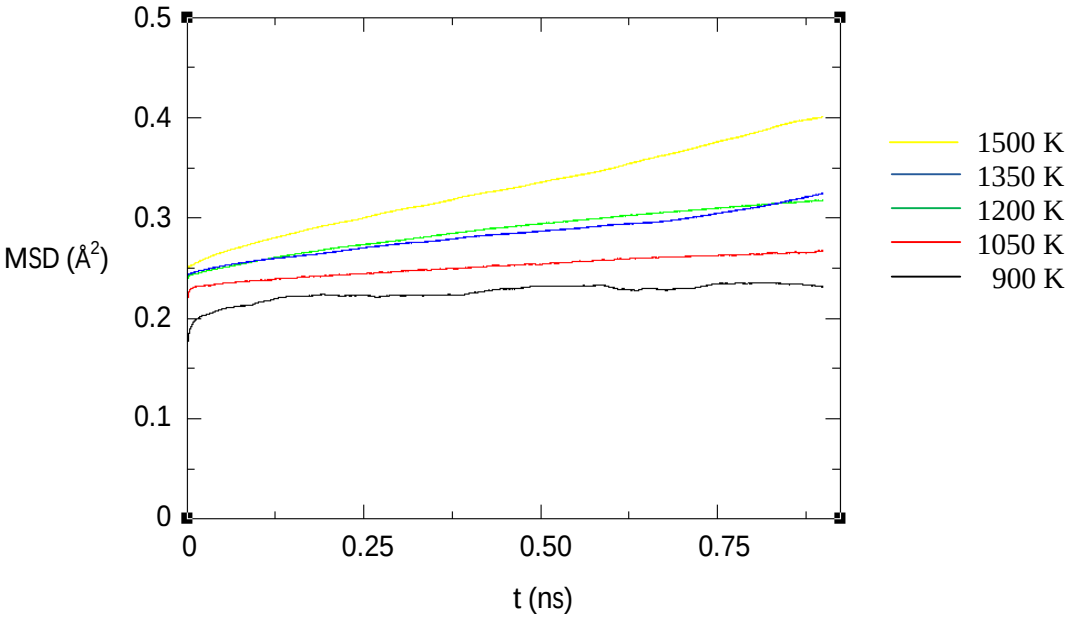

Figure 6.7: Mean square displacement (MSD) of O ions in $SrTiO_3$ with a V_O concentration of 2 % and Ti^{3+} charge compensation.

Similar to $BaTiO_3$, all the MSD increases over time, although sometimes the diffusion coefficient can be small as shown by the MSD for 900 K in figure 6.7. Figure 6.7 also shows again the difficulty in selecting an appropriate place to measure the gradient, as the plots for 1200 and 1350 K overlap. In this instance, the linear section at the end of the MSD plot was used to calculate the gradient for 1350 K.

6.5.2 Diffusion Coefficients for Oxygen

The O diffusion coefficients for a range of V_O concentrations in $SrTiO_3$ are presented in table 6.5. For the vast majority of D_O values, there is a decrease in the diffusion coefficient with decreasing V_O concentration. Comparison of D_O for $SrTiO_3$ and $BaTiO_3$ shows that generally O diffusion is higher in $SrTiO_3$ and that this is especially true at lower V_O concentrations and at lower temperatures. For example at 900 K, the value of D_O for $SrTiO_3$ is twice that of $BaTiO_3$ for a V_O concentration of 2 %. This also suggests that the activation energy for O diffusion in $SrTiO_3$ is less than that of $BaTiO_3$.

De Souza *et al.* [13] have measured the bulk tracer diffusion coefficient of O for temperatures between 950 -1150 K. Their values ranged from ~ 1.0×10^{-11} to 3.0×10^{-11} cm^2s^{-1}. Similar to $BaTiO_3$, our calculated values are within an order of magnitude of these experimental results. Although, our values are larger than the experimental ones, it is noteworthy that the gradients (and therefore the activation energies) are very similar. Other experimental results show very good agreement with our results, especially over the 1200 to 1500 K range [21]. As previously discussed, the majority of computational studies on these materials focus on the activation energies of diffusion and therefore there is little or no diffusion data with which to better compare. The agreement between our data and experimental data is generally greater for $SrTiO_3$ than for $BaTiO_3$.

	Diffusion Coefficient (D_O) (cm^2s^{-1})		
Temperature (K)	5 % V_O	3 % V_O	2 % V_O
900	2.87×10^{-9}	1.33×10^{-9}	5.40×10^{-10}
1050	3.92×10^{-9}	1.53×10^{-9}	9.10×10^{-10}
1200	4.02×10^{-9}	2.92×10^{-9}	1.65×10^{-9}
1350	4.77×10^{-9}	4.78×10^{-9}	1.90×10^{-9}
1500	7.17×10^{-9}	5.78×10^{-9}	2.90×10^{-9}

Table 6.5: Oxygen diffusion coefficients for $SrTiO_3$ with the Ti^{3+} charge compensation mechanism.

6.5.3 Diffusion Activation Energies for Oxygen

The O diffusion activation energies (E_{act}) calculated for $SrTiO_3$ with a range of V_O concentrations using equation (6.2) are presented in table 6.6. The Arrhenius plots for these calculations are given in figure 6.8.

	Activation Energy (E_{act}) (eV)
V_O concentration	Ti^{3+} compensation
5 % V_O	0.15
3 % V_O	0.31
2 % V_O	0.32

Table 6.6: Oxygen diffusion activation energies for $SrTiO_3$ cells with a range of V_O concentrations.

The results in table 6.6 show that the reduction of the V_O concentration from 5 to 3 % causes a significant increase in E_{act}. However when the V_O concentration is reduced further, the increase in E_{act} is far smaller. This was not observed for $BaTiO_3$ and suggests the possibility that $SrTiO_3$ can form V_O more easily than $BaTiO_3$ and perhaps that the concentration of V_O is generally higher in $SrTiO_3$. Regardless of this, the E_{act}

value for the 5 % V_O concentration case is clearly too small. Another interesting difference between these two materials is that E_{act} is generally smaller in $SrTiO_3$, although the difference is not considerable and experimental results also suggest that the value for both materials is very similar.

Although there is a wealth of data for the diffusion coefficient of O in $SrTiO_3$, there is far less information on the activation energy for O diffusion. There are, however, numerous results for the V_O migration energy in $SrTiO_3$. De Souza *et al.* [13] obtained a value of 0.58 eV for the activation enthalpy of O isotopes. From this value a value of ~ 0.6 eV was calculated for the V_O migration energy. De Souza *et al.* also present a compilation of V_O migration energies. These values range from 0.3 to 2.1 eV for experimental methods and 0.4 to 1.35 eV for DFT and pair potential calculations. Our value of 0.32 eV is somewhat lower than some of these quoted values but it is within 0.3 eV of the majority of these values and in some cases it is within 0.1 eV.

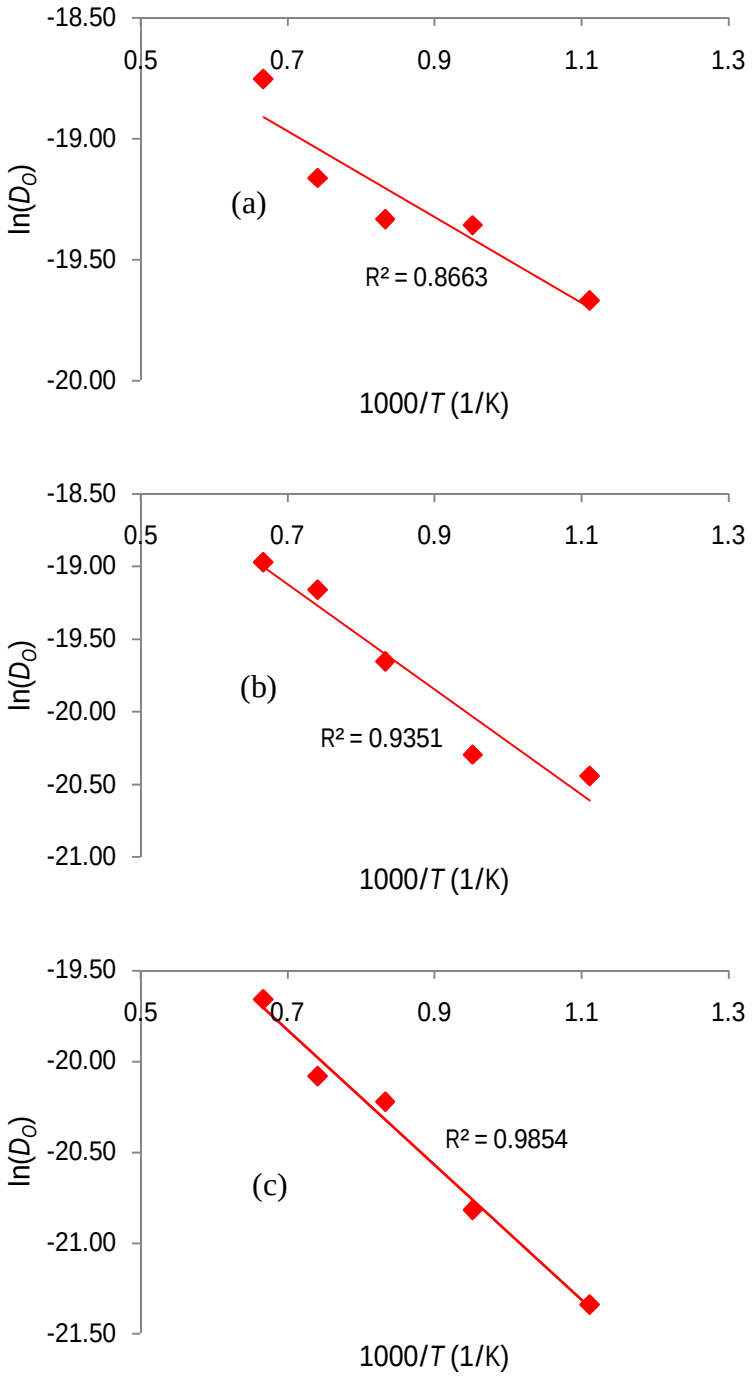

Figure 6.8: Arrhenius plots of 1n (D_O) against 1/T for $SrTiO_3$ cells with different V_O concentrations. (a) 5 % V_O concentration, (b) 3 % V_O concentration and (c) 2 % V_O concentration.

6.6 Conclusions

Using our new potential sets, we have used molecular dynamics simulations to study oxygen diffusion in *c*-$BaTiO_3$ and *c*-$SrTiO_3$. For $BaTiO_3$, we have considered three potential oxygen vacancy charge compensation mechanisms including the reduction of Ti^{4+} to Ti^{3+} ions. Oxygen vacancy concentrations ranging from 2 to 10 % were also tested to provide the best fit to experimental data. For $SrTiO_3$, only the reduction of Ti^{4+} ions was considered as the compensation mechanism in agreement with experimental results. Diffusion coefficients for oxygen were calculated from mean square displacement plots for each charge compensation mechanism and oxygen vacancy concentration over a temperature range of 900 – 1500 K. Arrhenius plots of the diffusion coefficients were then used to calculate the activation energy of oxygen diffusion for these materials.

The calculations for $BaTiO_3$ agreed with the experimentally proven compensation mechanism of Ti^{4+} reduction to Ti^{3+} ions, as this produced the activation energy most comparable to experimental values. The lowest oxygen vacancy concentration tested (2 %) gave both the closest diffusion and activation energy data to experiment. As to be expected, the activation energy for oxygen diffusion in $SrTiO_3$ also increased with decreasing oxygen vacancy concentration, although not to the same extent as $BaTiO_3$. It was found that for both perovskites, the diffusion coefficients at lower temperatures (900 - 1050 K) are about an order of magnitude higher than experimental values. Although at higher temperatures (1200 - 1500 K) the agreement is much better, especially for $SrTiO_3$. The agreement for the activation energies with experiment and other simulations is good. However, it can be argued that cells with lower oxygen vacancy concentrations should be tested which should increase the activation energy and thus test the agreement with experiment. Further calculations would therefore need to be completed to probe fully the effects of vacancy concentration.

References

[1] H. -I. Yoo and D. -K. Lee, Physical Chemistry Chemical Physics **5**, 2212 (2003).

[2] T. Oyama, N. Wada and H. Takagi, Physical Review B **82**, 134107 (2010).

[3] T. Baiatu, R. Waser and K. -H. Härdtl, Journal of the American Ceramic Society **73**, 1663 (1990).

[4] R. Waser, T. Baiatu and K. -H. Härdtl, Journal of the American Ceramic Society **73**, 1645 (1990).

[5] Y. Sakabe, Y. Hamaji, H. Sano and N. Wada, Japanese Journal of Applied Physics **41**, 5668 (2002).

[6] S. Shirasaki, H. Yamamura, H. Haneda, K. Kakegawa and J. Moori, Journal of Chemical Physics **73**, 4640 (1980).

[7] J. H. Haeni, P. Irvin, W. Chang, R. Uecker, P. Reiche, Y. L. Li, S. Choudhury, W. Tian, M. E. Hawley, B. Craigo, A. K. Tagantsev, X. Q. Pan, S. K. Streiffer, L. Q. Chen, S. W. Kirchoefer, J. Levy and D. G. Schlom, Nature **430**, 758 (2004).

[8] A. A. Sirenko, C. Bernhard, A. Golnik, A. M. Clark, J. Hao, W. Si and X. X. Xi, Nature **404**, 373 (2000).

[9] A. Kinaci, C. Sevik and T. Cagin, Physical Review B **82**, 115114 (2010).

[10] J. F. Schooley, W. R. Hosler and M. L. Cohen, Physical Review Letters **12**, 474 (1964).

[11] M. J. Akhtar, Z. -U. -N. Akhtar, R. A. Jackson and C. R. A. Catlow, Journal of the American Ceramic Society **78**, 421 (1995).

[12] J. Li, S. Li, F. Liu, M. A. Alim, G. Chen, Journal of Materials Science: Materials in Electronics **14**, 483 (2003).

[13] R. A. De Souza, V. Metlenko, D. Park and T. E. Weirich, Physical Review B **85**, 174109 (2012).

[14] I. Denk, F. Noll and J. Maier, Journal of the American Ceramic Society **80**, 279 (2005).

[15] A. Ohtomo and H. Y. Hwang, Nature **427**, 423 (2004).

[16] K. Szot, W. Speier G. Bihlmayer and R. Waser, Nature Materials **5**, 312 (2006).

[17] S. Shirasaki, H. Haneda, K. Arai and M. Fujimotoi, Journal of Materials Science **22**, 4439 (1987).

[18] M. T. Buscaglia, V. Buscaglia, M Viviani, P. Nanni and M. Hanuskova, Journal of the European Ceramic Society **20**, 1997 (2000).

[19] R. Freer, Journal of Materials Science **15**, 803 (1980).

[20] E. T. Park, P. Nash, J. Wolfenstine, K. C. Goretta and J. L. Routbort, Journal of Materials Research **14**, 523 (1999).

[21] P. Pasierb, S. Komornicki and M. Rekas, Journal of Physics and Chemistry of Solids **60**, 1835 (1999).

[22] C. A. J. Fisher and H. Matsubara, Computational Materials Science **14**, 177 (1999).

[23] P. Raiteri, J. D. Gale and G. Bussi, Journal of Physics: Condensed Matter **23**, 334213 (2011).

[24] M. S. Islam, Solid State Ionics **154**, 75 (2002).

[25] M. Kubo, Y. Oumi, R. Miura, A. Stirling, A. Miyamoto, M. Kawasaki, M. Yoshimoto and H. Koinuma, Physical Review B **56**, 13535 (1997).

[26] T. Oyama, N. Wada and Y. Sakabe, Key Engineering Materials **388**, 269 (2009).

[27] G. V. Lewis, C. R. A. Catlow and R. E. W. Casselton, Journal of the American Ceramic Society **68**, 555 (1985).

[28] M. Schie, A. Marchewka, T. Müller, R. A. De Souza and R. Waser, Journal of Physics: Condensed Matter **24**, 485002 (2012).

[29] J. Carrasco, F. Illas, N. Lopez, E. A. Kotomin, Yu. F. Zhukovskii, R. A. Evarestov, Yu. A. Mastrikov, S. Piskunov and J. Maier, Physical Review B **73**, 064106 (2006).

[30] J. Crawford and P. Jacobs, Journal of Solid State Chemistry **144**, 423 (1999).

[31] M. Atzmon, Physical Review Letters **65**, 2889 (1990).

[32] N. Garimella, *Multicomponent Interdiffusion in Austenitic Ni-, Fe-Ni-base Alloys and Li_2-Ni_3Al Intermetallic for High-temperature Applications* (University of Central Florida, PhD Thesis, 2009).

[33] H. G. Ahmed, *Studies and Modelling of High Temperature Diffusion Processes in Selected High Performance Structural Coating Systems* (University of Northumbria, PhD Thesis, 2010).

[34] R. Newburgh, J. Peidle and W. Rueckner, American Journal of Physics **74**, 478 (2006).

[35] W. Smith and T. R. Forester, Journal of Molecular Graphics **14**, 136 (1996).

[36] A. M. Stoneham, *Ionic Solids at High Temperatures* (World Scientific Publishing, Singapore, 1989).

[37] J. D. Gale and A. L. Rohl, Molecular Simulation **29**, 291 (2003).

[38] C. J. Xiao, Z. X. Li and X. R. Deng, Bulletin of Materials Science **34**, 963 (2011).

[39] Y. He, Thermochimica Acta **419**, 135 (2004).

[40] A. V. Bandura and R. A. Evarestov, Journal of Computational Chemistry **33**, 1554 (2012).

[41] S. Tsunekawa, H. F. J. Watanabe, H. Takei, Physica Status Solidi A **83**, 467 (1984).

[42] D. I. Woodward, I. M. Reaney, G. Y. Yang, E. C. Dickey and C. A. Randall, Applied Physics Letters **84**, 4650 (2004).

[43] M. -H. Lin, J. -F. Chou and H. -Y. Lu, Journal of the European Ceramic Society **20**, 517 (2000).

[44] H. U. Anderson, Journal of the American Ceramic Society **48**, 118 (1965).

[45] G. V. Lewis and C. R. A. Catlow, Journal of Physics and Chemistry of Solids **47**, 89 (1986).

[46] W. Gong, H. Yun, Y.B. Ning, J. E. Greedan, W. R. Datars, C. V. Stager, Journal of Solid State Chemistry **90**, 320 (1991).

[47] K. Xie, N. Umezawa, N. Zhang, P. Reunchan, Y. Zhangab and J. Ye, Energy and Environmental Science **4**, 4211 (2011).

[48] C. Yu, M. L. Scullin, M. Huijben, R. Ramesh and A. Majumdar, Applied Physics Letters **92**, 092118 (2008).

7

Thermodynamics of Vacancies in *h*-$BaTiO_3$

7.1 Introduction

It is not only the cubic close packed perovskite structure (*c*-$BaTiO_3$) that displays useful electrical properties; the high temperature (> 1425 ˚C) hexagonal polymorph (*h*-$BaTiO_3$) also displays interesting and useful electrical properties depending upon the temperature [1-3] and chemical dopants present [4]. Semiconductivity can also be induced in undoped *h*-$BaTiO_3$ and is conventionally represented as a partial reduction of Ti^{4+} to Ti^{3+} ions when samples are prepared at high temperature under inert or reducing conditions [5-6]. Through partial re-oxidation of these samples, 'colossal' permittivity effects can be achieved [5]. Samples prepared in such reducing conditions also result in oxygen deficiency. Both experiment and simulations (including our own calculations) have confirmed the oxygen loss occurs only at face sharing (O1) sites [7-8] as discussed in chapter 4. Such intrinsic defects are crucial in controlling the electrical properties in this semiconducting material as illustrated by recent publications by Natsui *et al.* [6, 9] on the diffusion behaviour of oxygen in *h*-$BaTiO_3$. As is the case with the other polymorphs of $BaTiO_3$, the main focus of research on *h*-$BaTiO_3$ is on doping and in particular, on transition metal doping [10-11]. In general, these doped samples can be prepared in air and are insulators or modest semiconductors; oxygen deficiency at the O1 sites is again a key feature in their formation [12-13], a fact illustrated by figure 7.1 [13]. In some cases, e.g. Ga-doped samples, they exhibit high room temperature permittivity (ε_r > 60) and modest microwave dielectric resonance properties [4].

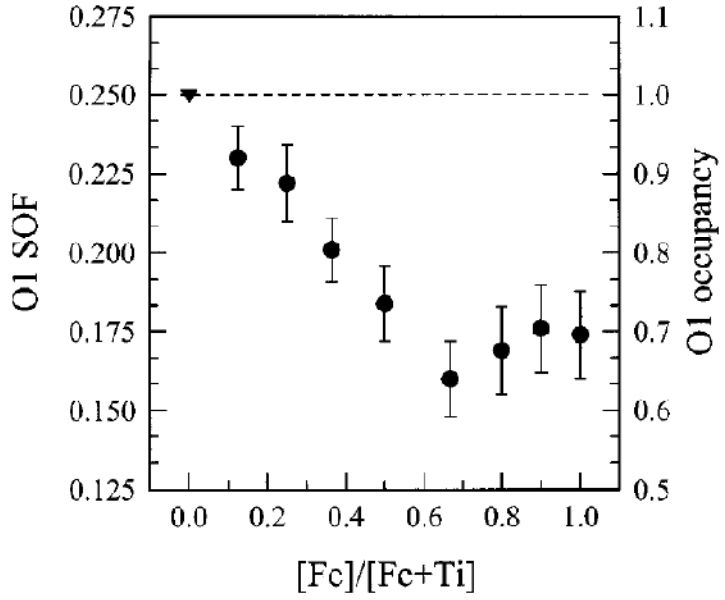

Figure 7.1: Site occupation fractions (SOF) for O1 vs [Fe]/[Fe + Ti] atomic ratio for quenched samples [13] (explicit permission to reuse this image has been granted).

There are a significant number of DFT studies completed on *c*-$BaTiO_3$ [14-17] in the literature; however, there are far fewer DFT studies (or indeed simulation studies) on the hexagonal polymorph. One exception is the work of Colson *et al.* [7] who completed calculations on both the *c*- and *h*- polymorphs and obtained good agreement with experimental structures as well as simulating Ru-doping of the *h*-polymorph at concentrations beyond the dilute limit. Unlike for *h*-$BaTiO_3$, defect formation energies have been derived for intrinsic mono- and di-vacancies using DFT for *c*-$BaTiO_3$ [15], although unlike in this work, the oxygen chemical potential was established using DFT to calculate the total energy of the oxygen dimer directly, whereas ideal gas relations were used for our calculations of the oxygen chemical potential (see section 7.2.1). As previously mentioned, DFT methods have also been used to calculate formation energies for Co-doping in different $BaTiO_3$ polymorphs [18]. To the best of our knowledge no other in-depth study of intrinsic defect thermodynamics in *h*-$BaTiO_3$ exists.

In this chapter, the Zhang-Northrup formalism [19] is used to calculate defect formation energies. In this formalism, the defect formation energy is defined as the difference between the Gibbs free energies of the defective and perfect cell with regard to specific chemical potentials and the contribution of electrons being added and removed. One disadvantage of zero-temperature DFT calculations is the exclusion of entropic and pressure/volume contributions to the Gibbs free energy of each particle. While this is not an issue for solids as these contributions are small, it does present a significant issue for calculations on gaseous particles where such contributions are much larger. This problem can be corrected through the use of ideal gas physics in a method described by Finnis *et al.* [20] and employed more recently for the calculation of defect formation energies for alumina [21]. Through the use of this method, chemical potentials for atomic species, namely oxygen in our case, can be made more accurate through the combination of DFT calculations and standard thermodynamics as well as being defined for a specific temperature and oxygen partial pressure. The Gibbs free energy of a solid can be accurately determined by using the ground-state total energy obtained from DFT calculations.

The aim of this chapter is to determine accurate formation energies for the native defects of *h*-$BaTiO_3$. In addition to Ba (V_{Ba}), Ti (V_{Ti}) and O (V_O) mono-vacancies, Ti-O (V_{Ti} - V_O) and Ba-O (V_{Ba} - V_O) di-vacancies have also been considered, including the binding energies of such di-vacancies. Finite-size scaling and band gap corrections have also been applied. The results show a large difference in energy between these defects and this is reflected in the calculated concentrations of each vacancy type and possible vacancy site. Such results will enable quantitative comparison both with experiment and with previous results calculated for *c*-$BaTiO_3$ [15].

7.2 Method

7.2.1 Defect Formation Energy Calculations

In the Zhang-Northrup formalism [19] we begin with a supercell of the crystal. It is assumed that this supercell is in equilibrium with a reservoir of the constituent atomic species (α) and a reservoir of electrons. The chemical potentials of these atomic species (μ_α) and the electrons (μ_e) are treated as equal to those in the supercell. The formation energy (ΔE_f) can then be obtained by comparing the Gibbs free energy of the supercell and the Gibbs free energy of the defective supercell with respect to the electrons added or removed as well as the chemical potentials of the atomic species. In order to create a vacancy in the perfect supercell, an atom of element (α) must be added or removed. The defect formation energy of a defect in charge state q, can be calculated with respect to chemical potentials and the Fermi level,

$$\Delta E_f = (E_T^{def,q} - E_T^{perf}) + q(E_{VBM} + E_F) - \sum_i \Delta n_i \mu_i \tag{7.1}$$

where $E_T^{def,q}$ is the total energy of the defective system and E_T^{perf} is the total energy of the perfect reference cell. The dependence upon the Fermi level, E_F, is given in the second term and E_{VBM} is the position of the valence band maximum (VBM). In this equation, E_F takes a value between 0 and E_g, where E_g is the band gap of the material. The final term defines the contribution of the chemical potentials of each atomic species, Δn_i is the number of atoms of element i removed or added to create the defect, μ_i represents the chemical potential of element i and is the sum of the chemical potentials of the reference state and the chosen chemical environment (as calculated by equations (7.3) – (7.5) below). The chemical potential of the reference state for an element is equivalent to its calculated total free energy per atom (see section 7.3.1). It is noteworthy to add configurational entropy is neglected here because we are only concerned with the dilute limit.

From the calculation of defect formation energies, the concentration of that defect in equilibrium (see section 2.7.1) at a particular temperature can be obtained [22],

$$c = c_0 \exp\left(\frac{-\Delta E_f}{k_B T}\right) \tag{7.2}$$

where c_0 is the concentration of possible defect sites, k_B is the Boltzmann constant and T is the temperature. These values can enable quantitative comparison with experiment and in the case of *h*-$BaTiO_3$ an insight into preferred vacancy sites is provided.

For defect formation energy calculations it is essential that chemical potentials are calculated to establish the thermodynamic boundaries of the system. As discussed in the introduction, the small temperature and pressure dependence of the chemical potential per unit cell of a solid (e.g. Ba, Ti) can be neglected. This allows the use of T = 0 K total energy calculations for these atomic species and the bulk crystal (as well as its formation energy) to define thermodynamic reservoirs where the chemical potentials of the individual atoms cannot exceed the formation enthalpy of the crystal.

$$\mu_{\mathrm{Ba}} + \mu_{\mathrm{Ti}} + 3\mu_{\mathrm{O}} = \Delta H_f[\mathrm{BaTiO_3}], \tag{7.3}$$

In addition to this requirement, further constraints come from the formation of competing compounds.

$$\mu_{\mathrm{Ba}} + \mu_{\mathrm{O}} \leq \Delta H_f[\mathrm{BaO}], \tag{7.4}$$

$$\mu_{\mathrm{Ti}} + 2\mu_{\mathrm{O}} \leq \Delta H_f[\mathrm{TiO_2}], \tag{7.5}$$

The combination of these equations confines the values of the chemical potentials of the atomic species to the stability range of $BaTiO_3$.

While it is acceptable to use T = 0 K total energy calculations to define thermodynamic boundaries for solids, the chemical potential of gaseous oxygen, as discussed, has a far stronger dependence upon temperature and pressure. Furthermore, the choice of functional and pseudopotentials in calculating μ_{O} results in significant error due to the inaccuracies of DFT in simulating the oxygen dimer as discussed by Hine *et al.* [21]. We have used a method developed by Finnis *et al.* [20] to avoid calculating μ_{O} directly from DFT calculations. By using the experimental formation energy of $BaTiO_3$ and T = 0 K total energy calculations for Ba and Ti, the oxygen

chemical potential at standard pressure and temperature, $\mu_O(p^0_{O_2}, T^0)$, can be determined without the need for direct calculation. Through the use of ideal gas relations and $\mu_O(p^0_{O_2}, T^0)$, the oxygen chemical potential can be derived for a specific temperature and pressure, $\mu_O(p_{O_2}, T)$. The reliability of this approach has been confirmed by comparison to thermodynamic data [23]. The value of $\mu_O(p_{O_2}, T)$ for a specific temperature and pressure is obtained from the ideal gas expression and a formula for an ideal gas of rigid dumbbells [23].

$$\mu_O(p_{O_2}, T) = \frac{1}{3}\left(\mu_{BaTiO_3} - \mu_{Ba} - \mu_{Ti} - \Delta G_f^{BaTiO_3}\right) + \Delta\mu(T) + \frac{1}{2}k_B T \ln\left(\frac{p_{O_2}}{p^0_{O_2}}\right) \tag{7.6}$$

The temperature contribution $\Delta\mu(T)$, is represented by,

$$\Delta\mu(T) = E_0 + \left(\mu^0_{O_2} - E_0\right)\left(\frac{T}{T^0}\right) - C_P T \ln\left(\frac{T}{T^0}\right) \tag{7.7}$$

where E_0 is the energy per oxygen molecule at 0 K and C_P is the specific heat per molecule at constant pressure ($5k_B/2$ [24]). Further details on this methodology and the calculation of E_0 can be found in [23].

For the results reported here, a temperature of 1698 K and an oxygen partial pressure of 1 atm have been used to calculate $\mu_O(p_{O_2}, T)$ in accordance with the experimental polymorphic phase transition conditions of *c*- to *h*-$BaTiO_3$.

7.2.2 Finite-size Corrections

One disadvantage of these types of DFT calculation is the spurious defect-defect interactions that occur between periodic images, with the magnitude being very much dependent on the charge of the defect and the size and shape of the supercell [25-26]. Elastic interactions are the main source of error for neutral defects. These interactions scale inversely to supercell volume, L^{-3}, where L is the length of the supercell, and

hence are dealt with inherently by the finite-size scaling extrapolation process. For charged defects, electrostatic interactions can be corrected by a multipole expansion as presented by Makov and Payne [27]. The first term in this expression concerns monopole-monopole interactions and scales as L^{-1}. This correction can be determined with prior knowledge of the static dielectric constant of the crystal, ε, and the Madelung constant of the supercell, α,

$$\Delta E_{\mathrm{mp}} = -\frac{q^2\alpha}{2L\varepsilon}, \tag{7.8}$$

First-principles calculations produced a value of ε = 57 for barium titanate [28] and this value is used in the present work. The next term in the multipole expansion relates to monopole-dipole interactions. Similarly to the elastic interactions, this scales with L^{-3} and can therefore also be accounted for by the finite-size scaling procedure. The results of this procedure generally produced small extrapolation errors, as shown by tables 7.1 and 7.2. For strongly charged defects such as Ti vacancies, quadrupole and higher terms may become important. However, they have not been considered here. It should be noted that alternate methods of calculating finite-size corrections are available [29].

7.2.3 Band Gap Corrections

Another shortcoming of these DFT calculations is that the value of the valence band energy (E_{VB}) calculated for the bulk cannot be applied to the supercell with the charged defect because of the shift in the electrostatic potential the defect causes [29-30]. To account for this problem, we use the same approach that was used by Erhart and Albe [15] for *c*-$BaTiO_3$. This method shifts the valence band (ΔE_{VB}) and the conduction band (ΔE_{CB}) with respect to each other so that the correction energy is obtained from: -

$$\Delta E_{bg} = n_e \Delta E_{\mathrm{CB}} + n_h \Delta E_{\mathrm{VB}}, \tag{7.9}$$

where n_e and n_h represent the number of electrons occupying conduction band states and the number of holes occupying valence band states, respectively. A T = 0 K a band gap of 3.4 eV derived from extrapolation of higher temperature data [31] was used to

correct for the underestimation of the band gap while assuming that the offset of the calculated band structure is restricted to the conduction band i.e. $\Delta E_{\mathrm{VB}} = 0$ and $\Delta E_{\mathrm{CB}} =$ 3.4 eV - E_G^{calc}. Such corrections only affect oxygen vacancies and di-vacancies in charge states below their full ionic values i.e. $V_O^{\cdot,0}$, $V_{Ti}^{\prime\prime\prime,\prime\prime\prime\prime} - V_O$ and $V_{Ba}^{\prime} - V_O$. Furthermore, these defects already have significantly higher formation energies than the equivalent defect in its nominal charge state over the majority of the band gap (see section 7.3.3) and the band gap corrections succeed in only further increasing these defect formation energies.

7.2.4 DFT Calculation Details

The calculations in this work were performed using the Vienna *Ab initio* simulation package (VASP) [32] with the local density approximation (LDA) [33-34] and projector augmented-wave method [35-36]. The LDA was chosen to provide consistency with results previously obtained for the cubic polymorph of $BaTiO_3$ [15]. For greater accuracy, the 3*s* and 3*p* electrons of the Ti atoms were included in the valence electrons for all calculations. Defect formation energies were calculated using the *h*-$BaTiO_3$ 30 atom unit cell as well as 60 (2 X 1 X 1) and 120 (2 X 2 X 1) atom supercells. A full description of the finite-size extrapolation procedure is given in section 7.2.2. A Γ-point centred 4 X 4 X 3 *k*-point mesh was used for Brillouin zone integration for the 30 and 60 atom cells and a 3 X 3 X 2 mesh for the 120 atom cells. A plane wave cutoff energy of 500 eV was applied for all defect calculations. In the case of charged defects, a neutralising background charge was used to preserve cell neutrality.

7.3 Thermodynamics of Vacancies in *h*-$BaTiO_3$

7.3.1 Bulk Properties of *h*-$BaTiO_3$

The thermodynamic boundaries (as described in section 7.2.1) are defined by the calculated bulk properties of *h*-$BaTiO_3$ and its constituent elements/compounds in their

standard states. All bulk property calculations were completed using a Γ-point centred 13 X 13 X 13 *k*-point mesh and were fully converged to an accuracy greater than 1 meV per unit cell. A plane wave cutoff energy of 600 eV was also used.

A lattice constant of 4.77 Å and a total energy of -2.24 eV/atom were calculated for bcc cubic Ba. These values agree reasonably well with the experimental equivalents of 5.03 Å [37] and a cohesive energy of -1.90 eV [38]. Ti has a hcp structure with calculated lattice constants of a = 2.86 Å and c = 4.54 Å (compared to experimental values of a = 2.95 and c = 4.69 Å [39]) and a total energy of - 8.54 eV (compared to an experimental cohesive energy of -4.85 eV [38]). The overbinding associated with LDA [40] explains the gross overestimation of the cohesive energy of Ti.

Barium oxide (BaO) has the rock salt structure ($Fm\bar{3}m$, space group number 225) with a lattice constant of 5.54 Å [41] and an enthalpy of formation of -5.68 eV [42]. DFT calculations produce a lattice constant of 3.28 Å and an enthalpy of formation of -5.01 eV for BaO. Rutile TiO_2 ($P4_2/mnm$, space group number 136) has lattice constants of a = 4.59 and c = 2.96 Å [43] and an enthalpy of formation of -9.78 eV [42], in comparison to calculated values of a = 4.56 and c = 2.92 Å and an enthalpy of formation of -10.09 eV. For *h*-$BaTiO_3$ ($P6_3/mmc$, space group number 194), lattice constants of a = 5.66 and c = 13.80 Å were calculated which agree well with experimental values of a = 5.72 and c = 13.96 Å [44]. There is also excellent agreement between the calculated and experimental enthalpy of formation energies, an experimental value of 17.20 eV [45] and a calculated value of 17.19 eV. In general there is good agreement between the experimental and calculated properties of the bulk materials, however, the tendency of LDA calculations to underestimate lattice constants is clear, particularly in the cases of BaO and Ba.

7.3.2 Defect Structures

All possible mono-vacancies were considered in *h*-$BaTiO_3$: this includes both possible sites for each vacancy and selected di-vacancies. Di-vacancies associated with the Ba2 atoms and Ti2 atoms located in the Ti_2O_9 dimers of *h*-$BaTiO_3$ were chosen because of

the strong binding behaviour between these sites and oxygen vacancies and because of the preference for the formation of these defects over Ba1 and Ti1 vacancies, respectively, as discussed in chapter 4. Multiple charge states were investigated for all types of vacancies. Figure 7.2 shows the relaxed cell geometries for the most favourable mono-vacancies in their nominal charge state.

The introduction of a face-sharing O1 vacancy (figure 7.2(b)) to the system causes the neighbouring O1 atoms to relax inwards, while the neighbouring Ti2 atoms move away from the newly formed 2+ charged site towards the layers of O2 atoms to accommodate the loss of attraction from the loss of the O1 atom. As expected the opposite occurs for the Ti2 vacancy (figure 7.2(c)): here O1 atoms are forced away from the 4- vacancy site, whereas the surrounding Ti and Ba atoms relax towards the vacancy site. Similar relaxations were observed in DFT calculations on vacancies in anatase TiO_2 [46]. For V''_{Ba2} the local relaxations are not as pronounced due to the reduced charge density of a large Ba atom compared to a Ti atom. However, there is a small movement of the nearest Ba2 and Ti2 atoms towards the vacancy site (figure 7.2(d)).

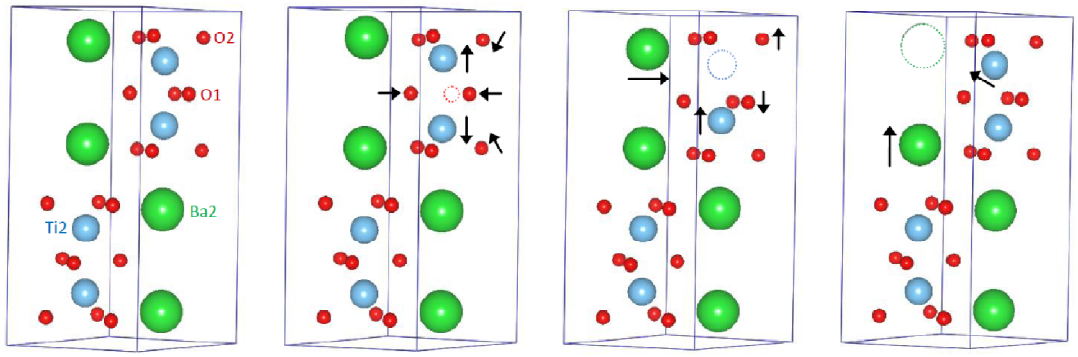

Figure 7.2: Relaxed cell geometries for (a) - bulk *h*-$BaTiO_3$ and (b) - $V^{\cdot\cdot}_{O1}$, (c) - V''''_{Ti2}, (d) - V''_{Ba2} defects. Vacancy positions are shown by dashed circles and arrows denote the direction of relaxation for atoms neighbouring the vacancy. Atoms on the cell boundary (i.e. Ti1 and Ba1) and bonds have been omitted for clarity [47] (explicit permission to reuse this image has been granted).

7.3.3 Defect Formation Energies

The results for the calculated defect formation energies for three different combinations of chemical potentials and with a Fermi level at the valence band maximum are presented in tables 7.1 and 7.2. For each vacancy type, the lowest energy vacancy (and hence most prominent) is plotted as a function of the Fermi level in figure 7.3. The values in figure 7.3 refer to a μ_O value calculated at the formation temperature of *h*-$BaTiO_3$, 1698 K, and an oxygen partial pressure of 1 atm. Only the energies of the vacancies in their nominal charge states (V_{Ti}'''', $V_O^{\cdot\cdot}$, V_{Ba}'', $V_{Ti}'' - V_O$ and $V_{Ba}^0 - V_O$) are plotted because for all vacancies, other charge states occupy a small part of the band gap or do not exist in the band gap at all. Examples of the finite-size extrapolation error calculations are given for types of defect in figure 7.4.

For O vacancies, there is a clear preference for face-sharing O1 vacancies over corner-sharing O2 vacancies. This observation is supported by our and other simulations [7] and by experiment [8, 48], where no evidence of O2 vacancies is reported for either doped or undoped *h*-$BaTiO_3$. At the metal-rich limit, oxygen vacancies dominate over the entire band gap with negative formation energies and hence are the most abundant defect. It is noteworthy that only at the conduction band minimum (CBM) does the formation energy reach 0 eV. This suggests that under these conditions stoichiometric *h*-$BaTiO_3$ cannot form and that oxygen vacancies must always be present. This observation is confirmed by experiment, where under low p_{O_2} (metal-rich) conditions oxygen deficient *h*-$BaTiO_3$ forms and re-oxidation is necessary to re-form the stoichiometric material [8]. The formation energies of both O1 and O2 vacancies are also considerably lower than the value found for *c*-$BaTiO_3$, where a value of -5.07 eV in metal-rich conditions was obtained [15]. This is partly supported by previous calculations in chapter 4, where the vacancy formation energy from lattice statics calculations for O1 in *h*-$BaTiO_3$ was lower than for an O vacancy in *c*-$BaTiO_3$, but this in turn was lower than the vacancy energy for an O2 atom. The most likely reason for this discrepancy is the different approaches taken in calculating μ_O in this work and in the work by Erhart and Albe [15]. If the temperature dependence of μ_O had been taken into account in the previous work, the formation energy of an O vacancy in

c-$BaTiO_3$ would undoubtedly have been lower. Additional error may also arise from the fact that static vacancy energy calculations do not take into account the chemical environment of the defect which makes direct comparison difficult. Under O-rich conditions, O1 vacancies only dominate in a section of the lower half of the band gap (a *p*-type material).

Unlike O vacancies, neither Ti1 nor Ti2 vacancies ever reach negative formation energies under any combination of chemical potentials at the VBM. This is to be expected because of the difficulty in removing an ion with a high charge density such as Ti^{4+} from an ionic system. In DFT calculations by Moriwake *et al.* [49] on *c*-$BaTiO_3$, Ti vacancies are not observed in any chemical environment, although this is almost certainly a result of the fact that only neutral defects were considered. High Ti vacancy energies in both *c*- and *h*-$BaTiO_3$ have also been found using potential-based methods as shown in chapter 4. Regardless of this, Ti vacancies (and in particular Ti2 vacancies) dominate in O-rich conditions in the top half of the band gap (an *n*-type material). Again, good agreement is achieved with lattice statics calculations as the Ti vacancy formation energies published here are higher than those for the cubic phase [15], which is also true for the classical calculations. It should be noted that Ba-site doping with trivalent lanthanides such as La in *c*-$BaTiO_3$ does produce a substantial solid solution (~25 at%) where the compensation mechanism is the formation of Ti-vacancies, i.e. $Ba_{1-x}La_xTi_{1-x/4}O_3$ with $0 \leq x \leq 0.25$ [50].

The results for the formation energy of Ba vacancies suggest that for the majority of the band gap it is not the dominant species, either in metal-rich or O-rich conditions (although the magnitude of the formation energies is reasonable with respect to the other vacancy types). Figure 7.3 shows that for only a small portion of the band gap (E_F = ~1.6 to 2.1 eV) in O-rich (Ba deficient) conditions does the Ba2 vacancy species become the dominant defect in the material. This may seem surprising considering the energetic penalty of removing a highly charged Ti vacancy. However, unlike a V_{Ti}'''', a Ba vacancy does not have such a strong dependence on the Fermi level (2- charge compared to a 4- charge), that allows Ti vacancies to dominate in the top half of the band gap. Furthermore, calculations on the cubic polymorph also showed only a small

area of the band gap in a similar chemical environment where Ba vacancies are the predominant defect [15] and previous calculations suggest Ba vacancies in *h*-$BaTiO_3$ are less favourable than in *c*-$BaTiO_3$. Direct comparison with experiment is difficult for $BaTiO_3$, as Ba and Ti vacancy abundances are measured in doped samples where the concentrations of such vacancies are strongly influenced by the nature of the dopant species [51].

Given the strong Coulombic interaction between point defects in $BaTiO_3$, it is necessary to consider the formation of defect pairs between negatively charged metal vacancies and positively charged oxygen vacancies. The binding energy (E_b) of such a defect pair gives an insight into whether the defects prefer to pair or remain isolated. The binding energy of a defect pair/complex is calculated by,

$$E_b = E_f(X) + E_f(Y) - E_f(XY) \tag{7.10}$$

where $E_f(X)$ and $E_f(Y)$ are the formation energies of the constituents and $E_f(XY)$ is the formation energy of the binding pair. The binding energy is independent of chemical potentials and a negative value suggests that the defect pair will readily form. Binding energies of -0.35 eV and -0.08 eV were calculated for $V_{Ba2}^0 - V_{O1}$ and $V_{Ba2}^0 - V_{O2}$, respectively. For the Ti vacancy pairs, binding energies of -0.25 eV and -1.01 eV were observed for $V_{Ti2}'' - V_{O1}$ and $V_{Ti2}'' - V_{O2}$, respectively. This clearly suggests that defect pairs will readily form where possible, with $V_{Ti2}'' - V_{O2}$ and $V_{Ba2}^0 - V_{O1}$ di-vacancies having the energetic preference, although, as previously discussed, in reality the presence of V_{O2} defects has not been observed experimentally. Erhart and Albe [15] obtained significantly stronger binding energies of -0.62 eV and -1.93 eV for the equivalent Ba-O and Ti-O di-vacancies in the cubic structure. The proposed reason for the greater Ti-O binding in the cubic polymorph is that for these types of di-vacancies in *h*-$BaTiO_3$, there is competition between the attraction of the negatively charged V_{Ti2} with both the positively charged V_O and the neighbouring Ti2 atom. This scenario does not exist for *c*-$BaTiO_3$ as all Ti atoms are separated by 4.01 Å and hence the Coulombic attraction is not as strong. In the case of the $V_{Ti2}'' - V_O$ di-vacancy, there is also increased strain because of the close proximity of surrounding O1 and O2 atoms which

are attracted to V_{O1}, but experience repulsion from the binding V_{Ti2} resulting in less favourable binding behaviour. A similar explanation can also account for the difference in the Ba-O binding energies between the two polymorphs as Ba atoms are also separated by ~ 4 Å in the cubic polymorph. As proposed in [15], it is most likely that oxygen vacancies bind to the immobile metal vacancies as they diffuse through the system.

Defect	q	$n_{e,h}$	E_f (eV) (Metal-rich)	E_f (eV) (O-rich)[1]	E_f (eV) (O-rich)[2]	Error (eV)
V_{O1}	0	-2	1.77	6.14	6.14	(0.19)
	+1	-1	-2.60	1.77	1.77	(0.11)
	+2	0	-6.80	-2.43	-2.43	(0.07)
V_{O2}	0	-2	2.55	6.92	6.92	(0.14)
	+1	-1	-1.82	2.55	2.55	(0.05)
	+2	0	-6.03	-1.66	-1.66	(0.12)
V_{Ba1}	-2	0	10.47	4.73	6.54	(0.20)
	-1	+1	9.82	4.08	5.89	(0.14)
	0	+2	9.22	3.48	5.29	(0.02)
V_{Ba2}	-2	0	10.21	4.47	6.28	(0.09)
	-1	+1	9.63	3.89	5.70	(0.02)
	0	+2	9.04	3.30	5.11	(0.14)
V_{Ti1}	-4	0	17.50	10.13	8.04	(0.35)
	-3	+1	17.00	9.63	7.54	(0.33)
	-2	+2	16.45	9.08	6.99	(0.23)
	-1	+3	15.92	8.55	6.46	(0.11)
	0	+4	15.37	8.00	5.91	(0.11)
V_{Ti2}	-4	0	16.25	8.88	6.79	(0.27)
	-3	+1	15.74	8.37	6.28	(0.30)
	-2	+2	15.27	7.9	5.81	(0.21)
	-1	+3	14.73	7.36	5.27	(0.08)
	0	+4	14.24	6.87	4.78	(0.09)

[1]Where $\Delta\mu_{\mathrm{Ba}}$ is at the maximum negative value defined by equations (7.4) and (7.5).

[2]Where $\Delta\mu_{\mathrm{Ti}}$ is at the maximum negative value defined by equations (7.4) and (7.5).

Table 7.1: Formation energies of mono-vacancies in *h*-$BaTiO_3$ under metal-rich and O-rich conditions at T = 1698 K, p_{O_2} = 1 atm and with the Fermi level at the valence band maximum (E_F = 0 in equation (7.1)). Values relevant to the band gap correction (equation (7.9)) are given in the third column. The finite-size extrapolation error is given in the final column.

Defect	q	$n_{e,h}$	E_f (eV) (Metal-rich)	E_f (eV) (O-rich)[1]	E_f (eV) (O-rich)[2]	Error (eV)
V_{Ba2} - V_{O1}	-1	-1	7.39	6.02	8.11	(0.17)
	0	0	3.06	1.69	3.78	(0.07)
	+1	+1	2.31	0.94	3.03	(0.09)
V_{Ba2} - V_{O2}	-1	-1	8.39	7.02	9.11	(0.23)
	0	0	4.10	2.73	4.82	(0.14)
	+1	+1	3.49	2.12	4.21	(0.13)
V_{Ti2} - V_{O1}	-3	-1	13.37	10.37	8.28	(0.12)
	-2	0	9.20	6.20	4.11	(0.16)
	-1	+1	8.62	5.62	3.53	(0.08)
	0	+2	8.03	5.03	2.94	(0.06)
	+1	+3	7.44	4.44	2.35	(0.17)
V_{Ti2} - V_{O2}	-3	-1	13.32	10.32	8.23	(0.22)
	-2	0	9.21	6.21	4.12	(0.31)
	-1	+1	8.45	5.45	3.36	(0.24)
	0	+2	7.83	4.83	2.74	(0.07)
	+1	+3	7.21	4.21	2.12	(0.09)

[1]Where $\Delta\mu_{\mathrm{Ba}}$ is at the maximum negative value defined by equations (7.4) and (7.5).

[2]Where $\Delta\mu_{\mathrm{Ti}}$ is at the maximum negative value defined by equations (7.4) and (7.5).

Table 7.2: Formation energies of di-vacancies in *h*-$BaTiO_3$ under metal-rich and O-rich conditions at T = 1698 K, p_{O_2} = 1 atm and with the Fermi level at the valence band maximum (E_F = 0 in equation (7.1)). Values relevant to the band gap correction (equation (7.9)) are given in the third column. The finite-size extrapolation error is given in the final column.

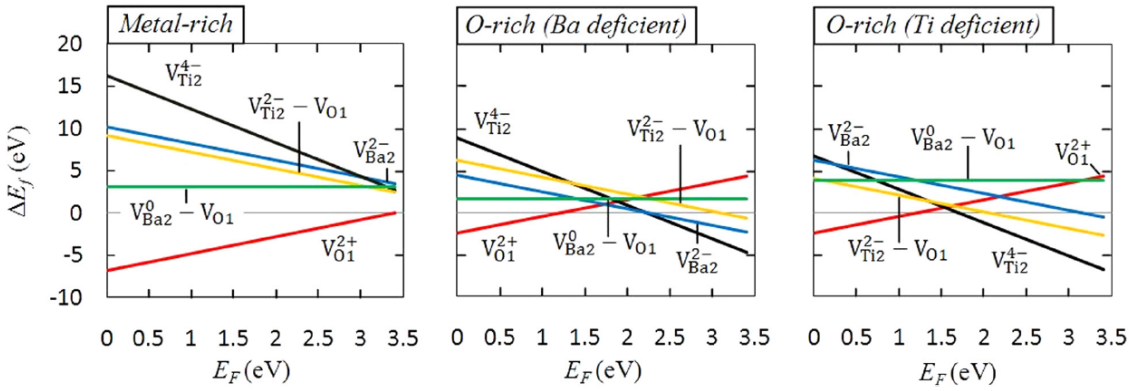

Figure 7.3: Variation of calculated defect formation energies of the lowest energy vacancy types in *h*-$BaTiO_3$ with Fermi level energy (E_F). Formation energies refer to the defect in its nominal charge state. The calculation of μ_O was performed at T = 1698 K and p_{O_2} = 1 atm [47] (explicit permission to reuse this image has been granted).

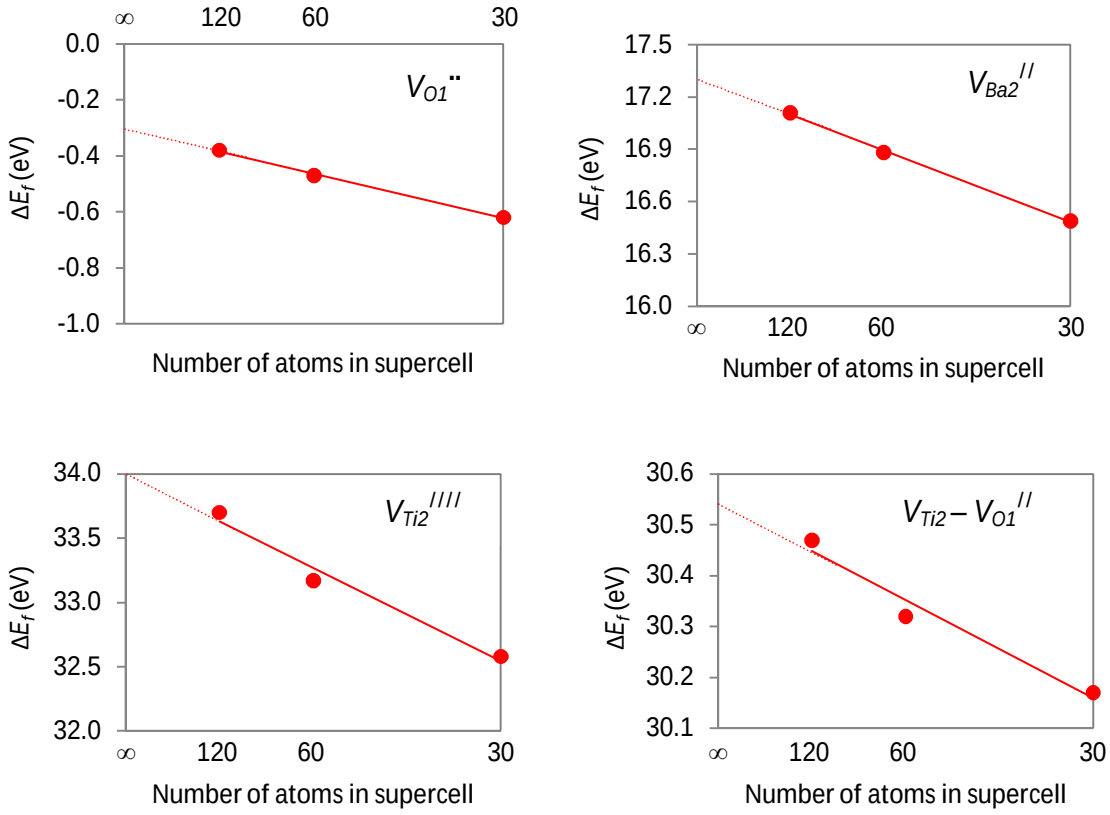

Figure 7.4: Finite-size extrapolations for a series of defects in their nominal charge state in *h*-$BaTiO_3$.

7.3.4 Defect Concentrations

By using the calculated defect formation energies at a specific combination of chemical potentials, the equilibrium defect concentrations can be calculated using equation 7.2. The concentrations of the most common defects at a range of temperatures in both Ba- and Ti-deficient environments are given in figure 7.5. The concentrations are calculated at the Fermi level pinning energy (1.22 eV), this value represents the point at which the Fermi level of the material cannot be closer to the valence band as the formation energy of certain defects becomes negative meaning that the stoichiometric material is not stable. Metal-rich conditions are not considered as the high formation energies of metal vacancies in this environment means that the concentrations will be negligible for most values of the Fermi energy. O vacancies are also omitted, as at the Fermi level pinning energy their formation energies are very low and will hence be very high in concentration and will always be the dominant defect.

At the pinning energy and under Ba-deficient conditions, titanium mono- and di-vacancies are low in concentration, with di-vacancies being preferred (~7.0 x 10^{10} cm^{-3} for V_{Ti2} - V_{O1} at 1698 K compared to ~1.3 x 10^{10} cm^{-3} for V_{Ti2} at the same temperature). Conversely, Ba mono- and di-vacancies are significantly higher in concentration. V_{Ba2} - V_{O1} shows the highest concentration for metal vacancies in Ba-deficient conditions with a concentration of ~9.7 x 10^{16} cm^{-3} at 1698 K, an order of magnitude more than the second most important defect, V_{Ba2}. These vacancy concentrations are only valid for the undoped material as cation vacancies are often involved in compensating donor-doped systems and will hence exist in higher concentrations in such doped systems [52-53].

In Ti-deficient conditions, the V_{Ti2} - V_{O1} di-vacancy pair is the commonest metal defect in the system. The concentration of these di-vacancies proves that where possible metal vacancies will preferentially bind to oxygen vacancies to lower the internal energy of the crystal. This is also confirmed by a molecular dynamics study on doped $BaTiO_3$, where diffusion of V_O is inhibited by its Coulombic attraction to cation vacancies [54]. Mono-titanium vacancies are also present in significant concentrations, while other defects are only present in far smaller concentrations.

These results have been confirmed by experiment and thermodynamics calculations for both the cubic and hexagonal polymorphs of $BaTiO_3$ [55-56]. Lee *et al.* [56] showed using XRD and by studying the phase transition temperature variation with respect to the Ba/Ti ratio that a greater solubility limit exists under Ba-rich (Ti-deficient) conditions than previously thought in addition to the already known solubility limit of the Ti-rich (Ba-deficient) side. This solubility in both Ba- and Ti-rich conditions suggests that both Ba and Ti metal vacancies are likely and that they will exist as partial-Schottky defects (V_{Ba} - V_O and V_{Ti} - $2V_O$) in the system, a finding confirmed by thermodynamic theory [56].

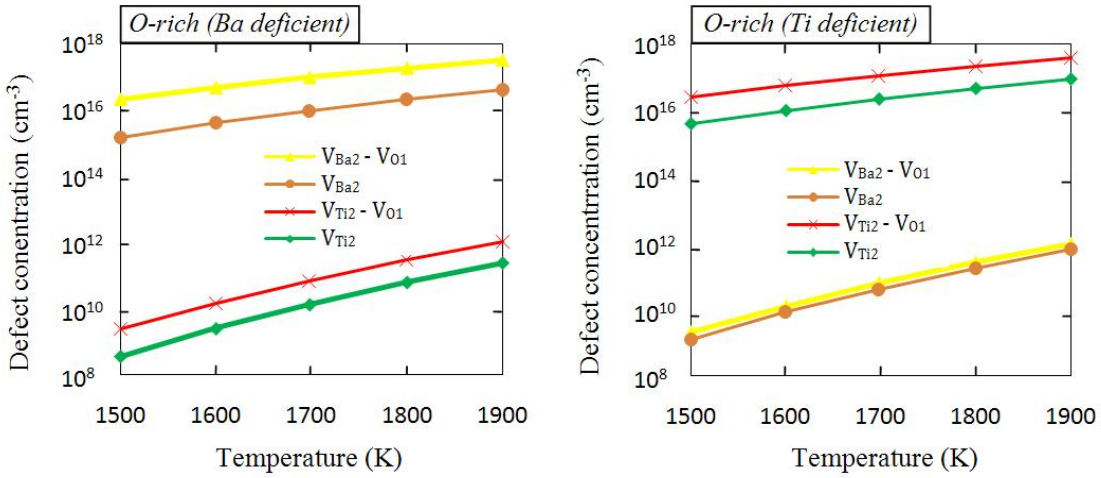

Figure 7.5: Defect concentrations of V_{Ti2}, V_{Ba2}, V_{Ti2} - V_{O1} and V_{Ba2} - V_{O1} in their nominal charge states for temperatures in the range 1500 – 1900 K at the Fermi level pinning energy (1.22 eV) in *h*-$BaTiO_3$ [47] (explicit permission to reuse this image has been granted).

7.4 Conclusions

In this chapter, we have used density functional theory calculations to complete an extensive study of vacancies in *h*-$BaTiO_3$. All possible mono-vacancies have been considered as well as metal-oxygen di-vacancies. Multiple charge states have been considered for all of the vacancies. Defect formation energies have been calculated using the Zhang-Northrup formalism [19] with necessary consideration given to the errors arising from the supercell approach and from the error associated with the calculation of the band-gap in DFT studies. The method of Finnis, Lozovoi and Alavi [20] has also been used for the calculation of the oxygen chemical potential to reduce inaccuracies arising from the direct calculation of the oxygen dimer. Equilibrium defect concentrations are derived from formation energies for a range of temperatures.

The calculations confirmed that all types of vacancies studied exist in their nominal charge state over the majority of the band gap and that generally V_{O1} is the dominant defect in the system in accordance with experiment and previous calculations. Under reducing conditions, the formation energy of V_{O1} remains negative for all values of the Fermi level up to the conduction band minimum. This suggests that under such a low oxygen partial pressure, stoichiometry cannot exist in the system, a finding supported by experiment. For oxygen-rich conditions, V_{O1} again dominates in the lower half of the band gap, while in the upper half metal di-vacancies are the most prevalent defects. Binding energies calculated for the V_{Ba} - V_O and V_{Ti} - V_O pairs suggest that these di-vacancies will readily form by the 'capture' of a mobile oxygen vacancy by a metal vacancy. Mono-metal vacancy concentrations are exceeded by di-vacancies concentrations, with the highest concentrated defects being V_{Ba2} - V_{O1} (~9.7 x 10^{16} cm^{-3} (1698 K)) for a Ba-deficient environment and V_{Ti2} - V_{O1} (~1.1 x 10^{17} cm^{-3} (1698 K) for a Ti-deficient environment, as supported by experiment. Excellent agreement has also been observed with previous lattice statics calculations presented in chapter 4 and with DFT calculations on the cubic polymorph of $BaTiO_3$.

References

[1] M. Yamaguchi, K. Inoue, T. Yagi and Y. Akishige, Physical Review Letters **74**, 2126 (1995).

[2] M. Yamaguchi, M. Watanabe, K. Inoue, Y. Akishige, and T. Yagi, Physical Review Letters **75**, 1399 (1995).

[3] K. Inoue, A. Hasegawa and K. Watanabe, H. Yamaguchi, H. Uwe and T. Sakudo, Physical Review B **38**, 6532 (1988).

[4] A. Feteira, K. Sarma, N. Mc. Alford, I. M. Reaney and D. C. Sinclair, Journal of the American Ceramic Society **86**, 511 (2003).

[5] J. Yu, T. Ishikawa, Y. Arai, S. Yoda, M. Itoh and Y. Saita, Applied Physics Letters **87**, 252904 (2005).

[6] H. Natsui, J. Yu, S. Hashimoto, M. Itoh, O. Odawara and S. Yoda, Ferroelectrics **415**, 122 (2011).

[7] T. A. Colson, M. J. S. Spencer and I. Yarovsky, Computational Materials Science **34**, 157 (2005).

[8] D. C. Sinclair, J. M. S. Skakle, F. D. Morrison, R. I. Smith and T. P. Beales, Journal of Materials Chemistry **6**, 1327 (1999).

[9] H. Natsui, J. Yu, S. Hashimoto, M. Itoh, O. Odawara and S. Yoda, Ferroelectrics **403**, 225 (2010).

[10] N. Maso, H. Beltran, E. Cordoncillo, P. Escribano and A. R. West, Journal of Materials Chemistry **16**, 1626 (2006).

[11] H. J. Hagemann and H. Ihrig, Physical Review B **20**, 3871 (1979).

[12] L. Miranda, A. Feteira, D. C. Sinclair, K. Boulahya, M. Hernando, J. Ramfrez, A. Varela, J. M. Gonzalez-Calbet and M. Parras, Chemistry of Materials **21**, 1731 (2009).

[13] I. E. Grey, C. Li, L. M. D. Cranswich, R. S. Roth, T. A. Vanderah, Journal of Solid State Chemistry **135**, 312 (1998).

[14] Z. -X. Chen, Y. Chen and Y. -S. Jiang, Journal of Physical Chemistry B **105**, 5766 (2001).

[15] P. Erhart and K. Albe, Journal of Applied Physics **102**, 084111 (2007).

[16] P. Ghosez, J.-P. Michenaud and X. Gonze, Physical Review B **58**, 6224 (1998).

[17] E. Bousquet and P.Ghosez, Physical Review B **74**, 180101 (2006).

[18] Y. Li, Q. Liu, T. Yao, Z. Pan, Z. Sun, Y. Jiang, H. Zhang, Z. Pan, W. Yan and S. Wei, Applied Physics Letters **96**, 091905 (2010).

[19] S. B. Zhang and J. E. Northrup, Physical Review Letters **67**, 2339 (1991).

[20] M. W. Finnis, A. Y. Lozovoi and A. Alavi, Annual Review Materials Research **35**, 167 (2005).

[21] N. D. M. Hine, K. Frensch, W. M. C. Foulkes and M. W. Finnis, Physical Review B **79**, 024112 (2009).

[22] A. R. Allnatt and A. B. Lidiard, *Atomic Transport in Solids* (Cambridge University Press, Cambridge, 2003).

[23] K. Johnston, M. R. Castell, A. T. Paxton and M. W. Finnis, Physical Review B **70**, 085415 (2004).

[24] Condensed Phase Thermochemistry Data, NIST Chemistry WebBook, NIST Standard Reference Database Number 69 (2005) (http://webbook.nist.gov).

[25] Y. - J. Zhao, C. Persson, S. Lany and A. Zunger, Applied Physics Letters **85**, 5860 (2004).

[26] D. Aberg, P. Erhart, A. J. Williamson and V. Lordi, Physical Review B **77**, 165206 (2008).

[27] G. Makov and M. C. Payne, Physical Review B **51**, 4014 (1995).

[28] E. Cockayne, Journal of the European Ceramic Society **23**, 2375 (2003).

[29] C. G. van de Walle and J. Neugebauer, Journal of Applied Physics **95**, 3851 (2004).

[30] P. A. Schultz, Physical Review Letters **96**, 246401 (2006).

[31] S. H. Wemple, Physical Review B **2**, 2679 (1970).

[32] G. Kresse and J. Furthmüller, Computational Materials Science **6**, 15 (1996).

[33] D. M. Ceperley and B. J. Alder, Physical Review Letters **45**, 566 (1980).

[34] J. P. Perdew and A. Zunger, Physical Review B **23**, 5048 (1981).

[35] P. E. Blöchl, Physical Review B **50**, 17953 (1994).

[36] G. Kresse and D. Joubert, Physical Review B **59**, 1758 (1999).

[37] J. Evers**,** G. Oehlinger**,** B. Sendlinger**,** A. Weiss, M. Schmidt and P. Schramel**,** Journal of Alloy Compounds **182**, 175 (1992).

[38] C. Kittel, *Introduction to Solid State Physics* (John Wiley and Sons Ltd., New York, 2004).

[39] R. R. Pawar and V. T. Deshpande, Acta Crystallography **24A**, 316 (1968).

[40] A. van der Walle and G. Ceder, Physical Review B **59**, 14992 (1999).

[41] R. J. Zollweg, Physical Review **100**, 671 (1955).

[42] D. Lide, *CRC Handbook of Chemistry and Physics* (CRC Press, Boca Raton, 1998).

[43] S. C. Abrahams and J. L. Bernstein, Journal of Chemical Physics **55**, 3206 (1971).

[44] H. Arend and L. Kihlborg, Journal of the American Ceramic Society **52**, 63 (1969).

[45] M. K. Karapet'yants and M. L. Karapel'yants, *Thermodynamic Constants of Inorganic and Organic Compounds* (Ann Arbor-Humphrey Science Publishers, Michigan, 1970).

[46] S. Na-Phattalung, M. F. Smith, K. Kim, M.-H. Du, S.-H. Wei, S. B. Zhang and S. Limpijumnong, Physical Review B **73**, 125205 (2006).

[47] J. A. Dawson, J. H. Harding, H. Chen and D. C. Sinclair, Journal of Applied Physics **111**, 094108, (2012).

[48] A. Feteira, G. M. Keith, M. J. Rampling, C. A. Kirk, I. M. Reaney, K. Sarma, N. Mc. Alford and D. C. Sinclair, Crystal Engineering **5**, 439 (2002).

[49] H. Moriwake, International Journal of Quantum Chemistry **99**, 824 (2004).

[50] F. D. Morrison, D. C. Sinclair and A. R. West, Journal of Applied Physics **86,** 6355 (1999).

[51] T. D. Dunbar, W. L. Warren, B. A. Tuttle, C. A. Randall and Y. Tsur, Journal of Physical Chemistry B **108**, 908 (2004).

[52] N. -H. Chan and D. M. Smyth, Journal of the American Ceramic Society **67**, 285 (1984).

[53] A. Yamada and Y. -M. Chiang, Journal of the American Ceramic Society **78**, 909 (1995).

[54] T. Oyama, N. Wada and Y. Sakabe, Key Engineering Materials **388**, 269 (2009).

[55] S. Lee, C. Randall and Z. -K. Liu, Journal of the American Ceramic Society **90**, 2589 (2007).

[56] S. Lee, C. Randall and Z. -K. Liu, Journal of the American Ceramic Society **91**, 1748 (2008).

8

Conclusions and Future Work

In this work a number of different computational modelling techniques have been applied to study the defect chemistry of $BaTiO_3$ and other related perovskite materials. Through the application of these varied methods, many interesting undiscovered aspects of these materials have been found as well as many experimentally proven, but not fully understood phenomena.

In our first results chapter we looked at the rare-earth and transition metal doping of the cubic and hexagonal polymorphs of $BaTiO_3$. Using lattice statics simulations and a newly developed potential set for $BaTiO_3$ in combination with previously developed potentials for the rare-earth oxides; we have calculated the solution energies for a range of dopant ions. Excellent agreement with experiment is observed especially when compared to the results of previous models. It was discovered that La doping of the both the cubic and hexagonal polymorphs occurs at the Ba-site with charge compensation via Ti vacancies. Charge compensation via electron compensation was found to be very unfavourable for all dopants tested. This suggests that conduction in donor-doped $BaTiO_3$ comes from O vacancies and this is also supported by recent calculations [1]. Calculations on *h*-$BaTiO_3$ show a preference for face-sharing O vacancies over corner-sharing O vacancies and that Ba-site doping is disfavoured when compared to *c*-$BaTiO_3$. It was also found that transition metal doping on the Ti-site was significantly favoured in *h*-$BaTiO_3$, especially for tri- and tetra-valent ions. This supports a large body of experimental work which shows that the hexagonal phase can be stabilised by such doping.

It would be worthwhile to investigate a lot of these areas using QM methods, especially the energetic consequences of electron compensation and the stabilisation of

the hexagonal phase with transition metal dopants. Analysis using methods such as DFT could provide important additional information on the local structures and the energetics of these processes. Classical calculations on solid solutions of transition metal doped *h*-$BaTiO_3$ would provide important information on systems where the dopant concentrations are in the same range as concentrations in experiment. Although a vast amount of research is available in the literature on the doping of $BaTiO_3$, additional EXAFS and local structure experiments could give stronger links between theory and experiment. This is especially true for comparing potential binding energy configurations in the simulations with reality. It is hoped that our results will provide a deeper understanding of this important topic and inspire future experimental or modelling work into this topic. Our new potential will also allow further research into many different technologically important materials.

In chapter 5 we again used new potentials and lattice statics methods to investigate the energetics and local structure of a range of A-site doped $BaTiO_3$ solid solutions. The validity of two different potential sets was tested by calculating the energy of mixing curves for solid solutions of $Ba_{1-x}Sr_xTiO_3$, $Ba_{1-x}Ca_xTiO_3$ and $Ca_{1-x}Ba_xTiO_3$. Both of the tested potential sets provided adequate qualitative agreement with experiment. However, our potential set produces better agreement for the $BaTiO_3$-$CaTiO_3$ system. Unsurprisingly, the energies of mixing for $BaTiO_3$-$CaTiO_3$ are much large than those for $BaTiO_3$-$SrTiO_3$ because of the large difference in A-site ionic radii in the $BaTiO_3$-$CaTiO_3$ system. We also studied the local structure of the $Ba_{1-x}Ca_xTiO_3$ solid solution to understand its unusual T_c behaviour. Our calculations show that significant Ca-O bond distortion is present in these solid solutions and that in some cases the bonds are stretched far beyond the usual Ca-O bond lengths in $CaTiO_3$ and indeed even some Ba-O bond lengths in the system. Ca displacement calculations also suggest a direct link between off-centring and the unusual T_c behaviour of the material. Our results strongly support some of the experimental theories for this behaviour as well as suggesting new ones.

Further calculations using MD would be useful in analysing the local structures of these solid solutions at temperature and over time and in observing how they change

when additional Ca is added to the system. DFT calculations would also again be very useful in analysing the local structure in detail, although the size of the supercells and the number of calculations required would make this computationally very expensive. Experimentally, further EXAFS analysis could be used to confirm or reject our results on the local structure of Ca-O bonds in this system. The T_c behaviour of the $Ba_{1-x}Ca_xTiO_3$ system has been of interest to the electroceramics community for many years. Our results in combination with experimental findings and hypotheses provide strong evidence linking the local structure of Ca ions in the system to this behaviour. The analysis and techniques presented here can also be applied to other similar problems.

Oxygen diffusion in bulk $BaTiO_3$ and $SrTiO_3$ is the focus of chapter 6. We used MD simulations in combination with MSD analysis to calculate O diffusion coefficients and activation energies for a range of V_O concentrations and potential charge compensation mechanisms. For $BaTiO_3$, three mechanisms were considered, reduction of Ti^{4+} to Ti^{3+} compensation, V_{Ba} compensation and V_{Ti} compensation. In agreement with experiment, both the activation energies and the diffusion coefficients suggested that the reduction of Ti^{4+} ions is the correct charge compensation mechanism. In light of this and experimental results, only the Ti^{3+} mechanism was considered for $SrTiO_3$. The activation energies calculated for both materials are in good agreement with experiment, especially for $BaTiO_3$. Generally the diffusion coefficients calculated are about an order of magnitude too high compared to experiment for the lower temperatures (900 - 1050 K). However, the agreement is far greater at higher temperatures (1200 - 1500 K).

Reducing the V_O concentration for the Ti^{3+} charge compensation mechanism has been shown to increase the activation energy and lower the diffusion in the cell. Further simulations at reduced V_O concentrations would show whether this pattern continues and hopefully further improve experimental agreement. Nudged elastic band (NEB) calculations using MD or DFT simulations would allow the investigation of individual O migration pathways in these materials. They would also allow for a different method of calculating the activation energy. Calculations of O diffusion in the orthorhombic structure of $CaTiO_3$ would also be interesting and would allow for comparison between

this series of perovskites. The effect of the orthorhombic structure on the diffusion would also be of interest. While there are many experimental studies measuring diffusion in these materials using a variety of techniques, there is also considerable inconsistency in these values. A future comprehensive study of tracer diffusion in these materials would, therefore, be very useful. We have shown that our potential is adequate in reproducing the diffusion behaviour of $BaTiO_3$ and $SrTiO_3$. It is hoped that the potentials and methods used here can and will be applied to a range of other materials to inspire further theoretical studies of diffusion.

In chapter 7 we used DFT calculations in combination with the Zhang-Northrup formalism to study the formation of mono- and di-vacancies in *h*-$BaTiO_3$. Using the Zhang-Northrup formalism we calculated the formation energies for each vacancy type over a range of charges and chemical environments. The necessary corrections for the supercell approach and band-gap error were also applied. The defect concentrations at equilibrium were also calculated. It was confirmed that all the vacancies exist in the nominal charge state and that V_{O1} has the lowest formation energy. Under reducing conditions (i.e. low oxygen partial pressure) the formation energy of V_{O1} is found to be negative for all values of the Fermi level. This agrees with experimental results that stoichiometric *h*-$BaTiO_3$ cannot be formed under such conditions. The results also suggest that defect pairs will readily form in the system.

As discussed in chapter 6, a comprehensive DFT study of vacancies in the cubic phase is available in the literature. However, in this study the chemical potential of oxygen is calculated directly from DFT calculations and not by using ideal gas relations as is the case in our work. A new study on *c*-$BaTiO_3$ using this method for calculating the oxygen chemical potential would allow for a more accurate comparison of these two phases. Similarly, DFT studies of similar materials like $SrTiO_3$ and $CaTiO_3$ would be useful in identifying the differences in vacancy formation in this series of materials. Such studies would also be able to test the quality of our own and others potential sets by comparison with the results from lattice statics calculations.

In this thesis, we have used a variety of modelling techniques to study a plethora of different defects in a range of perovskite materials. We have shown the power and

relative ease with which these different techniques can produce a wealth of crucial information. Above all, the importance of modelling and experimental collaboration is apparent in solving problems that would otherwise be difficult or impossible to solve separately.

References

[1] C. L. Freeman, J. A. Dawson, H. Chen, L. -B. Ben, J. H. Harding, A. R. West and D. C. Sinclair, Advanced Functional Materials (submitted) (2012).